Schweizerische Eidgenossenschaft
Confédération suisse
Confederazione Svizzera
Confederaziun svizra

Départmenet fédéral de l'environnement, des transports,
de l'énergie et de la communication DETEC
Office fédéral de l'énergie OFEN

Final report November 2012

SolAir-2 (1)

Innovative solar collectors for efficient and cost-effective solar thermal power generation – 2

SolAir-Pilot (2)

AIRLIGHT ENERGY

University of Applied Sciences and Arts
of Southern Switzerland
SUPSI

ETH
Eidgenössische Technische Hochschule Zürich
Swiss Federal Institute of Technology Zurich

THIS PAGE INTENTIONALLY LEFT BLANK

Mandant:

Office fédéral de l'énergie OFEN
Programme de recherche Solaire industriel à haute température
CH-3003 Berne
www.bfe.admin.ch

Cofinancement:
--

Mandataire:

Airlight Energy Holding SA
Via Croce, 1
CH-6710 Biasca
www.airlightenergy.com

SUPSI – DTI – ICIMSI
Via Cantonale, Galleria 2
CH-6928 Manno
www.supsi.ch ; www.icimsi.ch

ETHZ – Institute of Energy Technology
ML J 42.1, Sonneggstr. 3
CH-8092 Zurich
www.ethz.ch , www.iet.ethz.ch

Auteurs:

Maurizio C. Barbato, SUPSI – DTI – ICIMSI, maurizio.barbato@supsi.ch
Antonio Gaetano, SUPSI – DTI – ICIMSI, antonio.gaetano@supsi.ch
Davide Montorfano, SUPSI – DTI – ICIMSI, davide.montorfano@supsi.ch
Simone A. Zavattoni, SUPSI – DTI – ICIMSI, simone.zavattoni@supsi.ch
Gian Maria Di Stefano, SUPSI – DTI – ICIMSI, gianmaria.distefano@supsi.ch
Stefano Airaghi, SUPSI – DTI – ICIMSI, stefano.airaghi@supsi.ch
Paolo Matarrese, SUPSI – DTI – ICIMSI, paolo.matarrese@supsi.ch

Philipp Good, ETHZ–IET, pgood@ethz.ch
Aldo Steinfeld, ETHZ–IET, aldo.steinfeld@ethz.ch
Giw Zanganeh, ETHZ–IET, giwz@ethz.ch

Gianluca Ambrosetti, Airlight Energy Manufacturing SA, gianluca.ambrosetti@airlightenergy.com
Fabio Malnati, Airlight Energy Manufacturing SA, fabio.malnati@airlightenergy.com
Andrea Pedretti, Airlight Energy Manufacturing SA, andrea.pedretti@airlightenergy.com
Simone Pusterla, Airlight Energy Manufacturing SA, simone.pusterla@airlightenergy.com

Responsable de domaine de l'OFEN: Stefan Oberholzer
Chef de programme de l'OFEN: Pierre Renaud
Numéro du contrat et du projet de l'OFEN: (1) SI/500091-01 / SI/500091
(2) SI/500508-01 / SI/500508

THIS PAGE INTENTIONALLY LEFT BLANK

Table des matières

Chapter *Page*

THIS PAGE INTENTIONALLY LEFT BLANK

Abstract

The present final report shows results of the research and development activity performed for the SolAir-2 and SolAir-Pilot project during year 2012. The partners working activities are focused on:

- Receiver development:
  - cavity receiver modeling and simulations;
  - multi-shields insulation modeling, simulation and testing.

- Energy storage system:
  - experimental void fraction measurement;
  - proposal of the test campaign for the new storage prototype.

Chapter 1 illustrates the new design of the receiver. The effect of geometrical variations on its performance is evaluated by means of simplified models.

Chapter 2 reports the CFD simulations results performed to assess the behavior and the performance of the new cavity receiver. Various models are simulated evaluating the effect of changing some important geometrical characteristics such as internal absorber tube diameter and cavity dimensions.

Chapter 3 proposes a theoretical model for the cavity performances. The effects of the main geometrical parameters are investigated to improve the receiver design in terms of efficiency and costs.

Chapter 4 reports the analysis performed on the radiation shields thermal insulation of the receiver prototype, identified as BRCPHC-7. The simulations considered a radiation shields insulation geometry composed by metallic shields separated by air and calcium silicate spacers. The main objectives of this study are to define how shield quantity, shape and distance influence overall performance. Effects of spacers to heat transfer, and effects of different shapes of them, are also investigated.

Chapter 5 reports the results of the test campaign which aims at measuring the performance of a multi-shields thermal insulation prototype.

Chapter 6 reports about the CFD simulations performed to assess the behavior of the receiver thermal insulation. Various thermal insulation designs are analyzed and, based upon the simulations results, different improvements are also proposed.

Chapter 7 provides the mathematical model description, based on the electrical analogy, exploited to evaluate the receiver performance in terms of available power and receiver efficiency. The geometry is also optimized to guarantee a uniform distribution of the mass flow rate for each cavity.

Chapter 8 reports about the new version of the proposal of the test campaign aimed at evaluating the performance of the new receiver prototype. Moreover, the experimental test performed to measure the void fraction of a vibrated bed, simulating the aging of the storage system, is reported and detailed.

THIS PAGE INTENTIONALLY LEFT BLANK

Chapter 1

Air-receiver preliminary analysis

Contents

List of Figures

1.1. Introduction

This chapter provides an overview on the activities, related to the receiver performance analysis. The receiver design has been modified from the last version shown in [1]. A simplified sketch of the new design is given in Figure 1.

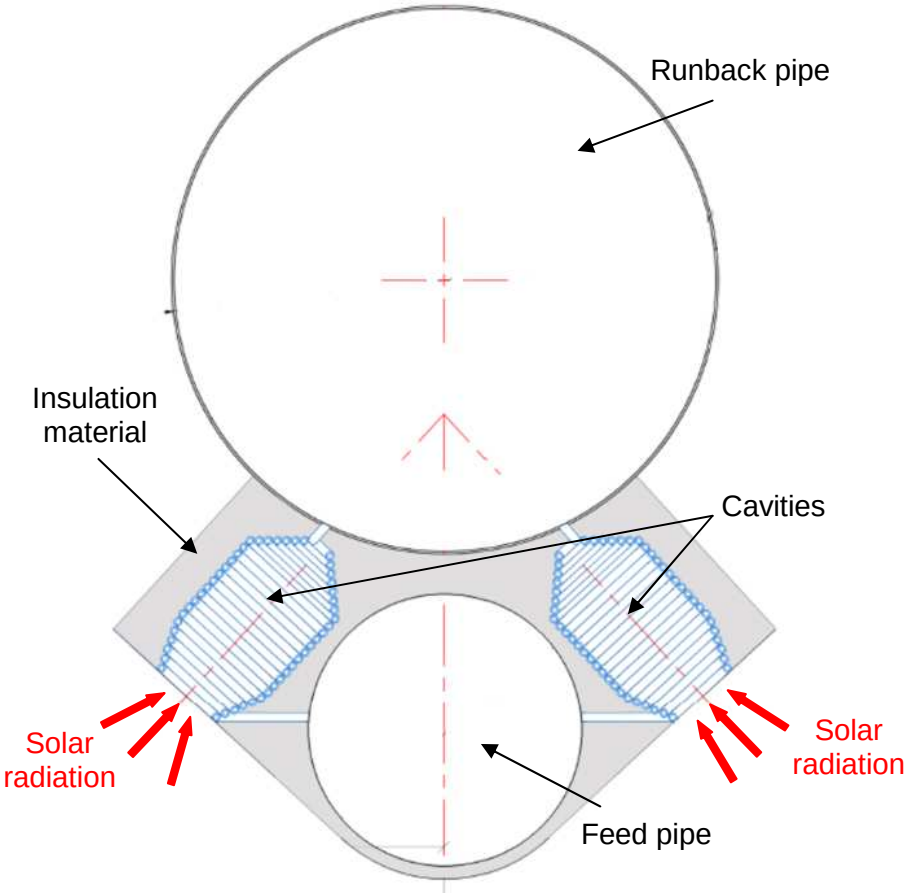

FIGURE 1: SIMPLIFIED SKETCH OF THE RECEIVER.

The receiver includes an air inflow pipe called “feed pipe”, a series of cavities formed by a coil of steel pipe, and a hot air pipe called the “runback pipe”. Each cavity inlet is connected to the feed pipe whereas cavity outlets are connected to the runback pipe. Air flows from the feed pipe to the cavities. Each cavity is irradiated by the solar radiation focused by the main mirror and by a secondary optics (not shown in Figure 1). As flowing into the coiled tube, air heats up to high temperature and is collected by the runback pipe. There are more than 4’000 cavities along the two sides of the receiver and each one is designed to heat air up at the desired temperature (650℃). All the parts of the receiver are insulated. The runback pipe is insulated by thermal shields (not shown in Figure 1) while for the other parts a solid insulation material will be considered. The receiver performances were evaluated looking at total mass flow rate, system pressure drop and temperature of the fluid at the outlet section of the runback pipe.

1.2. Receiver modelling: electrical analogy

Due to the size and the complexity of the system, the receiver performances are analysed by means of a non-dimensional model based on the electrical analogy. The feed and the runback pipes and all the cavities tubes are considered as part of an electrical circuit. The mass flow rates are the currents of the circuit, the pressure drops are the potential difference and an equivalent resistance relates pressure drop and mass flow rates.

$$\Delta P = \Delta V; \quad I = \dot{m}_{flow} \quad \Delta V = R \cdot I \;\rightarrow\; \Delta P = R_{flow}\dot{m}_{flow}$$

A schematic of the electrical analogy is shown by Figure 2 where different equivalent resistances are:

- R_c = cavity resistance;
- R_f = resistance given by the feed pipe between two adjacent cavities;
- R_b = resistance given by the runback pipe between two adjacent cavities.

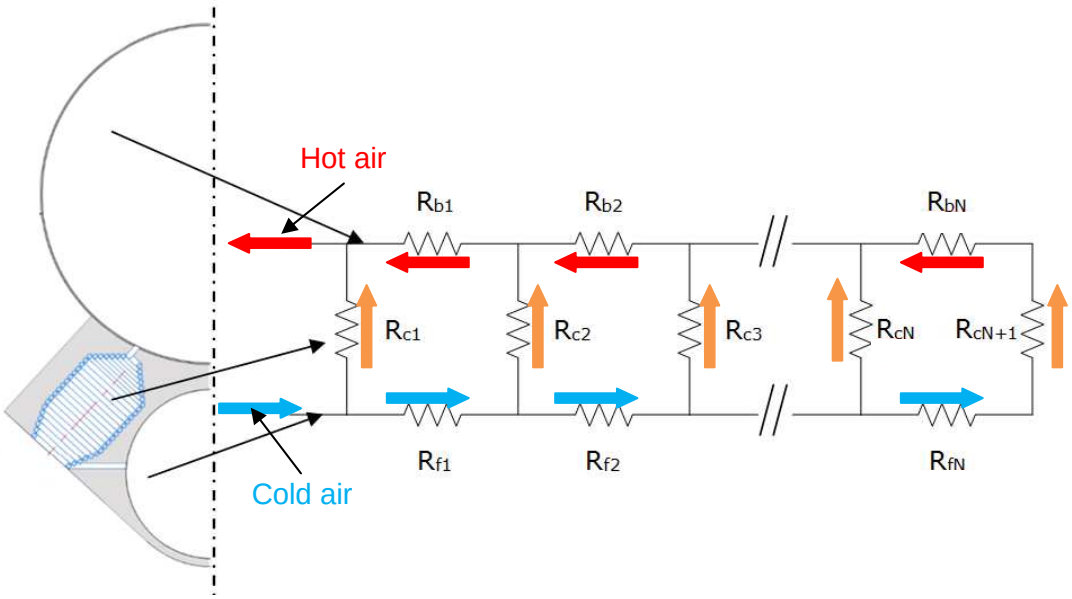

FIGURE 2: RECEIVER ELECTRICAL ANALOGY.

For a flow in a straight tube the pressure drop can be computed, as a first approximation, by the following relations [2]:

$$\Delta P = f\frac{L}{D}\rho\frac{v^2}{2} = f\frac{L}{D}\frac{\rho}{2}\left(\frac{m_{flow}}{\rho\pi\frac{D^2}{4}}\right)^2 = \left[f\frac{L}{D}\frac{\rho}{2}\frac{m_{flow}}{\left(\rho\pi\frac{D^2}{4}\right)^2}\right]m_{flow} = R_{flow}m_{flow}\ [Pa]$$

$$R_{flow} = \left[f\frac{L}{D}\frac{\rho}{2}\frac{m_{flow}}{\left(\rho\pi\frac{D^2}{4}\right)^2}\right]\left[\frac{Pa}{kg/s}\right]$$

Wherein *f* is the friction coefficient, *L* and *D* the tube length and diameter respectively and ρ is the fluid density. Notice that the flow resistance is a function of the mass flow rates, so the circuit cannot be solved directly but considering an iterative method. The number of cavities, for a receiver of length L_{rec} can be computed as

$$N_{cavity} = number\ of\ cavities = 2\frac{L_{rec}}{d_{opt}} = 4200$$

Where d_{opt} is the optical cavity step (i.e., the distance between the axes of two adjacent cavities). The factor 2 is due to the fact that there are two rows of cavities besides the air feed pipe. To solve the circuit for evaluating the system pressure drop and the distribution of the mass flow rates inside the cavities, mean properties of the fluid have been considered.

1.3. Results

The main results given by the electrical analogy model are the receiver pressure drop, which is important to evaluate the pumping power, and the cavity mass flow rates distribution along the receiver length. A uniform mass flow rate for the cavities is a very important condition since it means that, provided a uniform cavity irradiation, each cavity can heat air up at the desired temperature. If the mass flow rate for a cavity is larger than the optimal one, the exit fluid temperature for that cavity will be lower than the desired one. On the contrary if the mass flow rate is lower than the optimal one, the cavity is not able to dissipate all the power coming from the solar radiation and its walls temperature could overcome the limit of the tube material.

1.3.1. Effect of the runback pipe and feed pipe diameters variation

The diameters of the runback pipe and of the feed pipe have a strong effect on the receiver pressure drop and on the distribution of the mass flow rates inside the cavities. Three possible diameters have been considered for the feed pipe (D_f = 200 mm, 225 mm, 250 mm) and the runback pipe (D_{rb} = 350 mm, 400 mm, 450 mm).

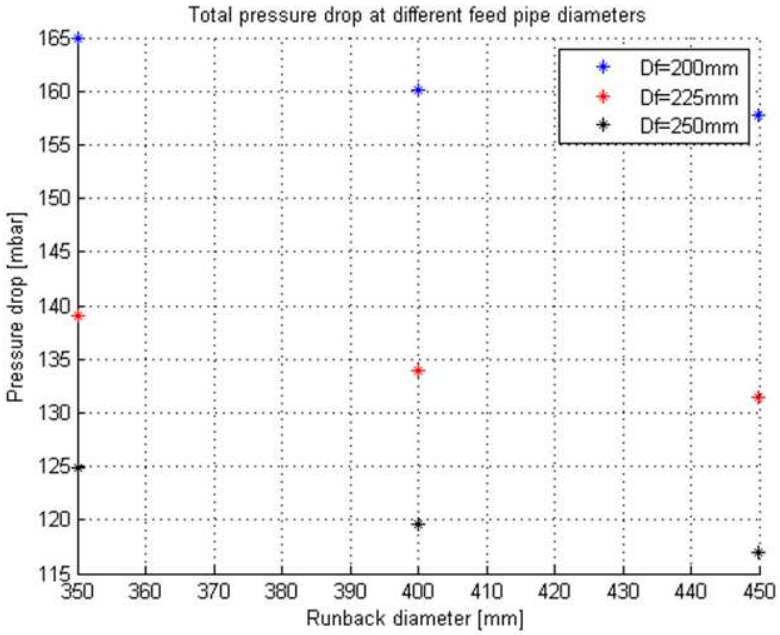

FIGURE 3: PRESSURE DROP FOR DIFFERENT FEED AND RUNBACK PIPES DIAMETERS.

Figure 3 presents the pressure drop for the receiver plotted against the runback pipe diameter. Results are parameterized with feed pipe diameter. These results show the expected pressure drop behaviour: the larger the feed and runback pipes diameters the lower the receiver pressure drop. For the analysis of the mass flow rates distribution, the effect of the feed pipe and of the run back pipe has been considered separately in the following. Figure 4 shows the mass flow rate per cavity along the receiver length. The results are for a feed pipe diameter of 250 mm and are parameterized with three different runback pipe diameters.

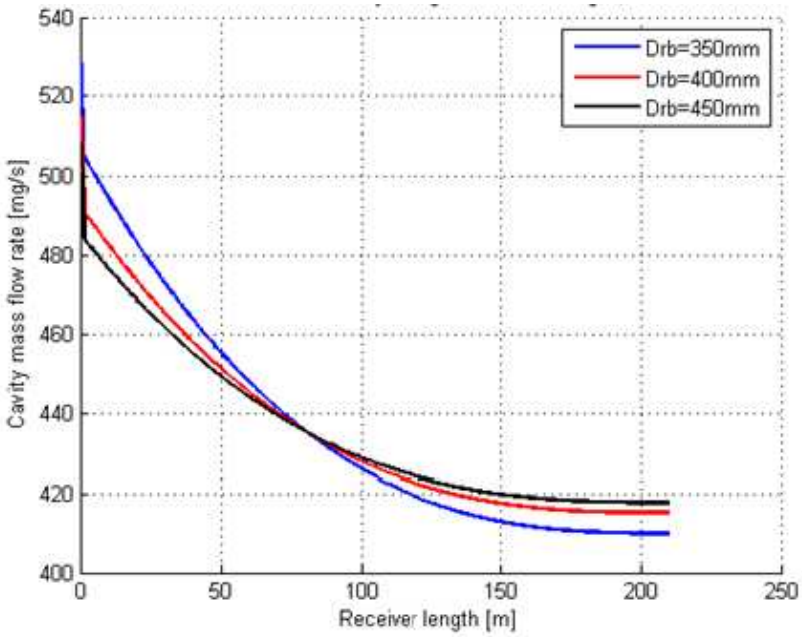

FIGURE 4: CAVITY MASS FLOW RATES FOR CONSTANT DF = 250 mm.

Figure 4 highlights that the mass flow rates distribution becomes more uniform when the runback pipe is larger, however there is a moderate variation between the three diameters considered. The “weird behaviour” on the initial part of the curves (inlet of the receiver) is due to the fact that there is no head pipe in the electrical circuit (see Figure 2) and the flow inlet also corresponds to the position of the first cavity. In that point there is a sudden variation of the mass flow rate. However this imperfection will be eliminated in the future development of the model.

The effect of the feed pipe diameter can be seen in Figure 5 which reports the cavity mass flow rate along the receiver for a constant runback diameter of 450 mm. The curves are parameterized as function of the feed pipe diameter. Figure 5 shows that the difference among the cavities mass flow rates is smaller when the feed and runback pipe diameters are large enough to reduce the pressure losses. This results show that increasing the diameter of both runback and feed tubes, their behaviour tends to be that of pressure tanks, granting in this way almost uniform feeding and exhaust conditions for the cavities along the receiver.

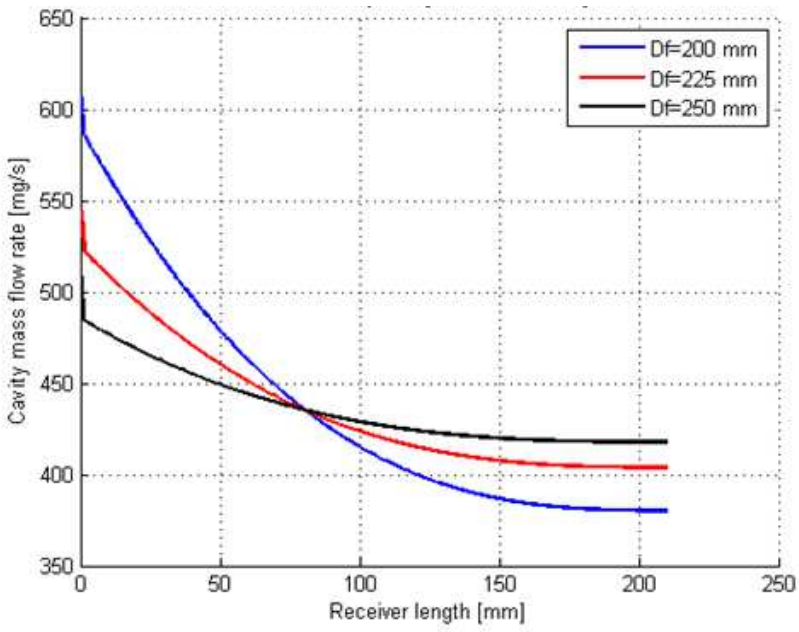

FIGURE 5: EFFECT OF THE FEED PIPE DIAMETER ON THE CAVITY MASS FLOW RATE.

1.3.2. Effects of diameter variation along the runback pipe

To reduce thermal losses and the volume of insulation material for the runback pipe, a possible variation of its diameter along the receiver length was considered. The runback pipe was assumed to be divided in a certain number of segments (D_{rb}-steps = 2, 5, 10) of equal length while three diameters have been considered for the outlet section. The diameter of the different pipe segments was computed assuming an equal pressure drop for all of them. This approach was a first assumption to model the pressure drop along the runback pipe with a more sophisticated design. Considering the three diameters for the outlet section and the number of divisions, the pressure drop of the system has been computed as well as the mass flow rate through each cavity. Figure 6 shows the receiver pressure drop when varying the runback pipe diameter. The results are parameterized by the number of sections diameter changes along the pipe.

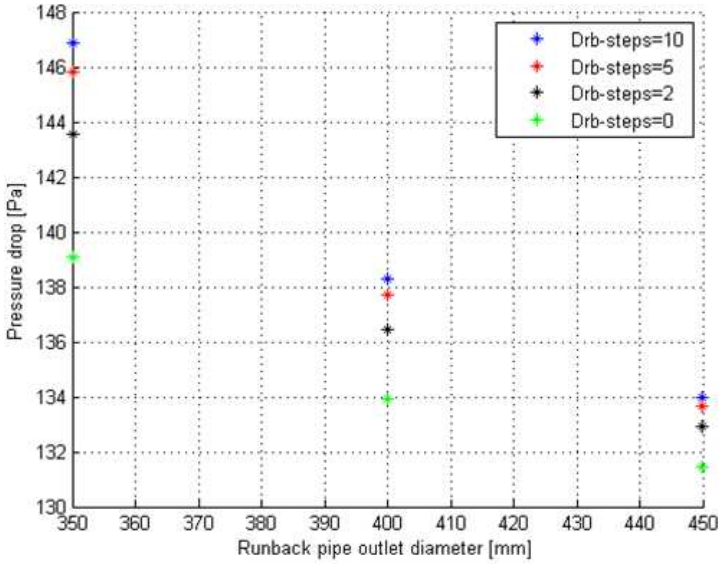

FIGURE 6: RECEIVER PRESSURE DROP FOR A RUNBACK PIPE WITH VARIABLE DIAMETER.

The results show that sectioning the runback pipe diameter increases the receiver pressure drop. It must be noted that the pressure drop can further rise because of the additional losses due to the diameter variation that were not accounted by now. The analysis of the mass flow rates distribution has been performed considering a runback pipe outlet diameter of 450 mm and it is reported in Figure 7.

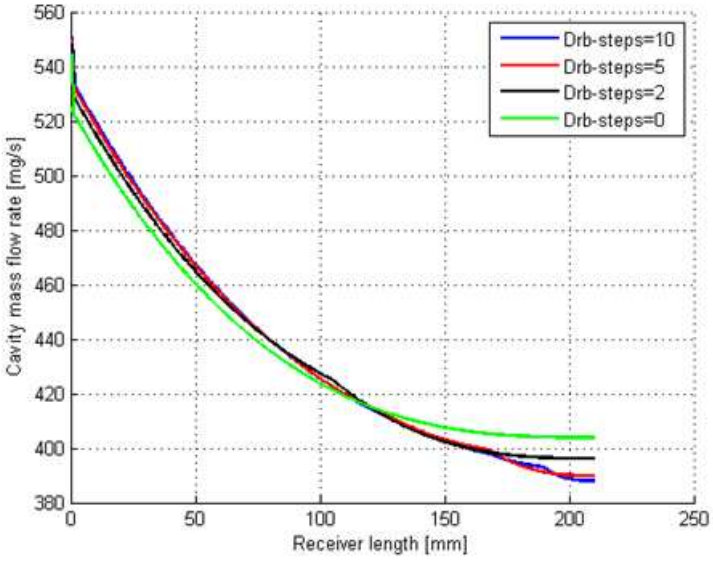

FIGURE 7: CAVITY MASS FLOW RATE IN CASE OF VARIABLE RUNBACK PIPE DIAMETER.

The oscillation of the mass flow rates distribution when the number of divisions increase is due the sudden variation of the runback pipe diameter. The distribution of the cavity mass flow rates gets less uniform as the number of divisions increases. The pressure losses in the runback pipe increase substantially and its performances move away from the condition of constant pressure tank.

1.4. Cavity analysis

In the previous model the air flowing through a cavity was assumed to have an inlet temperature of 120℃ and an outlet temperature of 6 50℃. It has been shown that the mass flow rates distribution is not uniform, therefore, for a constant value of the concentrated solar power entering each cavity, the air outlet temperature cannot be assumed to be the same for each cavity. Given the total input power for each cavity, the achievable outlet temperature of the fluid, depends on the real mass flow rate and on the thermal losses. A simplified cavity model has been implemented to take into account this effect and model the outlets temperature distribution of the air and its effects on the system pressure drop and on the mass flow rates distribution. This model has been used to compare different cavity tube diameters and analyse their thermal losses. The model results will be also validated by means of CFD simulations.

1.4.1. Computational model

The heat transfer process through the cavity was simulated with the aid of a simplified model. A schematic of the cavity is given in Figure 8.

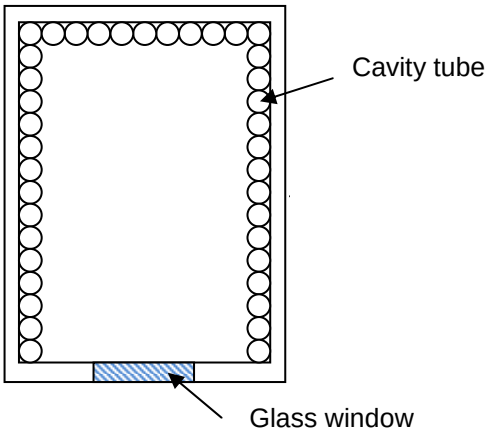

FIGURE 8: CAVITY SCHEMATICS.

The heat transfer model is divided in two sub-models to compute the heat flux to the fluid and the heat losses through the glass window. For the time being cavity walls have been assumed as adiabatic. The first sub-model considers the internal cavity temperature and the input power coming from solar radiation to compute the increase in temperature of the air in the spiral. The pressure drop can also be computed noticing that the heat transfer coefficient and friction coefficient for a spiral pipe differs a lot from those of a straight pipe. Those coefficients have been computed considering the relations given by Manlapaz and Churchill in [3] and [4].

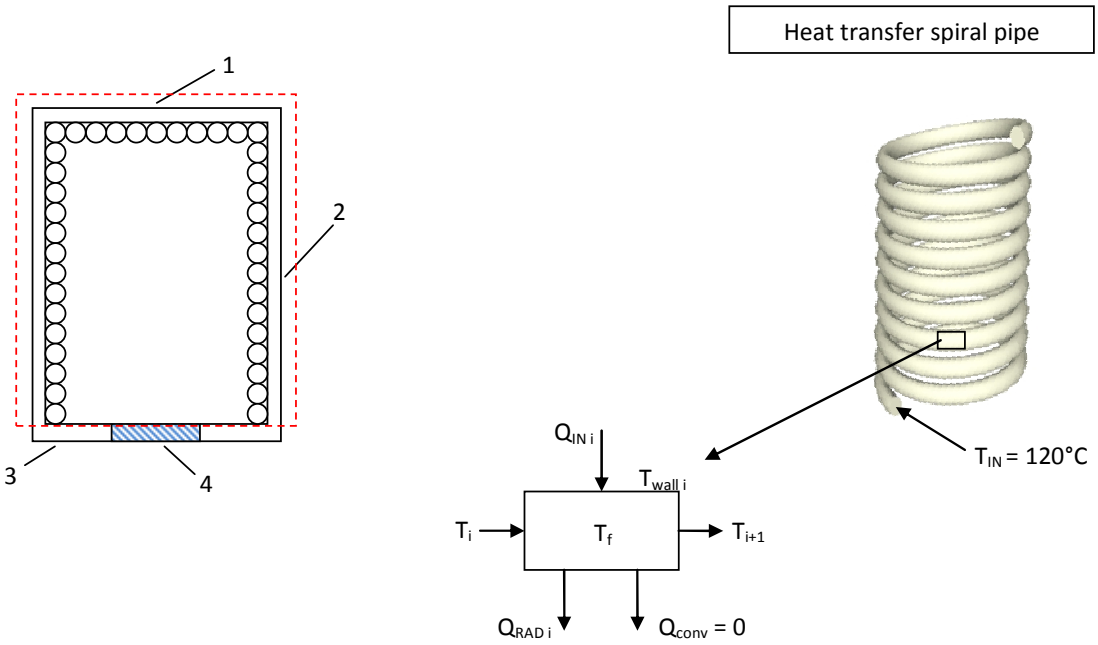

FIGURE 9: HEAT TRANSFER SUB-MODEL FOR THE SPIRAL PIPE.

The second sub-model of the cavity model considers the heat fluxes through the glass window. A schematic of the second part of the model is given in Figure 10.

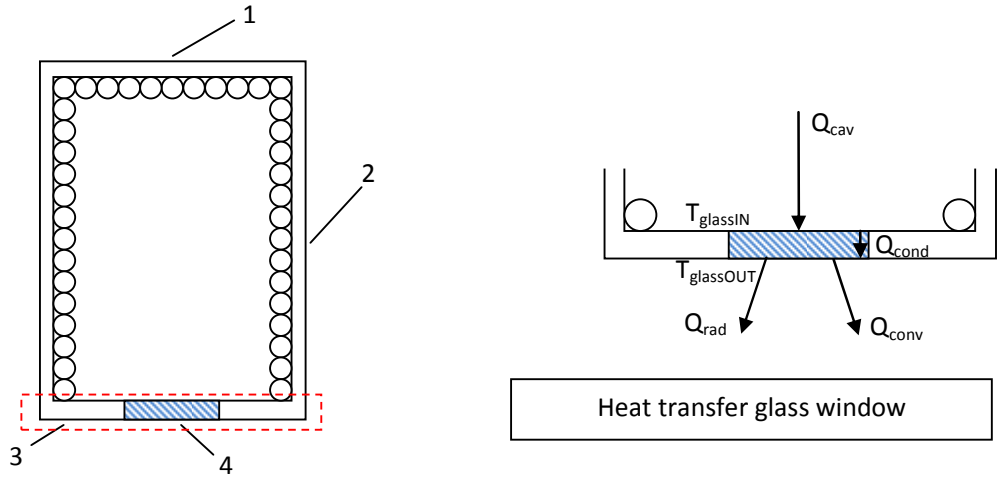

FIGURE 10: HEAT TRANSFER SUB-MODEL FOR THE CAVITY WINDOW.

The combination of the two sub-models allows the computation of the main cavity characteristics: e.g. fluid temperature at outlet of the cavity, glass window temperature, heat losses through the glass (radiative and convective) and pressure drop through the cavity pipe.

1.4.2. Cavity model results

As a preliminary evaluation of the cavities an investigation on the pipe diameter effects is performed. Three different pipe diameters were investigated. The inlet mass flow rate, not being yet defined, was varied from 10^{-4} kg/s to 10^{-3}kg/s. For this analysis the interesting output parameters are outlet fluid temperature, pressure drop across the cavity, heat losses and glass window temperature. Simulations show that the heat transfer process, by maintaining the same geometrical characteristics of the cavity, is minimally affected by an increase in pipe diameter so the air outlet temperature doesn't change (see Figure 11). This is due to the fact that the cavity inner surface area viewing the glass window is not affected by the pipe diameter variation.

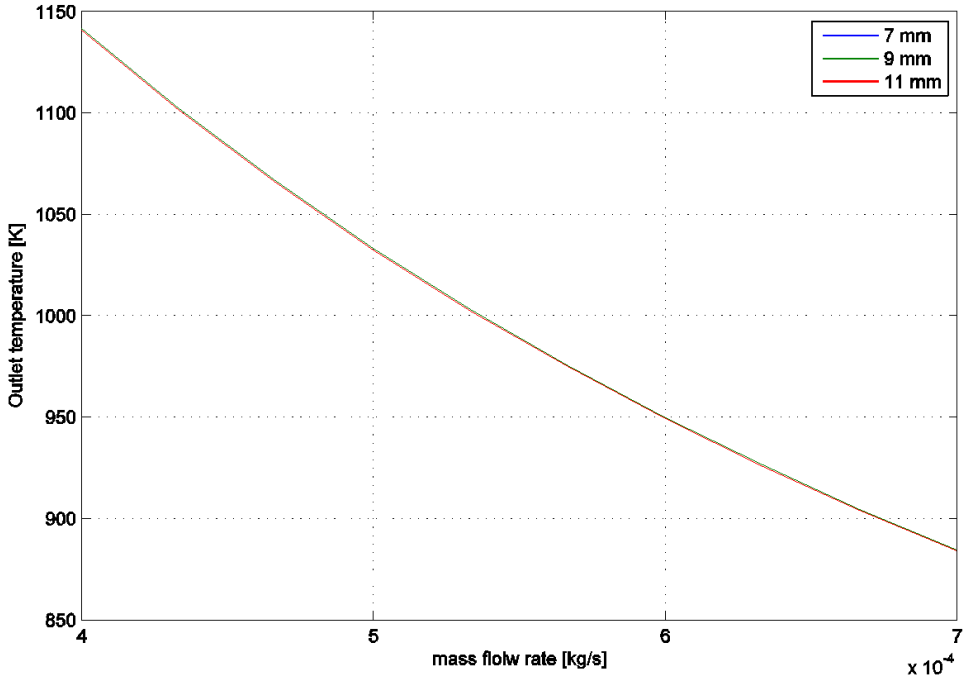

FIGURE 11: OUTLET TEMPERATURE AS A FUNCTION OF THE CAVITY PIPE DIAMETER.

In Figure 11, where the air temperature at the cavity outlet is plotted against the air mass flow rate and parameterized with the pipe diameter, the curves are so close that it is nearly impossible to distinguish them. It means that the heat transfer process is not affected by the cavity pipe diameter. Figure 12 the heat losses as a function of the receiving cavity mass flow rate.

Figure 13 reports air pressure drop through the cavity as a function of the mass flow rate and of the pipe diameter (as a parameter). As expected the larger the pipe diameter the lower the pressure drop.

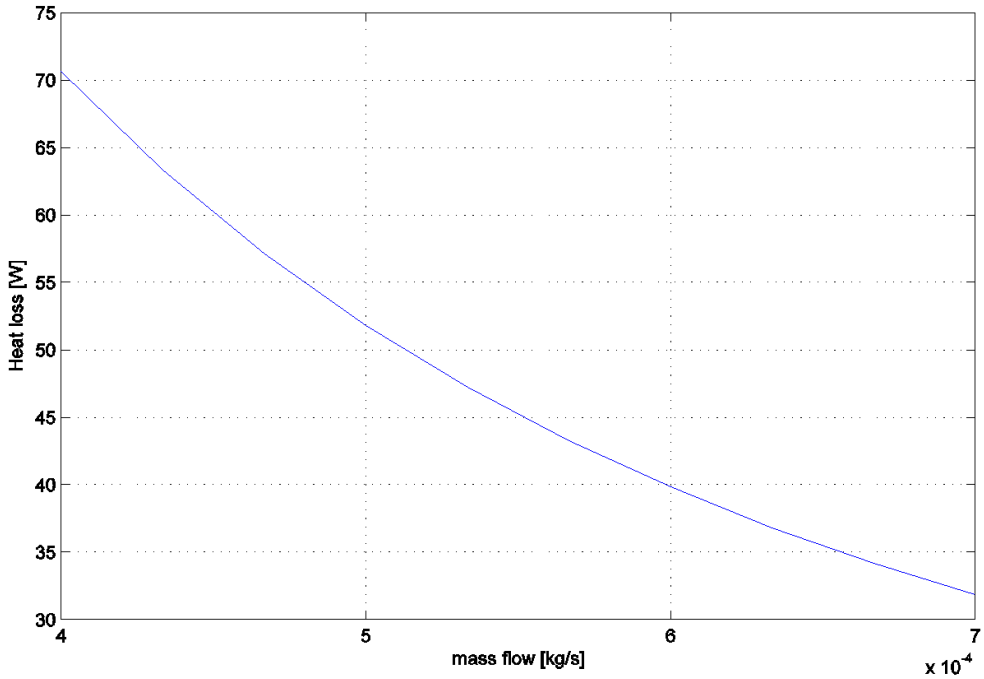

FIGURE 12: HEAT LOSSES AS A FUNCTION OF THE CAVITY MASS FLOW RATE.

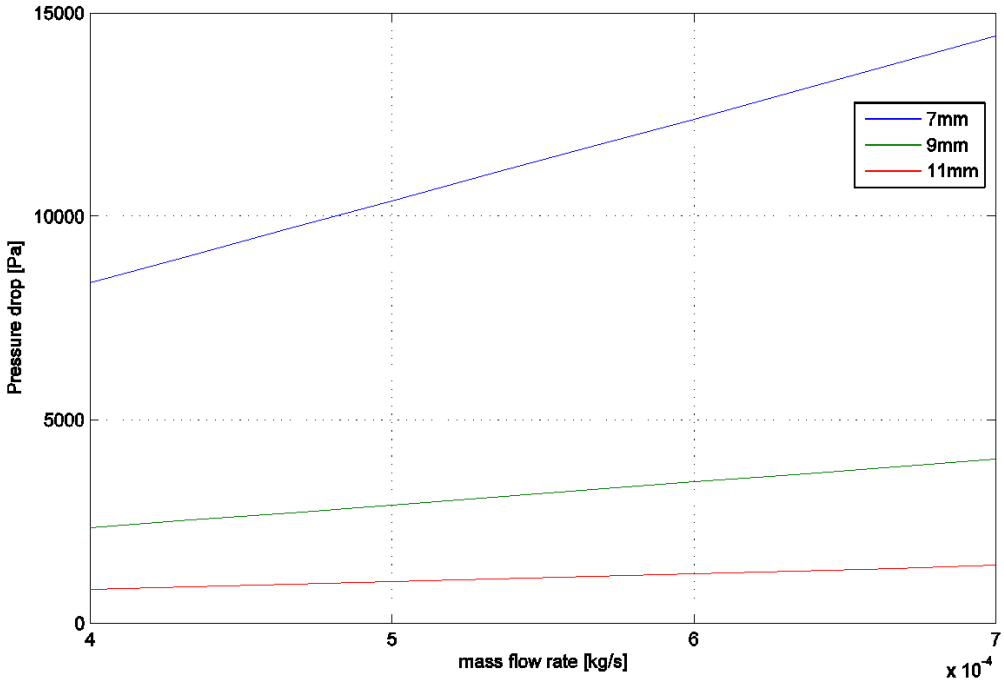

FIGURE 13: CAVITY PRESSURE DROP AT DIFFERENT CAVITY TUBE DIAMETERS.

1.5. Receiver model: whole system with heat transfer

By combining the above described models it is possible to simulate the behaviour of an entire receiver. This is important because due to the pressure drop the different cavities are fed with different values of mass flow rate and, as a consequence, they have different pressure drop and different exhaust air temperature. As an example for a receiver built with identical cavities, those nearer to the feed pipe inlet have larger mass flow rates and lower air outlet temperature with respect to those farther along the receiver. It is therefore mandatory to couple the different models to obtain a prediction of the whole system behaviour and be able to compute air flow temperatures in the runback pipe. Aiming at a receiver outlet temperature of 650℃, the model allows also monitoring the components (pipes and glass windows) peak temperatures so to control critical situations and avoid material failures. A comparison of several scenarios was conducted and, in the following, one of those tests is presented as an example.

The simulation was performed for a wide range of total mass flow rates. Figure 14 gives an overview of the receiver main temperatures as function of the mass flow rate. The red and the blue lines represent the maximum and the minimum outlet temperatures of the cavities for a given total mass flow rate. According to Figure 11, the maximum temperature is reached in the last cavity (the farthest from the feed air inlet that is the one with the lowest mass flow rate) and the minimum temperature is reached in the first cavity (the nearest to the feed air inlet, that is the one with the highest mass flow rate). The black line corresponds to the temperature at the outlet section of the runback pipe. This temperature is computed by modelling the mass flow rates and the outlet temperatures of each cavity of the receiver.

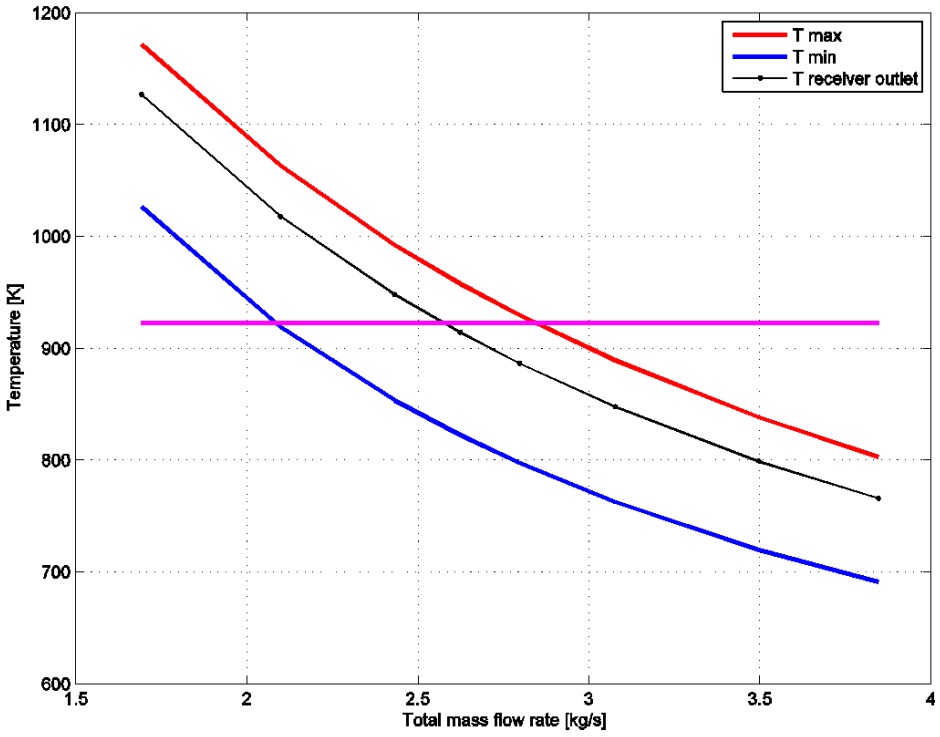

FIGURE 14: RECEIVER TEMPERATURE RANGES.

It is worth to note that, by setting the outlet temperature to the desired value of 650℃ (Figure 14, line magenta) and defining a maximal allowed temperature for the cavity, a range of duty points can be found. For this particular case the maximum total mass flow rate to obtain an outlet temperature of 650℃ (923.15 K) is about 2.6 kg/s. By assuming a maximum allowable cavity outlet temperature of 1'100 K the functioning range is located between 2-2.6 kg/s.
Figure 15 reports the receiver pressure drop as a function of the total mass rate. For the range of duty points identified above, the pressure drop goes from 3'800 to 5'000 Pa. Instead, Figure 16 shows the maximum and minimum cavity mass flow rates for a given total mass flow rate.

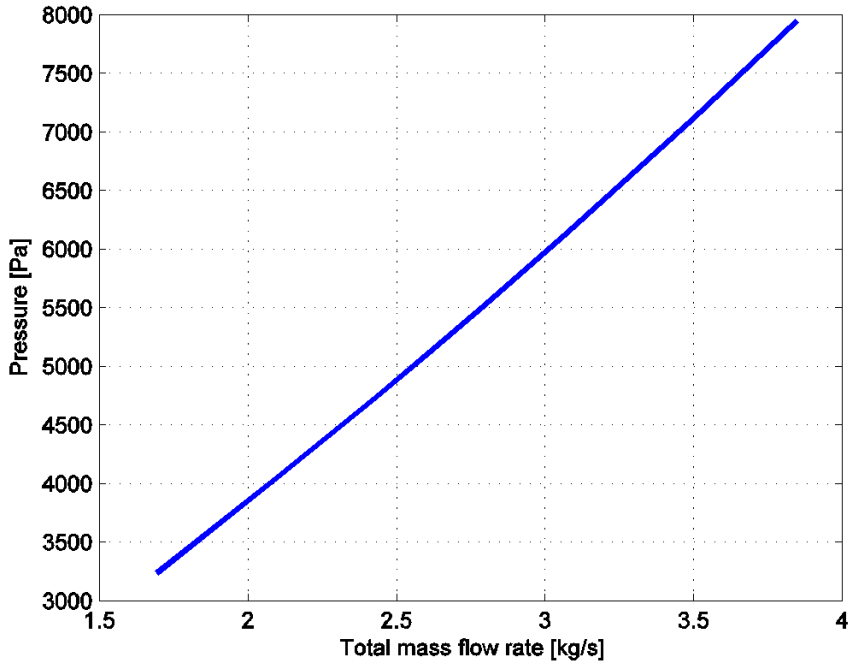

FIGURE 15: PRESSURE DROP AS A FUCNTION OF THE TOTAL MASS FLOW RATE.

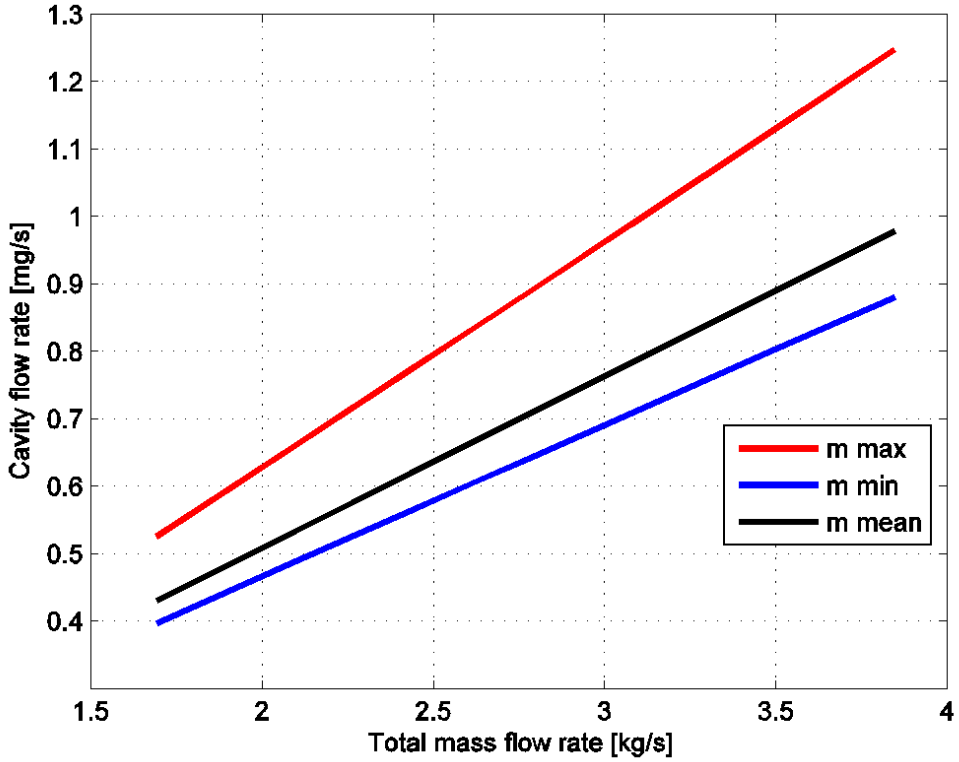

FIGURE 16: MAXIMUM AND MINIMUM CAVITY MASS FLOW RATES.

The larger the total mass flow rates the wider the unbalance of the cavity mass flow rate distribution. New geometrical configurations for the receiver are going to be analysed to overcome this problem.

1.6. Conclusions

A mathematical model based on the electrical analogy was developed to analyse the receiver performances. The effects of the main geometrical parameters (feed and runback pipes diameters, cavity pipe diameters) have been studied to improve the receiver design. Concerning the feed and the runback pipes the main conclusion is that the larger they are the better is for the receiver pressure drop and the cavity mass flow rates distribution. A thermodynamic model for the cavity was used to compute the outlet air temperature for each cavity and the air temperature at the outlet section of the receiver. The temperature distribution along the receiver is very important for the system efficiency and for avoiding the risk that some cavities overcome the material temperature limits. The results presented in this Chapter must be considered as a preliminary approach aimed at highlighting the critical characteristics of the receiver design. Those results need to be validated by more accurate CFD simulations and by experimental tests. An accurate CFD analysis of the cavities behaviour can be found in Chapter 2 of this report.

1.7. References

[1] “SolAir 2 - Innovative solar collectors for efficient and cost-effective solar thermal power generation - 2,” BFE annual report, 2011.

[2] ”Heat transfer a practical approach” Yunus A. Cengel, Second Edition, 2002.

[3] Fully developed laminar flow in a helically coiled tube of finite pitch, Romeo L. Manlapaz and Stuart W. Churchill, Chemical Engineering Communications, 7:1-3, 57-58.

[4] Fully developed laminar convection from a helical coil, Romeo L. Manlapaz and Stuart W. Churchill, Chemical Engineering Communications, 9:1-6, 185-200.

Chapter 2

Cavity model – CFD analysis

Contents

List of Figures

2.1. Introduction

This chapter aims at providing a complete overview on the results achieved, by means of computational fluid dynamic (CFD) simulations performed at SUPSI, related to the new cavity receiver.

After a first introductive section, describing the working principle of this receiver, all the main issues analyzed are reported and extensively described. The latter can be summarized as:

- effect of the skew angle of the incoming solar energy on the receiver performance;
- receiver set-back analysis;
- effect of receiver height and diameter variation on the overall performance;
- assessment of the receiver behaviour without the cover.

2.2. Receiver geometry and working principle

The geometry of the new cavity receiver is reported on l.h.s. of Figure 1; it is basically a hollow steel tube, wrapped in a spiral with a given diameter, forming the cavity wherein solar energy is concentrated. As depicted on r.h.s. of Figure 1, solar energy is collected and focused by the primary optics (mirror) towards the receiver where a secondary high-efficiency concentrator allows to avoid potential dispersion of energy directing it into the cavity through a glass window. This high density solar energy hits the inner surface of the cavity leading to an increment of its internal energy. Thermal energy is then gathered by the heat transfer fluid (air) which is fed into the receiver from the bottom, at low temperature. At the end of the receiver, hot air is then collected into the run-back pipe.

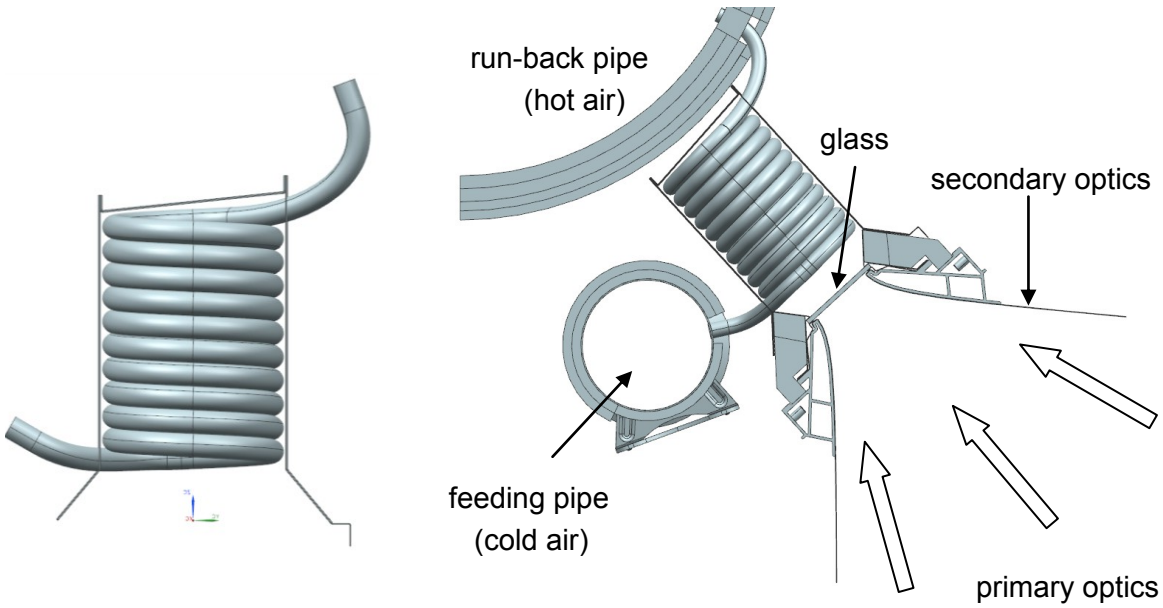

FIGURE 1: CHRYSALIS GEOMETRY (L.H.S.) AND WORKING PRINCIPLE OF THE NEW RECEIVER (R.H.S).

2.3. CFD model and boundary conditions

The behaviour of the receiver, as well as the effect of some geometric parameters on its overall performance, were assessed by means of 3D steady-state CFD simulations. Radiation heat transfer was accounted for by the discrete ordinates (DO) model [1][2].

At the beginning, since the geometry of the external insulation was not yet designed, the external surfaces of the receiver were considered adiabatic; the only exception was made for the glass window wherein power losses, by means of convection and radiation towards the external environment, were accounted for. Figure 2 depicts a schematic representation of the receiver with the boundary conditions used for the computations.

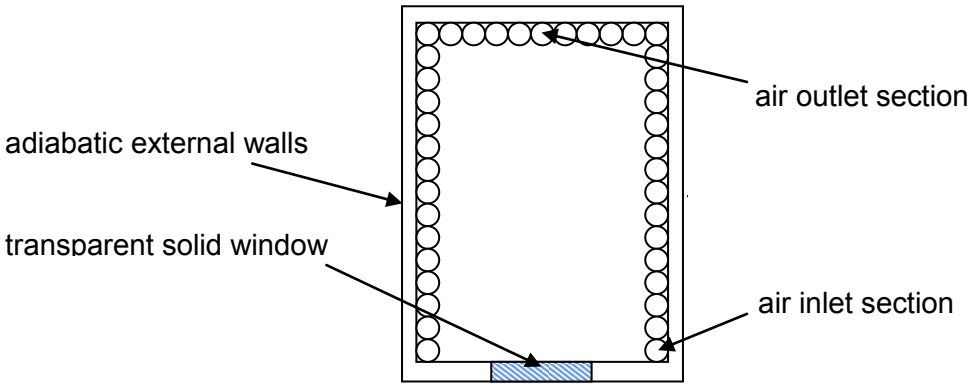

FIGURE 2: RECEIVER SCHEMATIC AND BOUNDARY CONDITIONS APPLIED.

The amount of energy entering the cavity was provided, in terms of flux [W/cm^2] by Airlight which performed a ray-tracing simulation of the whole receiver structure: ETFE layer, primary and secondary optics and the glass window. Once known the input power and the inlet temperature of the air, the mass flow rate was computed accordingly in order to achieve 923 K (650°C) of air outlet temperature.

As far as concerning the geometry of the cavity, simulations were performed to evaluate the effect of parameters such as:

- internal tube diameter;
- glass thickness;
- chrysalis pitch;
- internal height.

2.4. Preliminary CFD result

In this section the first simulation performed is reported. The input power was assumed to be uniformly applied to all the internal surfaces of the cavity. Assuming no heat-flux through all the opaque surfaces, the simulation results show that 89.6 % of the total input power is gathered by the HTF; instead, 9.8 % represents the heat losses from the external surface of the glass. The simulation was considered complete once the power unbalance, between the input power and the sum of the power gathered by the HTF and the amount lost through the glass, was lower than 1% of the input power. This is the reason why the algebraic sum of the power gathered by the air and the power lost may not be exactly equal to the input power.

The temperature distribution into the cavity is depicted by Figure 3. Since the cold air is pumped through the chrysalis from the bottom, the fluid temperature, as well as the temperature into the cavity, increases until a maximum at the top of the cavity.

It is worth to remind that the incoming energy was uniformly distributed on the inner walls. The real working conditions could be severely different from this initial assumption. The presence of a radiation skew angle can already lead to a strong non-uniformity as shown in the next section.

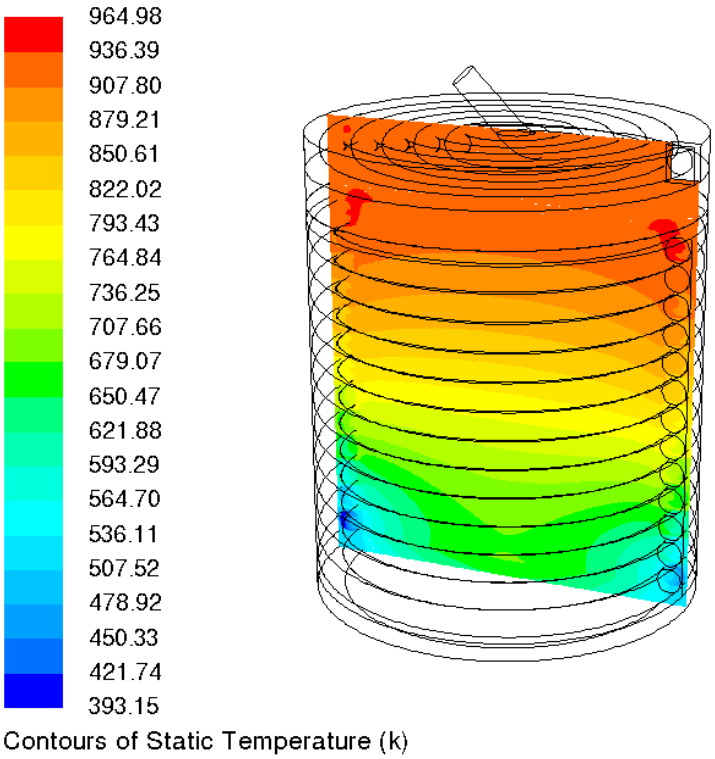

FIGURE 3: CHRYSALIS TEMPERATURE DISTRIBUTION AT STEADY STATE CONDITION.

2.5. Effect of the skew angle on the receiver performance

The skew angle indicates the inclination of incoming solar radiation with respect to the direct normal irradiation (DNI) condition. The higher the skew angle the more the solar concentration decreases due to end-losses (i.e. fraction of energy, reflected from the primary optics, that falls beyond the receiver [3]) and longer travel paths of the rays from the point of their reflection on the primary mirrors to the point of their absorption.

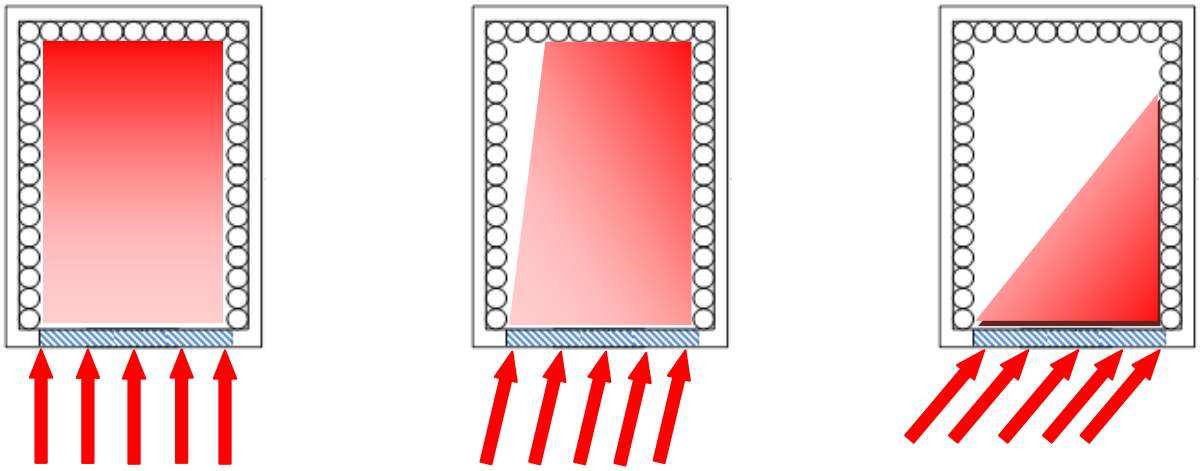

FIGURE 4: SCHEMATIC OF SKEW ANGLE EFFEC: SKEW 0°, SKEW 18°, AND SKEW 40° RESPECTIVLY.

The real-scale receiver prototype, which will be built in Morocco, will not be perfectly positioned towards north-south direction due to the ground conformation; therefore, the assessment of the receiver performance, operating under the two reference skew angles of 18° and 40°, given by the misalignment, are of particular interest.

To analyze the effect of the skew angle on the receiver performance, CFD simulations were performed applying the relative input power only to the internal surfaces which are actually irradiated. The exact energy distribution into the cavity was obtained from the ray-tracing simulations, performed by Airlight. Based upon the latter, the reference skew angles were simulated with the following energy distribution:

- **Skew 18°**: the input power was uniformly distributed onto one half of the lateral surface and a fraction, based upon the height of the cavity, to the top.

- **Skew 40°**: at this skew angle, with the given geometric dimensions of the cavity, the input power is only absorbed by a quarter of the lateral surface. To reproduce an even more realistic condition, the power distribution was modelled as linearly decreasing from the maximum amount near the internal glass surface.

Furthermore, both the simulations were run twice varying the convective heat transfer coefficient of the external glass surface between two reference values. Simulations results showed that, for both the cases, the air outlet temperature was below the target value of 923 K. This means that, for the preliminary analytical computation of the mass flow rate necessary as boundary condition of the CFD simulation, the power losses through the glass were probably underestimated. The results obtained were anyway representative of the cavity behavior with a skew angle and the tests, very expensive in terms of CPU time, were not replied for different values of the air mass flow rate. Among the results of these tests, in the case of skew 40°, the heat losses from the glass window account for about 27 % of the total input power. Despite the amount of power removed by the air flow is still remarkable, this is clearly a non convenient working condition since the hot region into the cavity is closer to the glass surface than to the cavity top. This condition reduces the cavity efficiency of more than 17% with respect to the case without skew.

2.6. Receiver set-back analysis

A new design solution, referred to hereinafter as the set-back, was analyzed. The latter aims at reducing the power losses through the window by moving away from the glass the lower hot region of the cavity. If the set-back distance is lower than a threshold value, the energy distribution into the cavity is not affected; the only difference is that part of the incoming energy is absorbed by the bottom surface of the first spiral circle. Considering the dimensions of the entire receiver and the space availability, two reference set-back distances were proposed. Therefore, two new computational grids were built and then simulated under the two reference skew angles conditions in order to evaluate how the set-back affects the receiver performance.

The 3D CFD simulations results showed that the two set-back cases analyzed do not lead to any relevant difference. It means that the height difference between the two reference set-back values is actually too small to produce a sensible effect on the final result. In order to prove this theory, a new simulation was performed implementing an unrealistic cavity set-back of 0.5 m. In this case, since the external surfaces of the cavity were adiabatic, the power lost through the glass surface was effectively lower than the reference cases. CFD simulations led to the evidence that the two values selected for the set-back distance do not sensibly affect the receiver behaviour; therefore, as final solution, the lower set-back distance, between the two reference values, was selected. Besides some constructive advantages, the main benefit provided by this solution is that the lower the set-back the lower the energy losses due to a smaller surface area for heat transfer.

Additional CFD simulations were performed to model the cavity behaviour when increasing the internal diameter of the absorber tube and reducing the internal cavity diameter. The main effect of increasing the absorber tube diameter, keeping the same air mass flow rate, is to reduce the pressure drop through the cavity. No relevant radiation-to-thermal efficiency variations were found. On the contrary, a reduction of the spiral pitch leads to a small increase of the cavity receiver efficiency.

2.7. Effect of the cavity height variation

In this paragraph the effect of varying the cavity height is analyzed. The absorber tube diameter was increased to further reduce the pressure drop through the cavity.

From the first cases analyzed, it is visible that increasing the height of the cavity leads to increase its radiation-to-thermal efficiency for the skew 18° working condition. In the case of skew 40°, since the solar energy is absorbed by the same number of spiral rings, increasing the cavity height seems to be not convenient. This will be better seen in Figure 5 and Figure 6 where temperature contours for the cavities are shown.

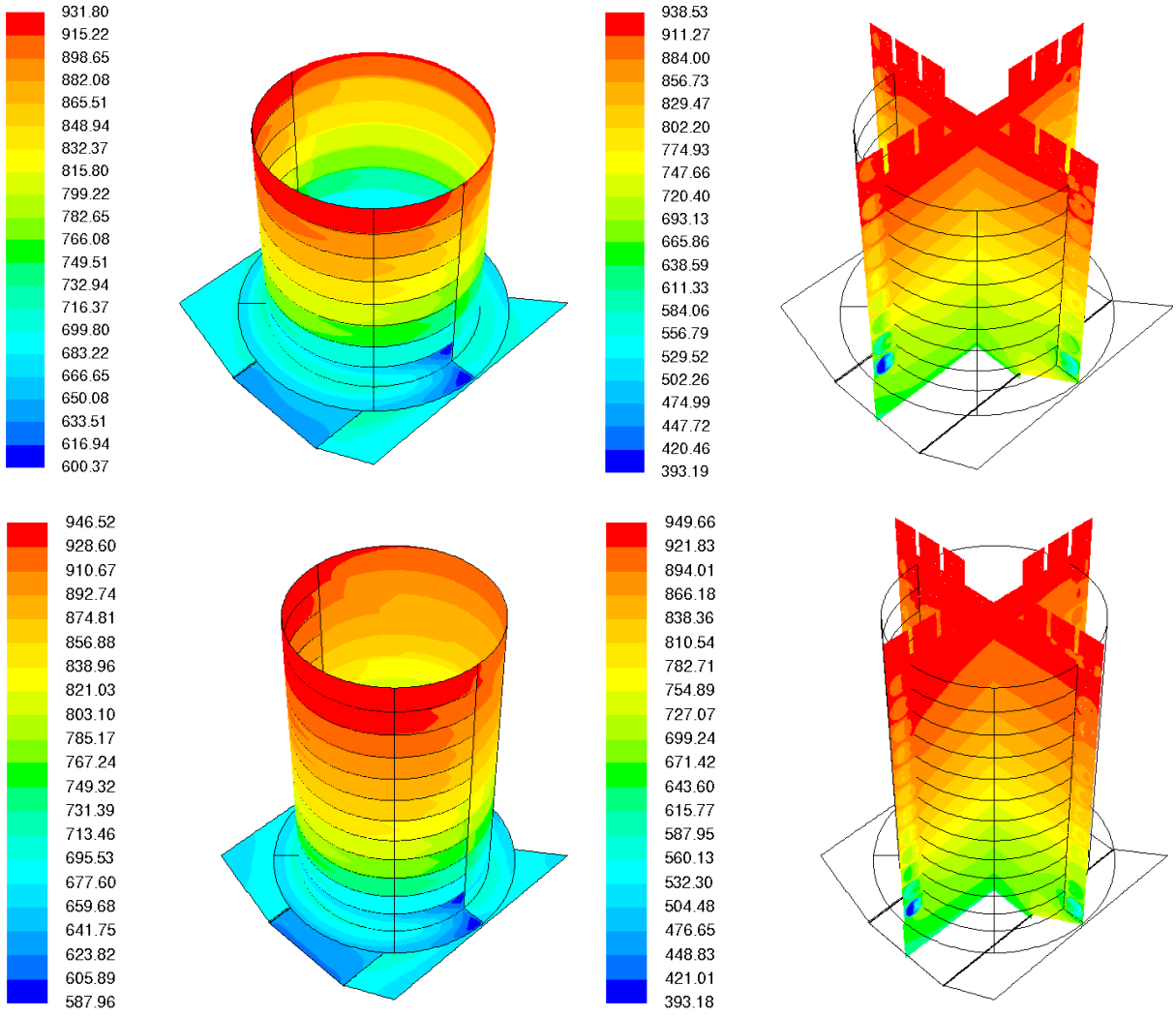

FIGURE 5: CONTOURS OF TEMPERATURE INTO THE CAVITY IN THE CASE OF SKEW 18° WORKING CONDITION (L.H.S.: INTERNAL SURFACES; R.H.S.: CUTTING PLANES); COMPARISON OF CAVITIES WITH DIFFERENT HEIGHTS. TEMPERATURE VALUES ARE IN K.

L.h.s. of Figure 5 shows the temperature distribution of the internal surface of the absorber tube for the skew 18° working condition. The incoming solar radiation impacts onto half of the internal surfaces, as well as onto the top, for both the reference heights. In this case, increasing the height of the cavity leads to improve its performance since the surface area, useful for heat transfer, increases while the incoming solar radiation remains the same.

R.h.s. of Figure 5 shows, instead, two perpendicular cutting planes which allow to visualize the stratification of the internal temperature of the cavity. It is worth to remind that, for all the simulations, the convective heat transfer contribution into the internal air volume of the cavity was not accounted for.

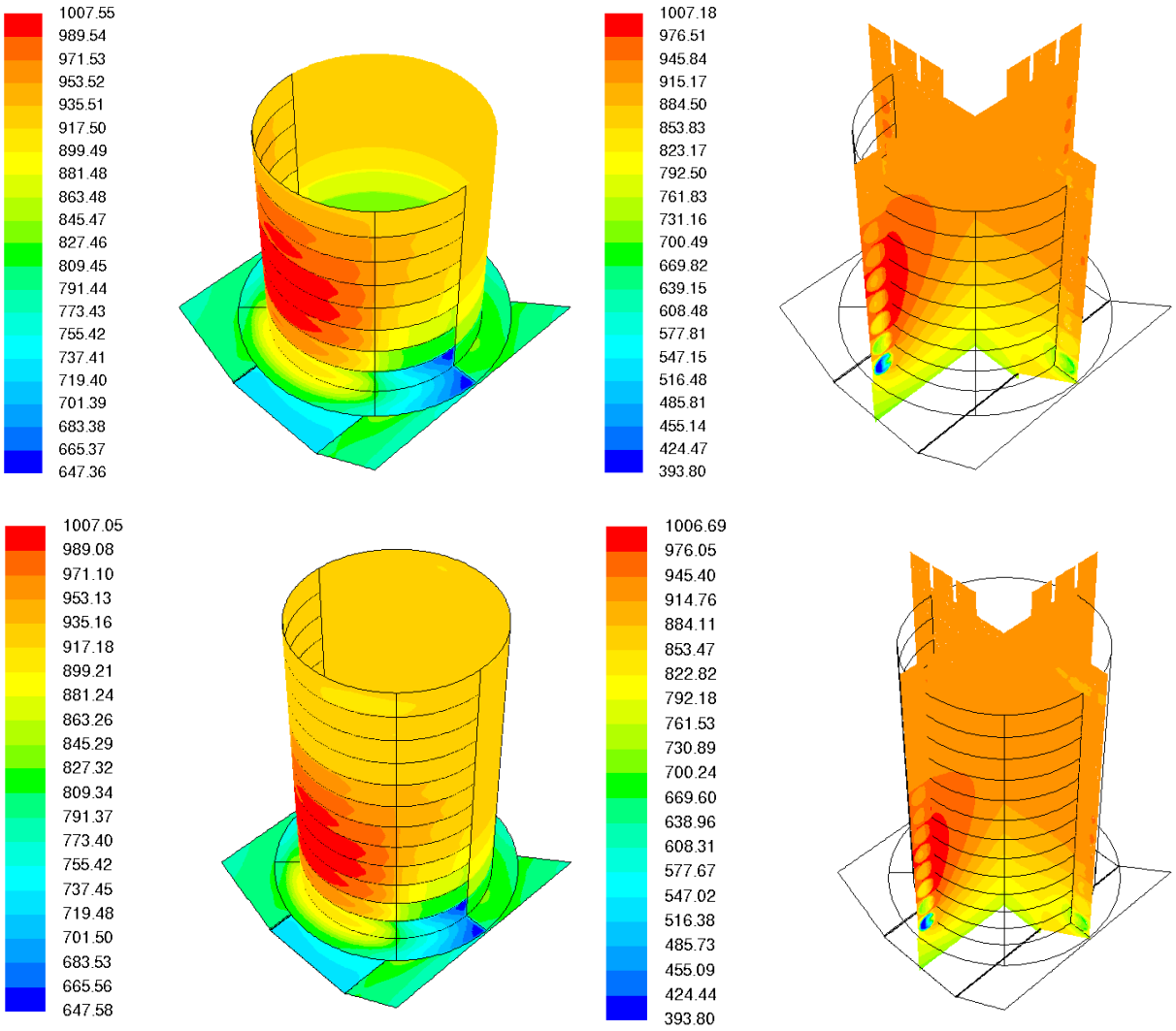

FIGURE 6: CONTOURS OF TEMPERATURE INTO THE CAVITY IN THE CASE OF SKEW 40° WORKING CONDITION (L.H.S.: INTERNAL SURFACES; R.H.S.: CUTTING PLANES); COMPARISON OF CAVITIES WITH DIFFERENT HEIGHTS. TEMPERATURE VALUES ARE IN K.

Figure 6 depicts the cavity working at skew 40° condition. With this high skew angle, incoming solar energy impacts directly onto a quarter of the internal surface. The radiation-to-thermal efficiency is lower than the previous case because, as clearly visible in the l.h.s. of Figure 6, with this high skew angle, incoming solar energy impacts directly onto a quarter only of the internal surface creating a hot spot close to the external glass window and no more on the top. In this case, increasing the height of the cavity does not lead to improvements since all the upper spiral rings are not reached by the incoming power. Based upon these results, the most efficient cavity height would be in between the two values analyzed.

The same tests were performed on the model of the cavity with a reduced pitch. For these cases, increasing the cavity height leads to slightly improve its performance for both the skew angle conditions. A graphical presentation of these results is reported in Figure 7 and Figure 8 showing the temperature contours.

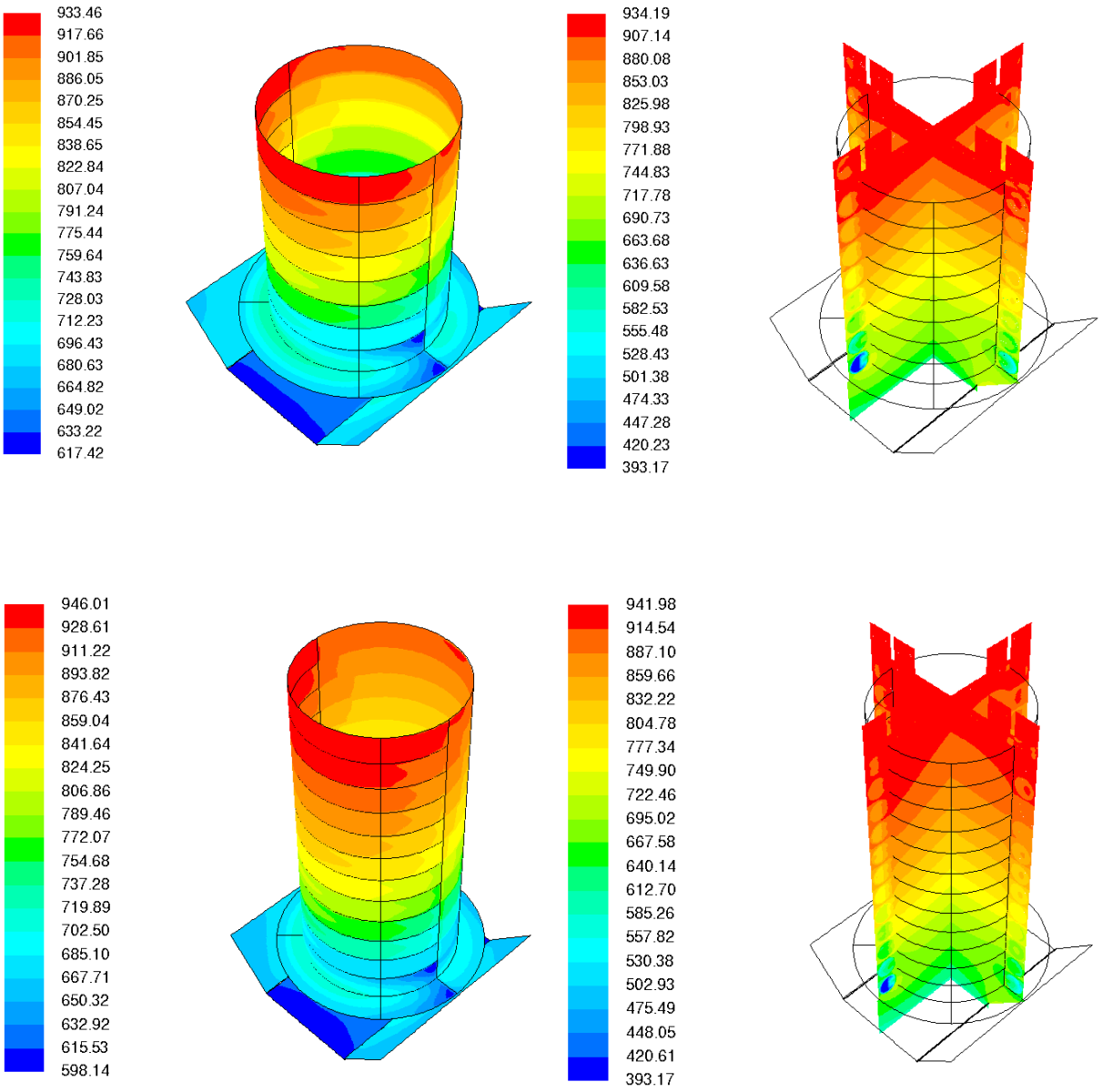

FIGURE 7: CONTOURS OF TEMPERATURE INTO THE CAVITY IN THE CASE OF SKEW 18° WORKING CONDITION (L.H.S.: INTERNAL SURFACES; R.H.S.: CUTTING PLANES); COMPARISON OF CAVITIES WITH DIFFERENT HEIGHTS. TEMPERATURE VALUES ARE IN K.

Regarding the skew 18° working condition, no appreciable differences can be observed with respect to the previous cases of cavity with larger internal diameter. In these cases also, the incoming power is uniformly distributed onto half of the internal surface and onto the top.

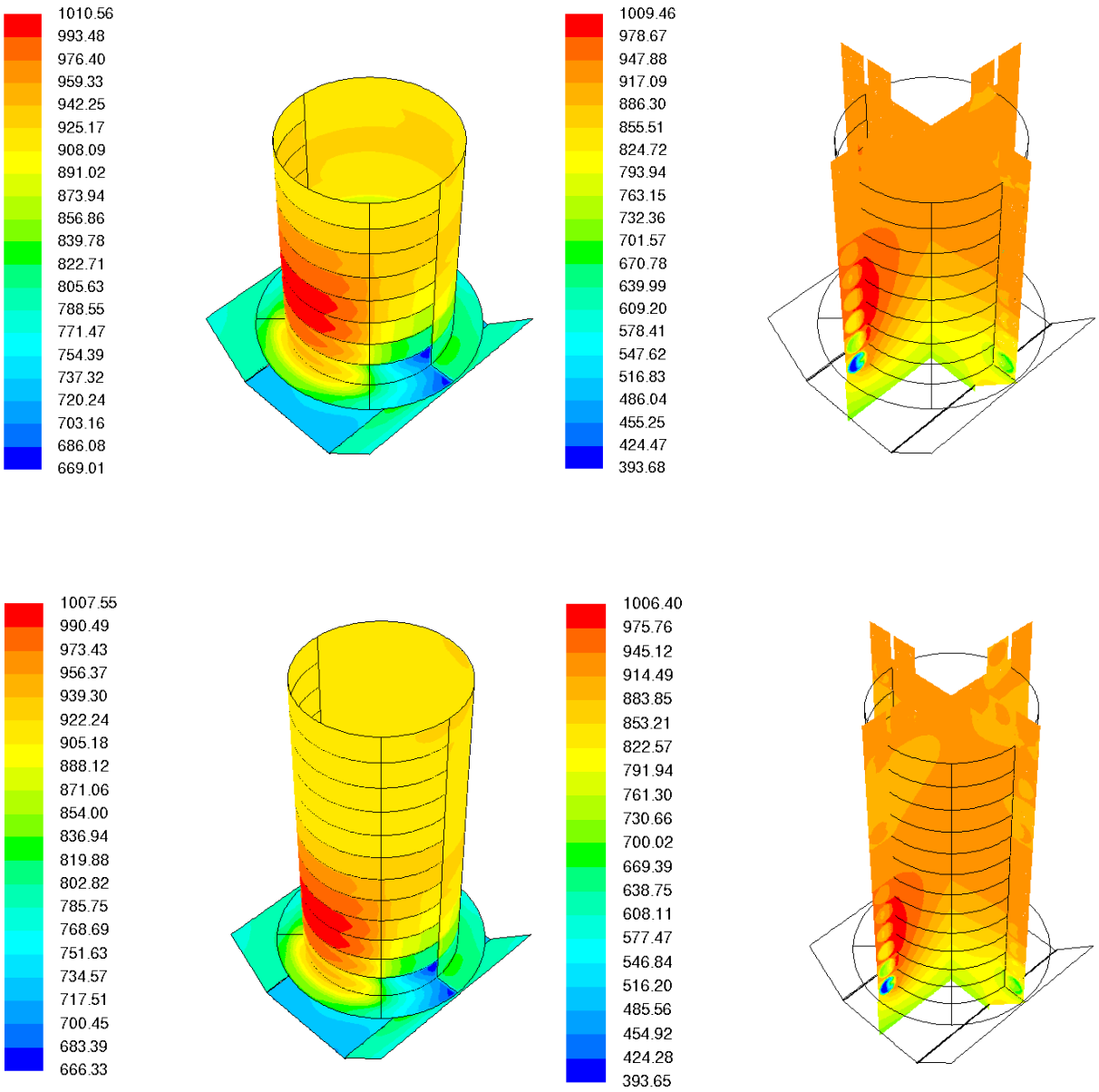

FIGURE 8: CONTOURS OF TEMPERATURE INTO THE CAVITY IN THE CASE OF SKEW 40° WORKING CONDITION (L.H.S.: INTERNAL SURFACES; R.H.S.: CUTTING PLANES); COMPARISON OF CAVITIES WITH DIFFERENT HEIGHTS. TEMPERATURE VALUES ARE IN K.

As depicted by Figure 8, the hot spot due to the incoming energy, onto the lower quarter of internal surface, is closer to the glass window. This because, reducing the internal diameter, the height reached by the incoming energy, especially at high skew angle, reduces accordingly. With the given dimensions, the last absorbed tube winding is not affected by the incoming solar radiation already for the smaller height. It means that, an excess of increase in cavity height may leads to a strong reduction of the HTF outlet temperature.

2.8. Analysis of the cavity without top coils

In all the simulations performed so far, the cavities were modelled with windings at the top which aims at harvesting the largest part of incoming energy. At the same time, this concept makes more difficult the manufacturing of the chrysalis itself and therefore, it was decided to remove the windings of the cover replacing them with a metal plate. This last version of the cavity was already introduced in l.h.s. of Figure 1. To assess the impact of the new design on the cavity performance, a new series of CFD analysis were performed. The tests were basically the same already extensively reported in paragraph 2.7 with the difference that the cavity has no winding onto its top.

The comparison between the actual CFD simulations results with the previous (paragraph 2.7), allowed to observe that substituting the top windings with a metal plate does not make a sensible difference for the skew 18° working condition; as far as concerning skew 40° a small improvement can be observed since, in the previous cases, the last windings were not hit by the incoming solar energy and therefore, removing them is useful because the fluid leaves the absorber tube earlier and at higher temperature. It is worth to note that, the pressure drop through the absorber tube is lower since the tube itself is shorter; therefore, the pumping power reduces accordingly. Figure 9 and Figure 10 depict the temperature distribution into the cavity for the two reference skew angles and for the two cavity heights.

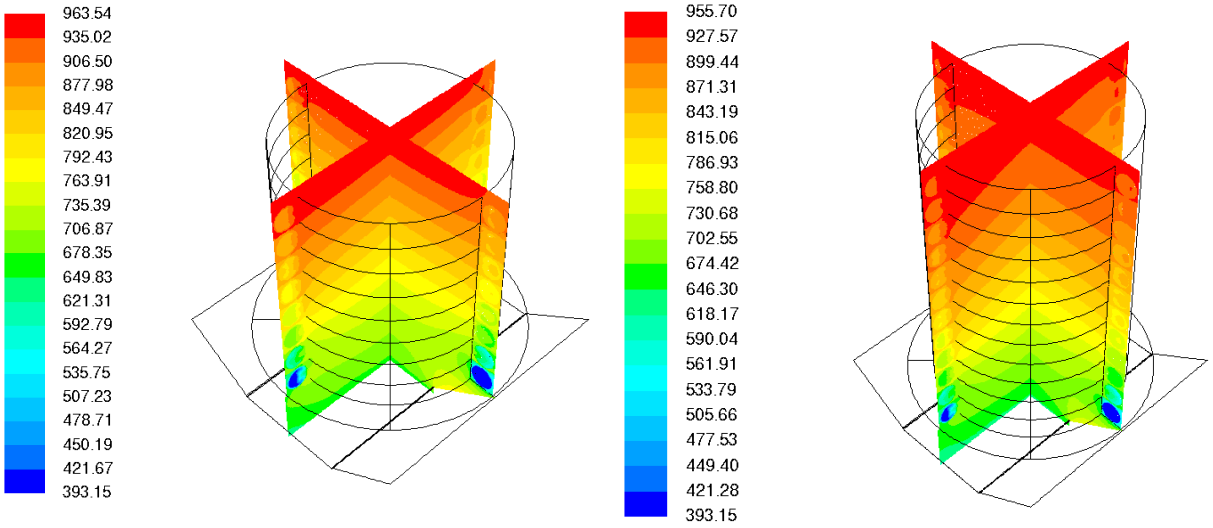

FIGURE 9: TEMPERATURE DISTRIBUTION INTO THE CAVITY IN THE CASE OF SKEW 18° WORKING CONDITION FOR THE LOWER (L.H.S.) AND THE HIGHER (R.H.S.) CAVITY HEIGHT RESPECTIVELY; TEMPERATURE VALUES ARE IN K.

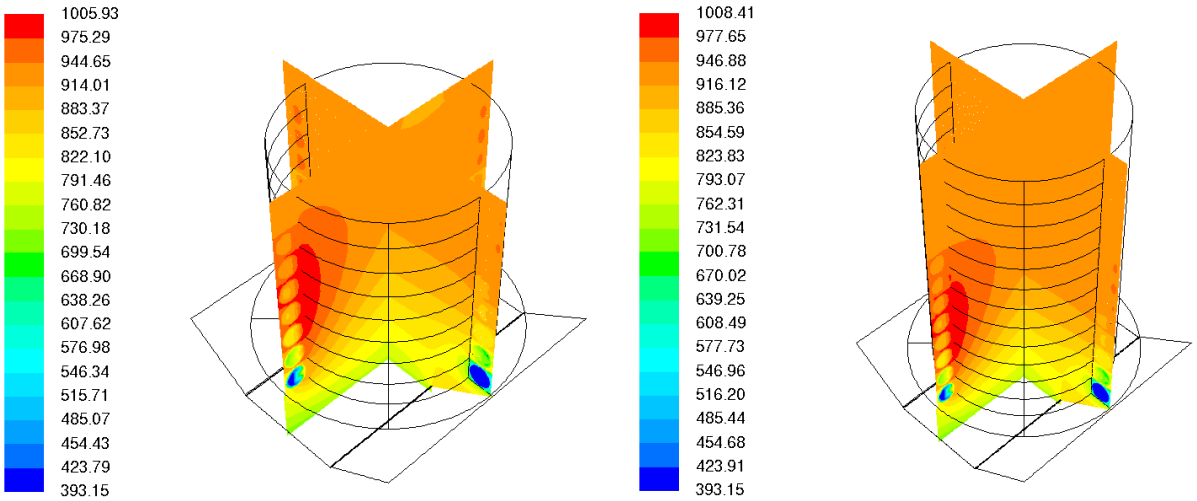

FIGURE 10: TEMPERATURE DISTRIBUTION INTO THE CAVITY IN THE CASE OF SKEW 40° WORKING CONDITION FOR THE LOWER (L.H.S.) AND THE HIGHER (R.H.S.) CAVITY HEIGHT RESPECTIVELY; TEMPERATURE VALUES ARE IN K.

As far as concerning the cavity with smaller internal diameter, the trend of the CFD simulations results is essentially the same. For the skew 18° working condition and the cavity with smaller height, the efficiency is slightly lower since the useful area for the heat transfer is lower. The radiation-to-thermal efficiency is not different any more if the higher cavity is considered. In this case, the incoming solar energy absorbed from the top is very small and thus it does not lead to an appreciable effect when the top windings are removed. As far as concerning skew 40° working condition, a small improvement can be observed removing the windings at the top. The temperature distribution into the cavity for the reference working conditions and different heights are shown Figure 11and Figure 12.

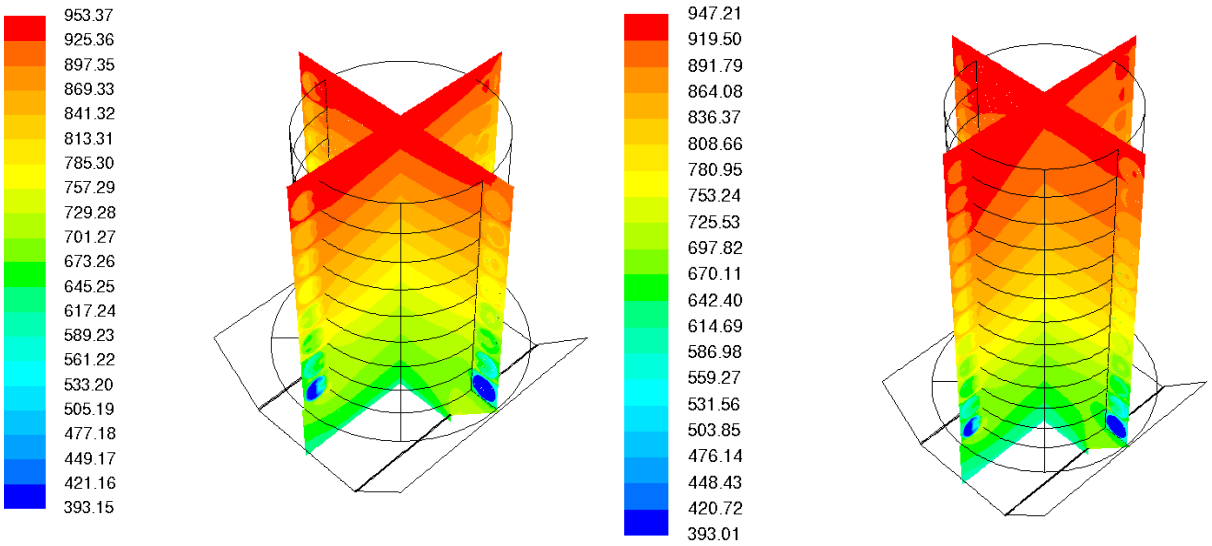

FIGURE 11: TEMPERATURE DISTRIBUTION INTO THE CAVITY IN THE CASE OF SKEW 18° WORKING CONDITION FOR THE LOWER (L.H.S.) AND THE HIGHER (R.H.S.) CAVITY HEIGHT RESPECTIVELY; TEMPERATURE VALUES ARE IN K.

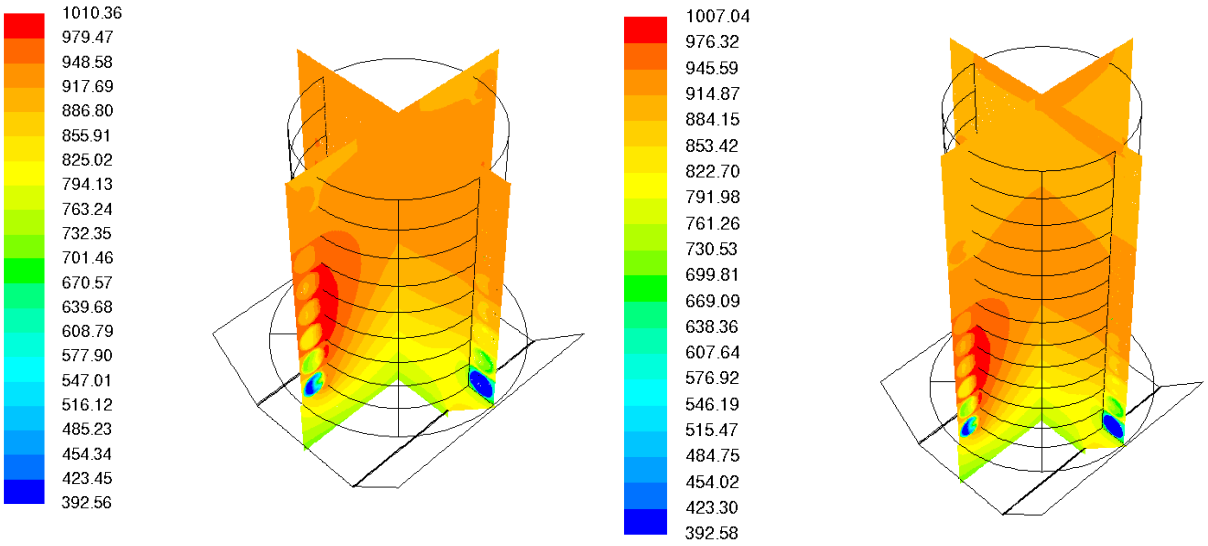

FIGURE 12: TEMPERATURE DISTRIBUTION INTO THE CAVITY IN THE CASE OF SKEW 40° WORKING CONDITION FOR THE LOWER (L.H.S.) AND THE HIGHER (R.H.S.) CAVITY HEIGHT RESPECTIVELY; TEMPERATURE VALUES ARE IN K.

2.9. Conclusions

A detailed 3D steady-state CFD simulations campaign was performed with the aim of evaluating the thermo-fluid dynamics behaviour of the new receiving cavity when subjected to the variation of various main parameters such as:

- internal diameter of the absorber tube;
- chrysalis pitch;
- internal height;
- glass thickness;
- skew angle of incoming solar energy;
- receiver set-back.

By combining all the CFD simulations results shown above, it was possible to obtain a first optimization of the chrysalis receiver design which will be tested onto the real scale prototype.

2.10. References

[1] G. Raithby and E. Chui, “A finite-volume method for predicting a radiant heat transfer in enclosures with participating media,” Journal of Heat Transfer, vol. 112, pp. 415 – 423, 1990.

[2] E. Chui and G. Raithby, “Computation of radiant heat transfer on a non-orthogonal mesh using the finite-volume method,” Numerical Heat Transfer - Part B, vol. 23, pp. 269 – 288, 1993.

[3] W. Stine and M. Geyer, “Power from the sun,” 2001. [Online]. Available: www.powerfromthesun.net.

Chapter 3

Cavity theoretical model

Contents

List of Figures

List of Tables

3.1. Introduction: problem description

A mathematical model of the cavity has been implemented at ETHZ. The model validation by means of CFD simulations and experimental tests will lead to a more flexible mean to analyze geometry variations of the system.

The main geometric parameters taken into account are:

- the outer tube diameter d_{tube};
- the cavity diameter d_{cavity} measured from one tube centre to the opposite tube centre;
- the number of loops n_{loop}.

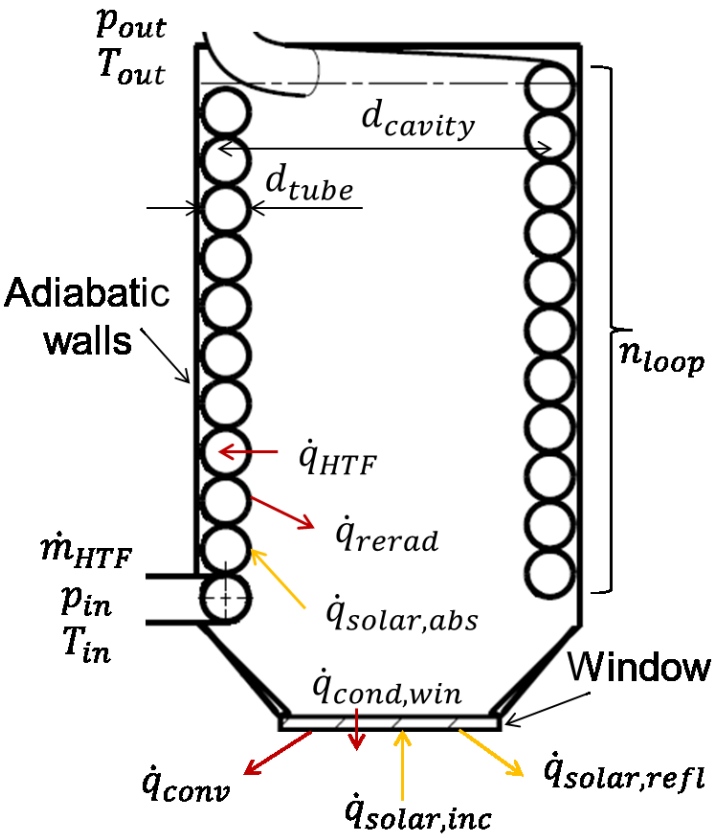

FIGURE 1: DIMENSIONS AND HEAT TRANSFERS OF A HELICAL COILED TUBE CAVITY.

The thermal performance of such a cavity may be defined as the ratio of the heat transferred to the heat transfer fluid (HTF) to the solar power incident on the cavity:

$$\eta_{th} = \frac{\dot{q}_{HTF}}{\dot{q}_{solar,inc}}$$

The performance in terms of pressure drop is best characterized by the specific pumping power demand, which is defined here as the share of pumping power demand in total expected electric power output:

$$\varepsilon_{pump} = \frac{\dot{w}_{pump}}{\eta_{th-el}\dot{q}_{HTF}}$$

In the above formula $\eta_{th\text{-}el}$ denotes the thermal-to-electric efficiency of the power block, which may be assumed around 35%.

The overall receiver performance of a coiled tube cavity may then be expressed as:

$$\eta_{rec} = \frac{\dot{q}_{HTF} - \dot{w}_{pump}/\eta_{th-el}}{\dot{q}_{solar,inc}} = \eta_{th}\left(1 - \varepsilon_{pump}\right)$$

which takes into account the pumping power requirement weighted by the thermal-to-electric conversion efficiency. Furthermore, as solar power plants inevitably deal with transients (daily start-up/shut-down, clouds), a fourth important quantity is the thermal inertia and hence the material use of a solar receiver, which should be minimized to reduce parasitic losses. The total amount of steel used for the helical pipes in a 212 m long receiver may be calculated by

$$m_{steel} = \rho_{steel} \cdot \frac{2 \cdot L_{rec}}{d_{cavity} + d_{tube}} \cdot n_{loop} \sqrt{\left(\pi d_{cavity}\right)^2 + d_{tube}^2} \cdot \pi (d_{tube} - t_{tube}) \cdot t_{tube}$$

where ρ_{steel} is the density of steel, L_{rec} the receiver length and t_{tube} the thickness of the pipe wall.

Consequently the objective is to find a set of geometric parameters (d_{tube}, d_{cavity}, n_{loop}) that yield maximum receiver efficiency at minimum material cost.

Preliminary to this analysis the effect of the window on the heat losses is studied by comparison of windowless and windowed cavities and the receiver performance is assessed with two different secondary concentrators, a linear and a point-focusing design achieving total geometric solar concentration ratios of 100 and 300 suns respectively.

3.2. Preliminary studies

3.2.1. Effect of window on heat losses

Heat losses due to natural convection are estimated using the modified Clausing and modified Stine models by Leibfried and Ortjohann [1] for windowless cavities and the correlation by Fujii and Imura [2] for free convection at the window. The optical properties of the anti-reflection coated window are provided by the supplier and losses due to reflection and absorption by the window are taken into account.

3.2.2. Influence of solar concentration on performance

The optical efficiencies of the linear trumpet and the point-focusing crossed design are determined using Monte Carlo ray-tracing. In addition the thermal efficiencies of two similar cavities but with different opening areas corresponding to the concentration ratios are calculated using a simplified one-dimensional model. Finally the products of optical and thermal efficiencies of the two configurations are compared to each other.

3.3. Heat transfer model of coiled tube cavity

The main objective of this model is to calculate the air outlet temperature and the pressure drop of the coiled pipe as a function of the geometric parameters and the operating variables (air inlet temperature, mass flow rate, solar radiation conditions), which enables the characterization of thermal efficiency and pumping power requirement for such a cavity. In addition the different heat loss mechanisms are quantified, facilitating the identification of improvement opportunities. Furthermore the model shall be used to predict the temperature distribution on the cavity and window surfaces to verify that material constraints are met.

3.3.1. Radiation

The incident and reflected solar energy at the window, the fraction of energy absorbed in the glass, and the distribution of the transmitted solar energy on the cavity walls are determined by Monte Carlo ray-tracing simulations of the complete optical system including ETFE top foil, primary mirror and secondary optics. These quantities are independent of the actual cavity temperature and hence may be determined a priori for any given design and solar irradiation level and integrated into the heat transfer model as source terms. The simulations are carried out with VEGAS [3], an intensely validated in-house code developed at the Professorship of Renewable Energy carriers (PRE) at ETH.

The radiative exchange between the cavity surfaces, the window segments and the environment due to thermal emission is modelled by means of the gray-band approximated radiosity method for semi-transparent windows using two spectral bands. The first band reaches up to 2’700 nm and covers in approximation the solar spectrum, to which the glass is transparent. In the second spectral band at higher wavelengths the window may be treated as completely opaque and emission from the outer window surface to the environment is included separately. The view factors between surface segments are partially calculated analytically and partly determined by Monte Carlo ray-tracing.

3.3.2. Convection

Internal flows in helically coiled pipes have been studied extensively due to their wide use in industry. In particular coiled tubes are interesting for heating and cooling applications because centrifugal forces cause a secondary flow of the form of a vortex pair, which leads to an enhanced convection heat transfer coefficient without causing excessive pressure drop as it occurs e.g. in turbulent flows. In order to keep the pumping power demand at a low level it is desirable to design the coil cavity in such a way that the flow in the helical tube stays laminar under all operating conditions. Accordingly the Fanning friction coefficient and the Nusselt number may be calculated by means of correlations from literature for fully developed laminar flow in helically coiled tubes. Here the correlations by Manlapaz and Churchill (1980, 1981) are utilized.

3.3.3. Conduction

Heat conduction is taken into account only from the inner window surface facing the cavity to the outer window surface seeing the environment, because there is a significant temperature gradient across the insulating glass. As the model is also used to detect hot spots, conduction is not included inside the cavity because of its smoothing effect on temperature peaks. However, as the helical tube walls are thin and the thermal conductivity of steel is rather low, heat conduction is expected to be relatively unimportant compared to the radiative exchange inside the cavity. It is further noted that the model deals with the helical tube cavity only, i.e. the outer cavity walls are assumed as adiabatic and conduction heat losses through the insulation are not considered by the model.

3.4. Results and conclusions

3.4.1. Effect of window

The heat losses predicted by the modified Clausing and Stine models [1] of an open cylindrical cavity are compared to the losses occurring at the window of a similar but closed cavity in Figure 2. The comparison is shown for the full range of daily cavity inclination angles (90°: downward facing, 0°: horizontal), which are a result of the one-axis tracking motion. In both cases the wall temperature is set to 650°C and the cavity opening area amounts to 15 cm^2, corresponding to a geometric concentration of 300 suns. Taking into account the solar radiation losses due to reflection at the window (8% of maximum solar power incident on the window), the closed cavity still performs better over the day. This applies even more if less concentrating, linear secondary optics are used, which requires larger cavity openings.

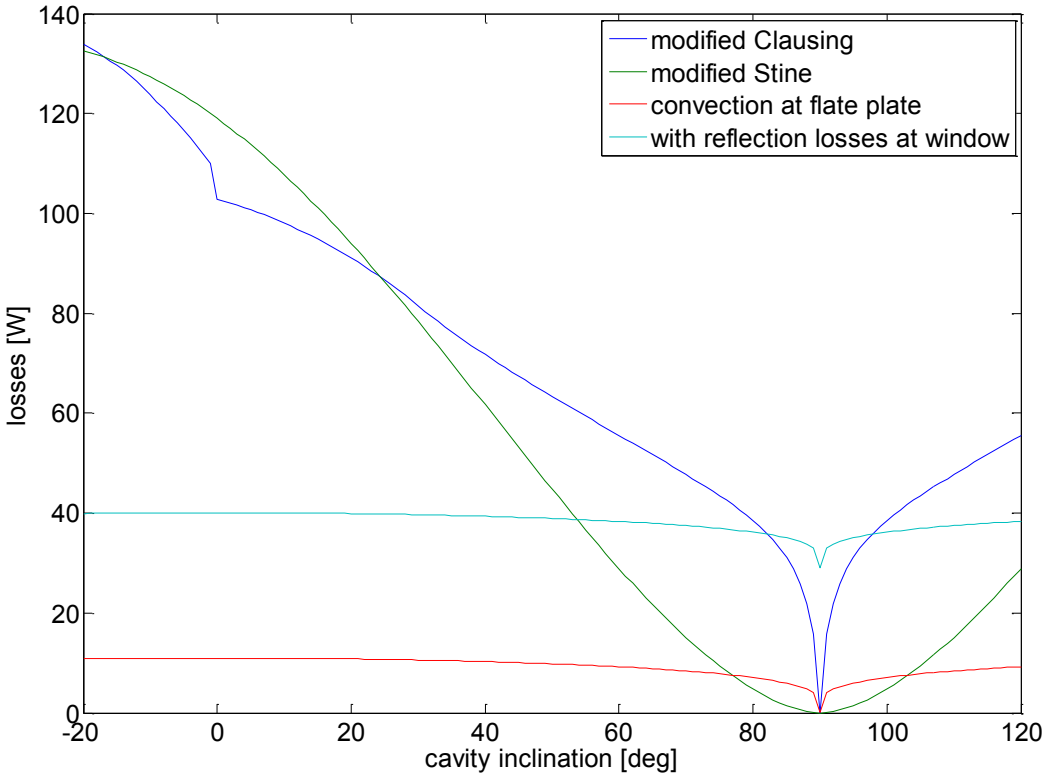

FIGURE 2: COMPARISON OF NATURAL CONVECTION LOSSES OF OPEN AND WINDOWED CAVITIES.

3.4.2. Influence of concentration

It is found that in spite of the increased thermal efficiencies achieved with 3-D secondary concentration the total performance of the system is comparable to that obtained with the line focus secondary concentrator, which is due to the inferior optical efficiency of point-focusing secondary optics with respect to the linear trumpet. As a consequence, considering the complexity added to the system by using 3-D crossed designs, only designs using the 2-D trumpet secondary stage are analyzed in the following.

3.4.3. Performance map of various coiled tube cavity designs

In order to find appropriate cavity dimensions a large number of simulations is performed for varying tube diameters, cavity diameters, numbers of loops and skew angles. Here the first three parameters define the geometry of the coiled tube cavity and the simulated values are summarized in Table 1.

TABLE 1: GEOMETRIC PARAMETERS USED IN SIMULATIONS.

Parameter	Values
d_{cavity}	80, 88, 100 120 mm
n_{loop}	5, 10, 15, 20 loops

The fourth variable represents different sun positions. The annual efficiency of a specific design is then obtained by an average of the efficiencies at certain skew angles weighted by the yearly direct normal irradiance (DNI) collected by the optical system at the corresponding angles. In the results presented below, the yearly DNI collected by a north-south oriented one-axis tracking system in Ait Baha (Morocco) is used as weighting function. The air inlet and outlet temperatures are kept constant over all runs at 120°C and 650°C respectively and the mass flow rate is adapted accordingly.

Figure 3 shows the thermal performance as a function of specific pumping power demand of the 4^3 = 64 different designs, coloured with respect to the cavity diameter. Obviously the desirable region is in the upper left corner, whereas designs in the lower right corner indicate a bad choice of parameters. It is observed that the smaller the cavity diameter becomes, the closer the desired region is approached, indicating that this parameter should be chosen as small as possible with respect to manufacturing.

The thermal performance and the pumping power in percentage of expected electric power output of these designs are consolidated in the receiver performance in Figure 4 and plotted as a function of the amount of steel needed for the number of helical tubes in a 212 meter long receiver.

It is seen that there seems to be an optimum in terms of receiver performance between 10 and 15 cooling loops. For lower numbers of loops the efficiency drops whereas for higher numbers the material use increases without any gain in performance. Furthermore the graph shows that the influence of the tube diameter on the receiver efficiency is strongly dependent on the choice of the other two parameters.

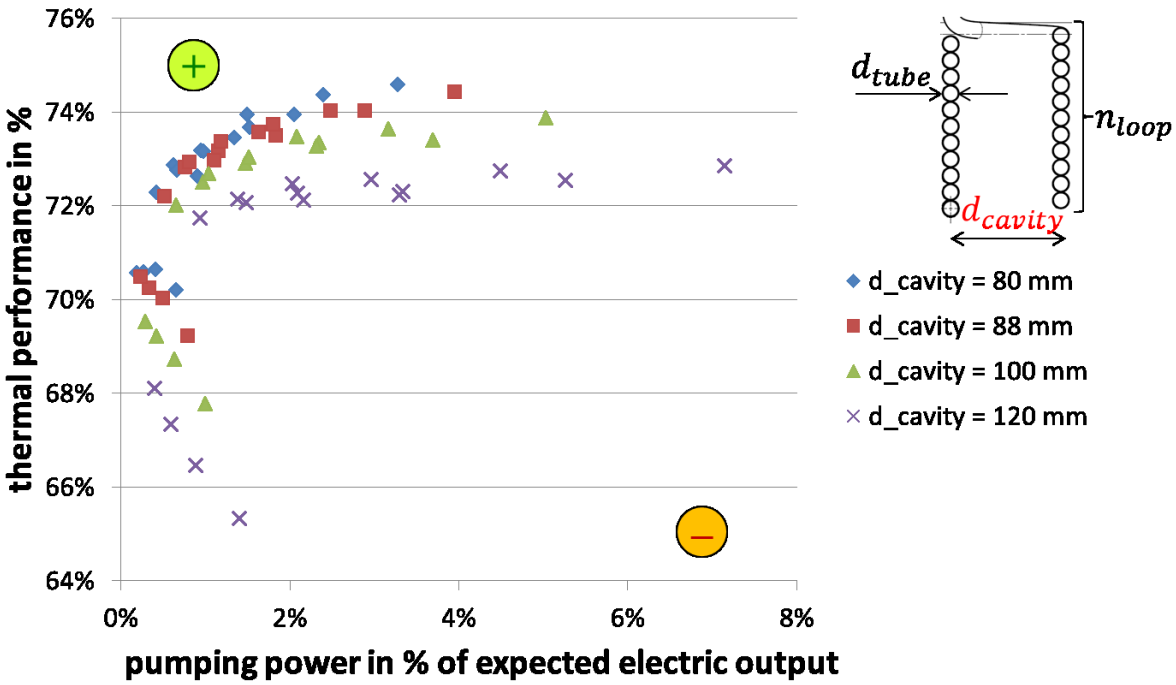

FIGURE 3: THERMAL PERFORMANCE AS A FUNCTION OF SPECIFIC PUMPING POWER FOR VARIOUS DESIGNS.

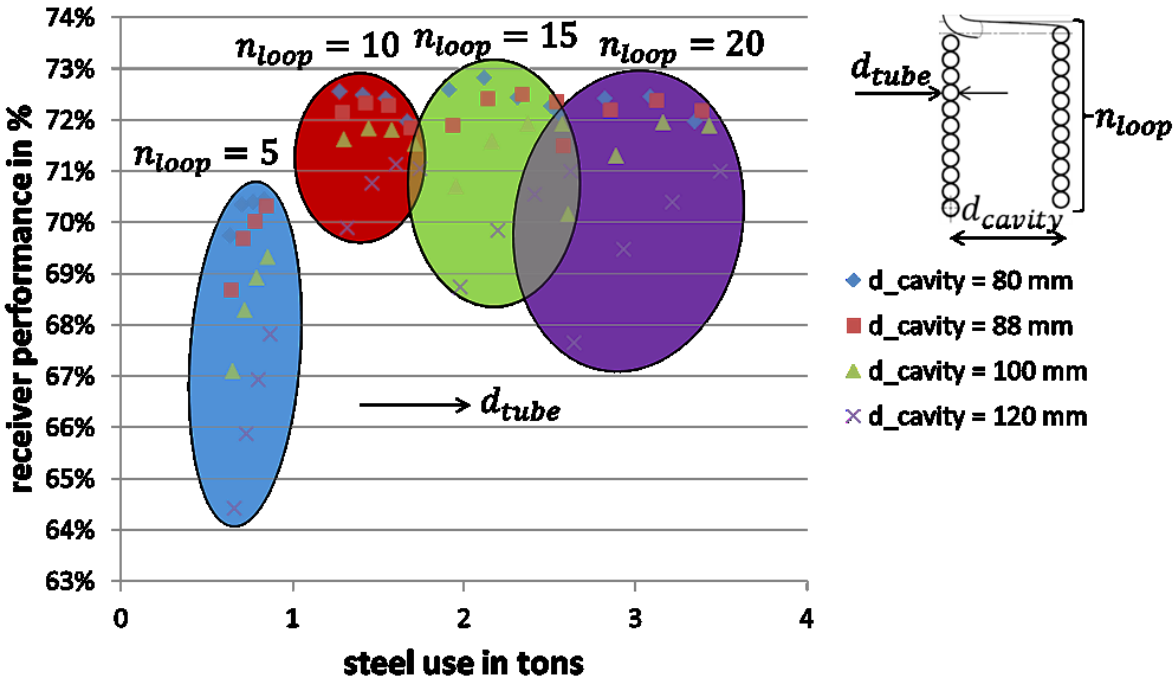

FIGURE 4: RECEIVER PERFORMCANCES AS A FUNCTION IN MATERIAL USED FOR COILED TUBE CAVITIES.

3.5. References

[1] Leibfried U. and Ortjohann J. (1995), Convective Heat Loss from Upward and Downward-Facing Cavity Solar Receivers: Measurements and Calculations, J. Sol. Eng.

[2] Fujii, T., and Imura, H., 1972, “Natural-convection heat transfer from a plate with arbitrary inclination,” Int. J. Heat Mass Transfer 15, p. 755.

[3] Petrasch, J., 2010, “A Free and Open Source Monte Carlo Ray Tracing Program for Concentrating Solar Energy Research,” ASME Conference Proceedings, (43956), pp. 125–132.

[4] Manlapaz, R.L., and Churchill, S.W., 1980, “Fully Developed Laminar Flow in a Helically Coiled Tube of Finite Pitch,” Chem. Eng. Comm. 7, p. 57.

[5] Manlapaz, R.L., and Churchill, S.W., 1981, “Fully Developed Laminar Convection from a Helical Coil,” Chem. Eng. Comm. 9, p. 185

THIS PAGE INTENTIONALLY LEFT BLANK

Chapter 4

Analysis of multi-shields thermal insulation

Contents

List of Figures

4.1. Introduction: objectives and problem description

This chapter reports the analysis performed on the radiation shields thermal insulation of the receiver, identified as BRCPHC-7. Based on the previous results reported in [1] new simulations have been performed considering new design solutions for the radiation shields structure.

The simulations considered a radiation shields insulation geometry composed by metallic shields separated by air and calcium silicate spacers. The system thermal insulation will be mainly guaranteed by octagonal metallic radiation shields.

The main objectives of this work are:

- defining the optimal separation distance between the shields;
- defining the optimal shields quantity;
- evaluating the conduction contribution, due to the calcium silicate spacer contacts, on the total receiver heat losses;
- verifying the external wall emissivity influence on the thermal insulation efficiency;
- evaluating the low pressure effectiveness with respect of the multilayer insulation geometry;
- defining an equivalent thermal conductivity for a virtual homogeneous material capable of reproducing the thermal behaviour of the studied complex multilayer geometry;

4.2. Two dimensional CFD analysis

Heat transfer in the insulation system was studied via two dimensional steady state CFD analyses performed using the commercial Fluent 13 code from ANSYS.

This report is structured in four test cases:

- Case 1: radiation shields distance optimization.
- Case 2: radiation shields number optimization.
- Case 3: external emissivity effect.
- Case 4: spacer conductive influence.

4.3. Receiver and thermal insulation concept

The receiver thermal insulation structure is based on metallic octagonal shaped radiation shields, see Figure 1. The receiver materials are, from the innermost, 3 shields made of copper coated stainless steel and the next ones made of copper coated aluminium.

In this study the shields were placed at different distances from each other and their number was changed. In the system prototype the distance between shields was guaranteed by means of calcium silicate spacers.

Solar radiation on the system outer wall was not taken into account.

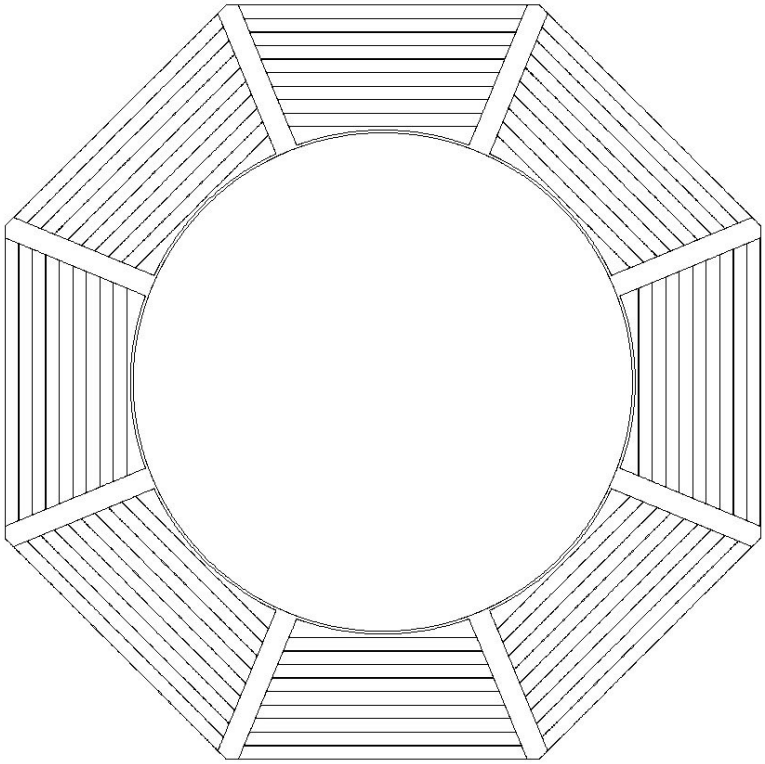

FIGURE 1: OCTAGONAL SHAPED INSULATION GEOMETRY.

4.3.1. Case 1: Radiation shields distance optimisation

A first set of simulations was run to study the influence of the distance between the shields. Therefore, in a thermal insulation system with 10 shields the spacer height was changed from 12 to 15, 20, 30, 40 and 50 mm. All the simulations were run both, with a standard operating pressure (101'325 Pa) and with a low pressure condition (100 Pa) between the shields. This last choice was taken to monitor the convective heat exchange contribution.

The spacer width is 20 mm and the distance from the air duct and the first shield is, at the closest point, 3 mm. Finally, the air duct internal wall temperature has been fixed at 1'173 K.

Computational domain

In order to evaluate natural convention flows and taking advantage of the geometrical symmetry, for the 2D analysis, a sector of 180° of the complete geometry was used (see Figure 2). The computational domain includes the solid regions, made of steel and aluminium, and the regions occupied by air. The external borders of the computational domain are the air duct internal wall and the outer shield.

Computational grid and modelling details

For the radiation shields distance optimization, the computational domains were meshed with Map type Quad elements with a maximal skew of 0.267.

The model was set for a laminar buoyant flow; continuity, N-S, energy and radiation model equations were solved. The radiation model used is The Discrete Ordinates Model [2][3].

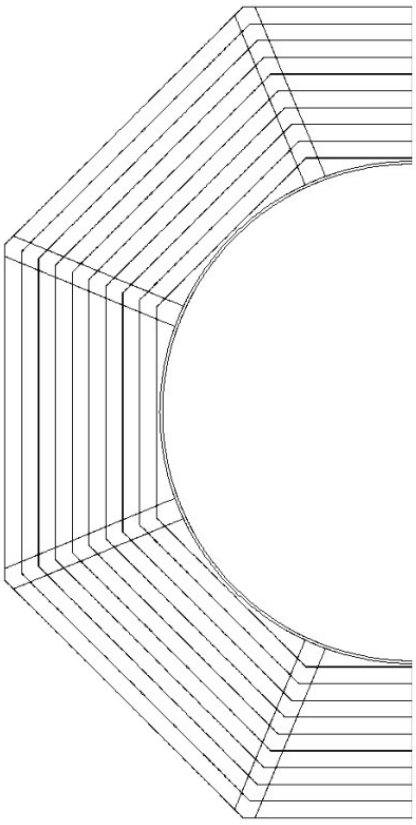

FIGURE 2: COMPUTATIONAL DOMAIN GEOMETRY – SHIELDS DISTANCE 15 mm.

CFD simulations results

Figure 3 shows temperature contours for the high and low pressure cases. Both cases present a stratified temperature distribution between radiation shields with a negligible effect of convective heat transfer.

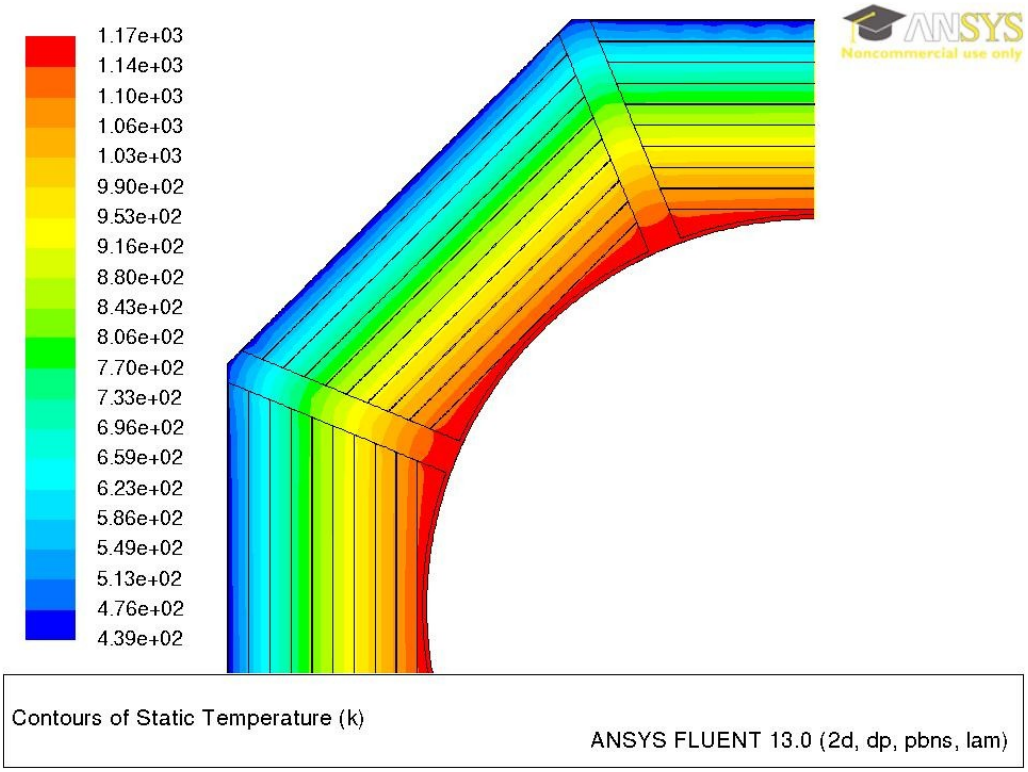

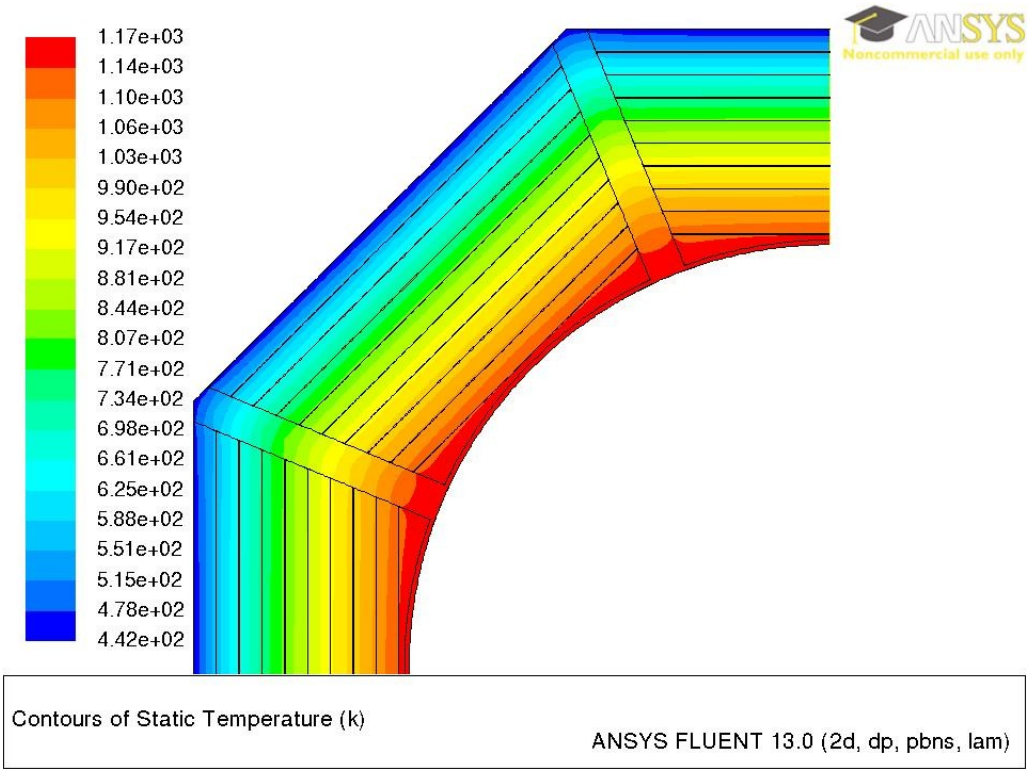

FIGURE 3: STATIC TEMPERATURE DISTRIBUTION FOR OPERATING PRESSURE OF 101'325 Pa (TOP) AND 100 Pa (BOTTOM) - SHIELDS DISTANCE = 12 mm.

Figure 4 shows the velocity vectors for the high and low pressure cases. A similar convective movement of the air between the shields in the two cases is reported though in the case with an operating pressure of 101’325 Pa the velocities are higher. Nevertheless, with a distance of 12 mm between the shields, the convective current speeds result to be in any case too low to significantly affect the temperature distribution and therefore the heat losses.

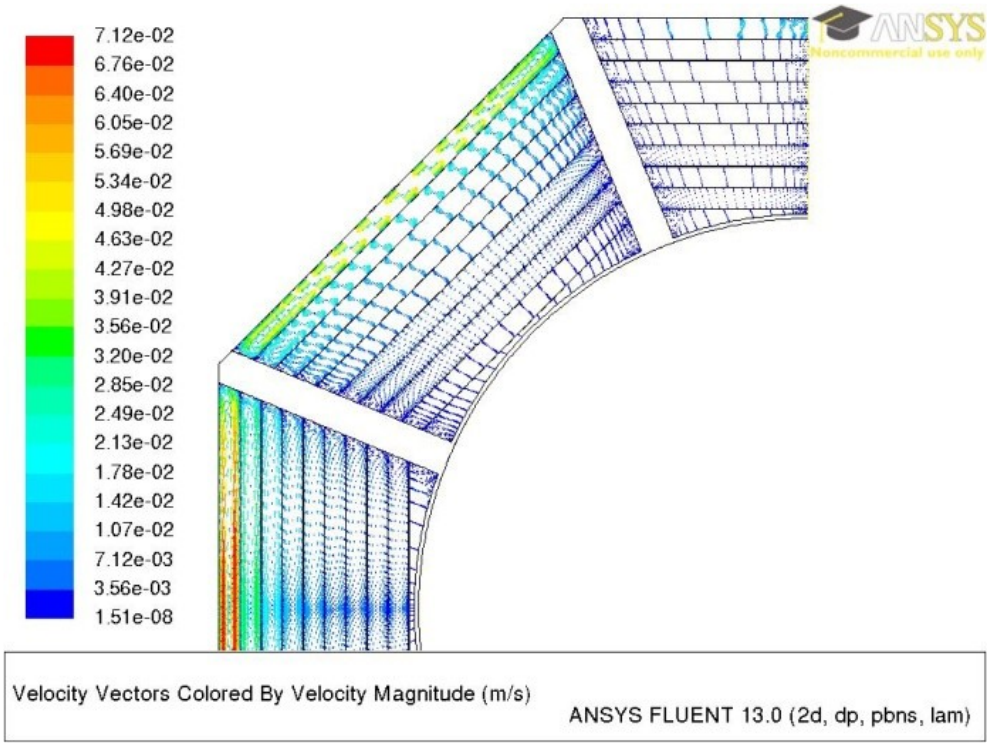

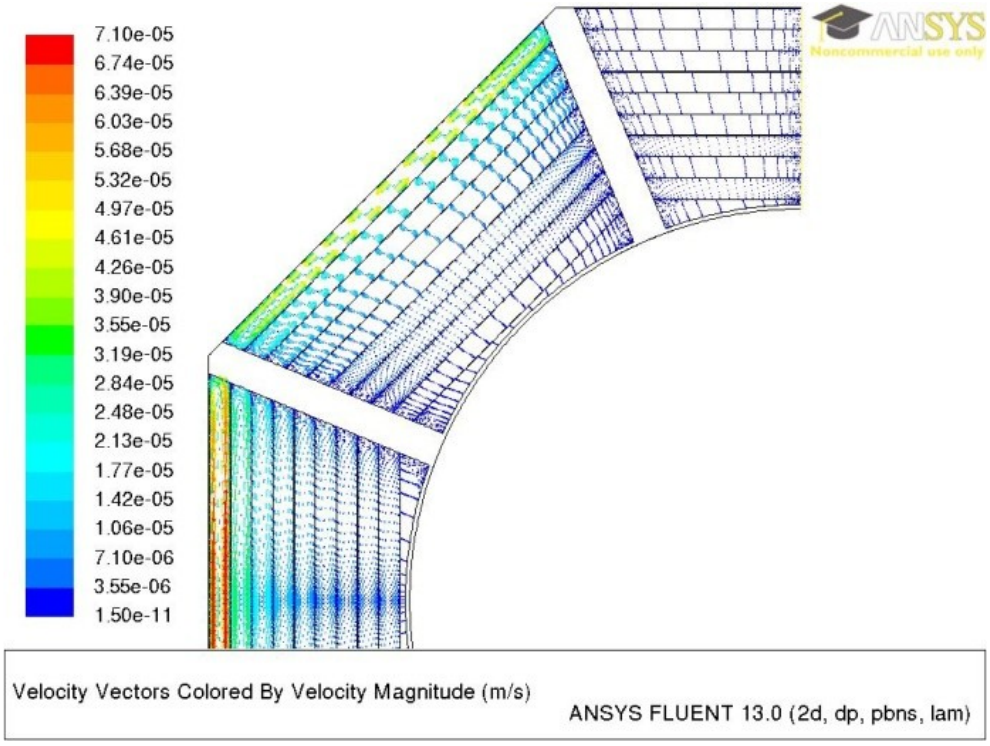

FIGURE 4: VELOCITY VECTORS COLORED BY VELOCITY MAGNITUDE FOR OPERATING PRESSURE OF 101’325 Pa (TOP) AND 100 Pa (BOTTOM)-SHIELDS DISTANCE: 12 mm.

Figure 5 and Figure 6 show the insulating performances in the cases with a shields distance of 50 mm. With this geometry a low pressure condition between the shields (bottom of the figures) is required to prevent the convective currents development. On the top of the figures, the shapes and the unfavourable effects of the convective cells are clearly represented.

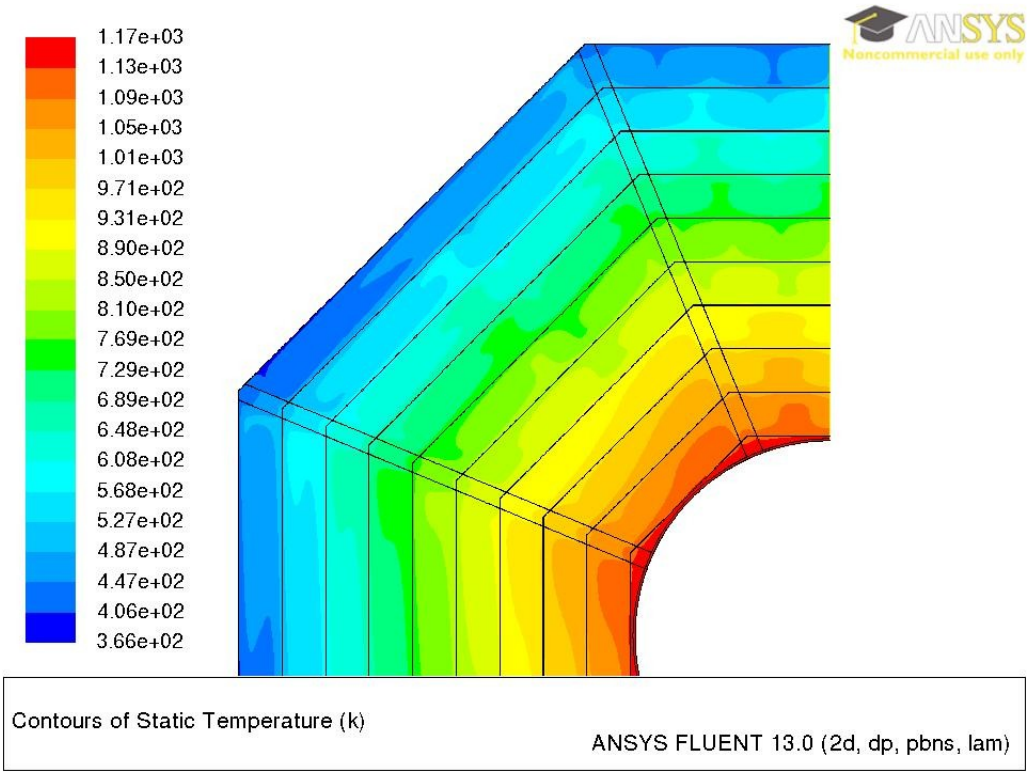

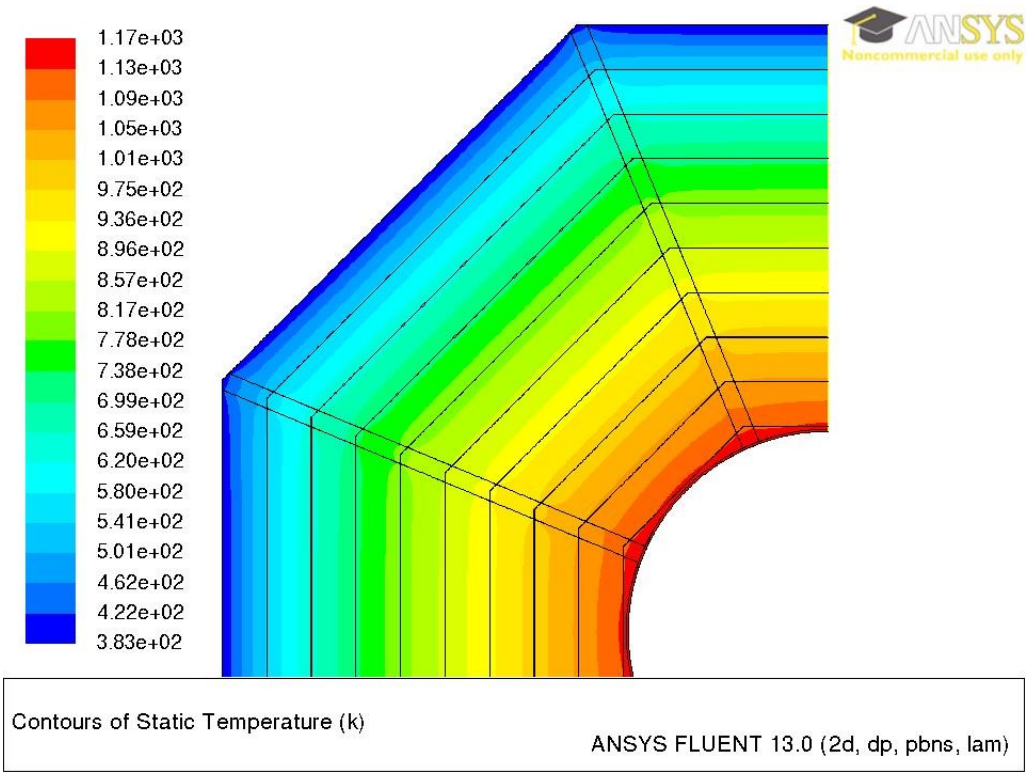

FIGURE 5: STATIC TEMPERATURE DISTRIBUTION FOR OPERATING PRESSURE OF 101'325 Pa (TOP) AND 100 Pa (BOTTOM) - SHIELDS DISTANCE: 50 mm.

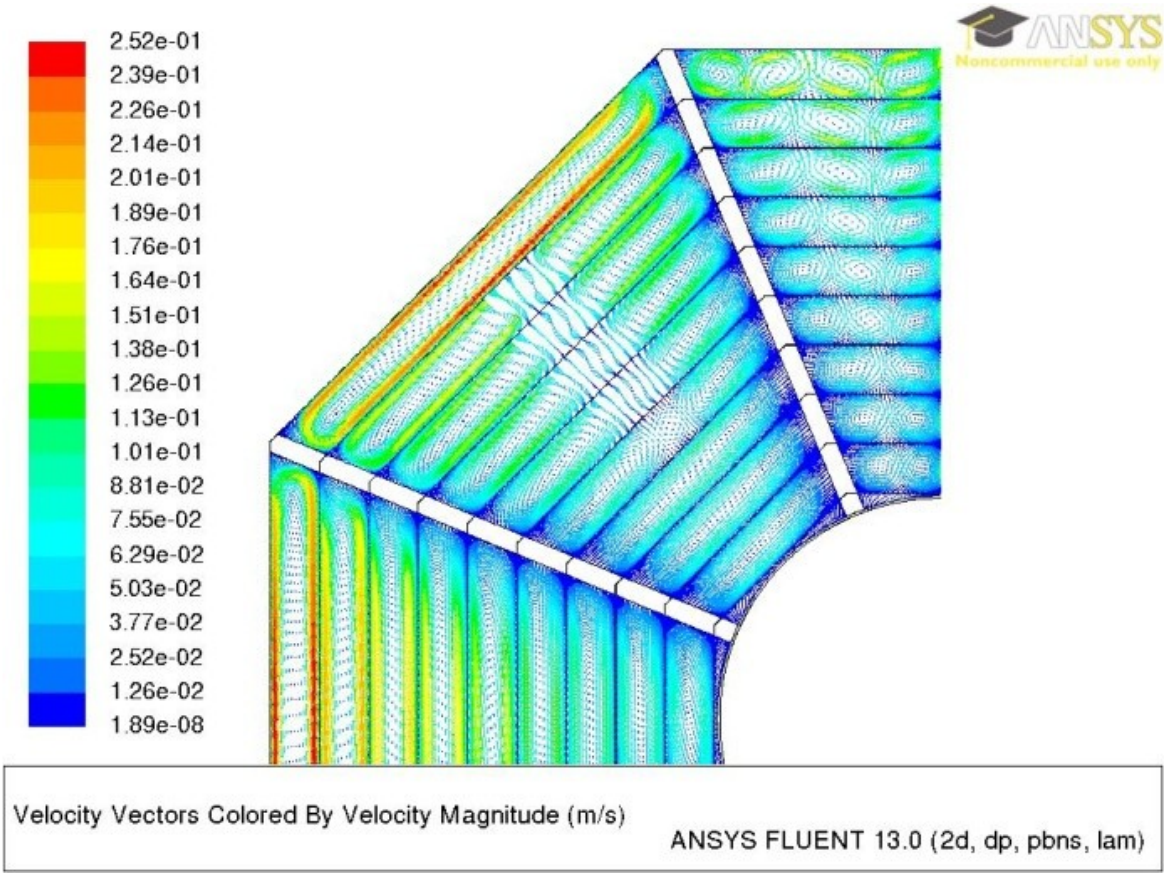

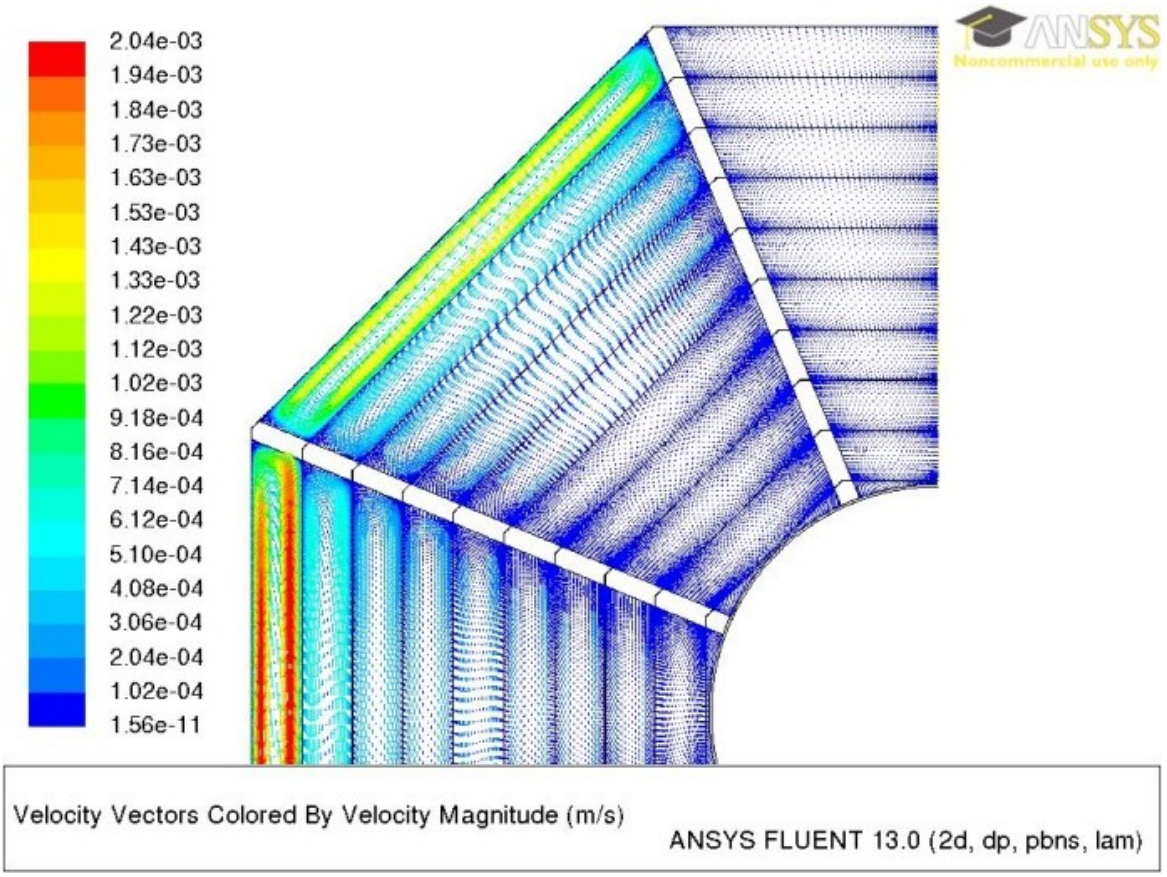

FIGURE 6: VELOCITY VECTORS COLORED BY VELOCITY MAGNITUDE FOR OPERATING PRESSURE OF 101'325 Pa (TOP) AND 100 Pa (BOTTOM) - SHIELDS DISTANCE: 50 mm.

Although Figure 7 shows that the receiver external temperature keeps decreasing increasing the distance between the shields, Figure 8 highlights there is an optimum value beyond which a shield distance increment will worsen the thermal insulation performances. This last aspect is related to the fact that the heat losses depend not only on the external wall temperature but also, and significantly, on the external wall surface extension. The equivalent thermal conductivity, as a function of the distance between shields, is reported in Figure 9.

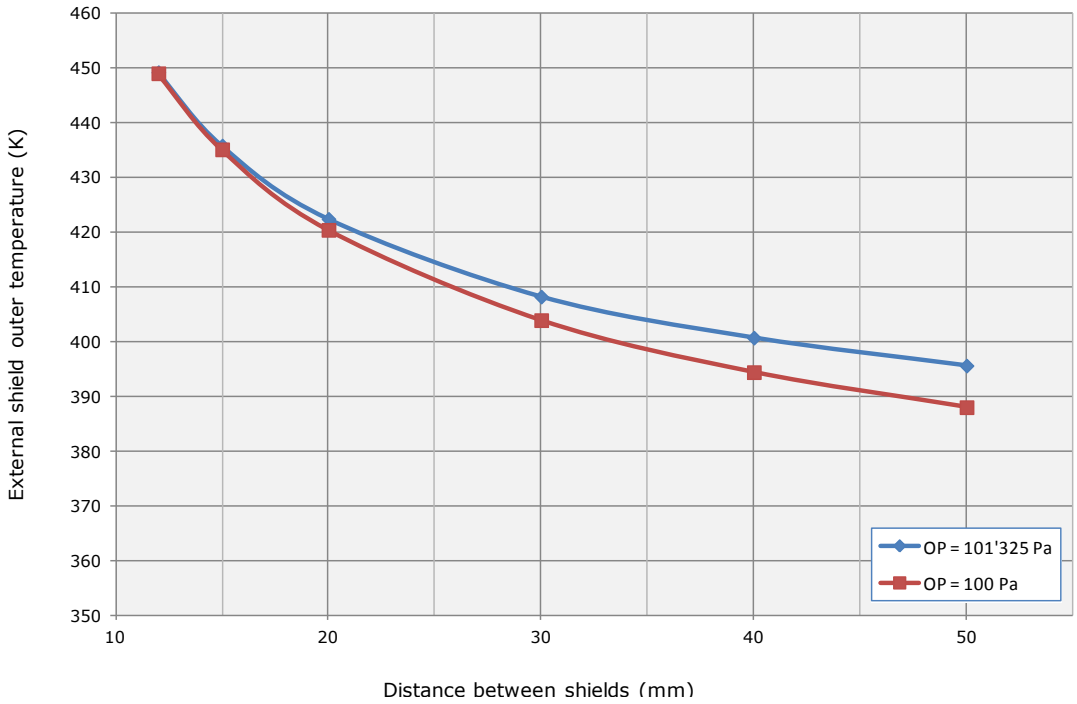

FIGURE 7: CASE 1 - OUTER WALL TEMPERATURE VERSUS DISTANCE BETWEEN SHIELDS GRAPH.

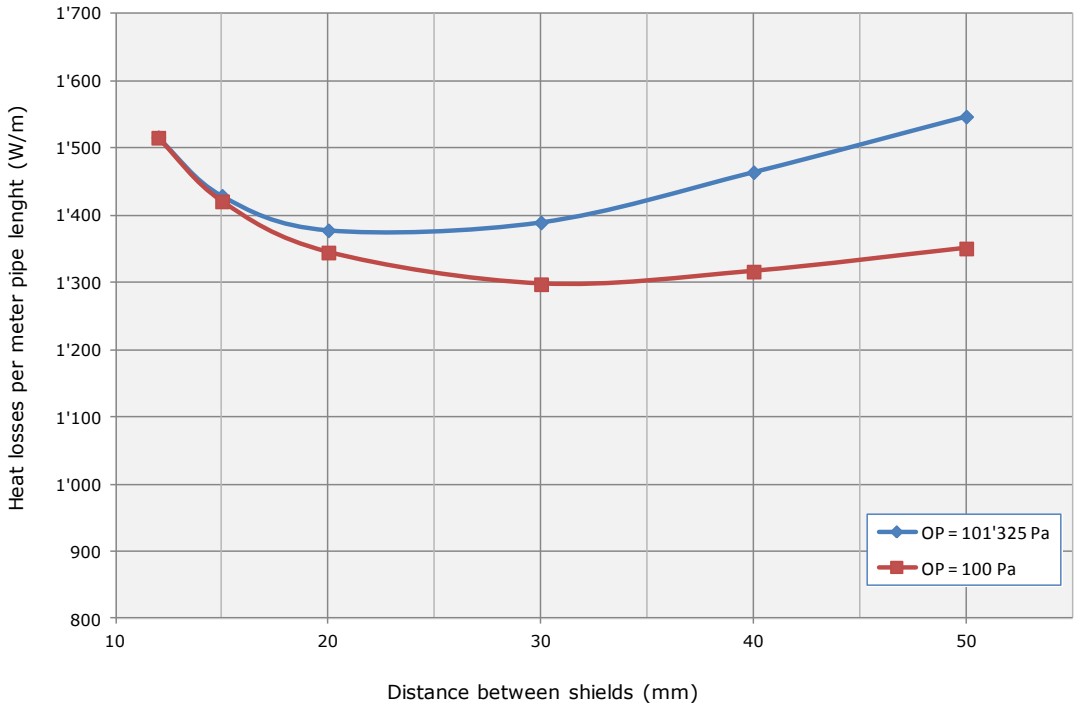

FIGURE 8: HEAT LOSSES VERSUS DISTANCE BETWEEN SHIELDS GRAPH.

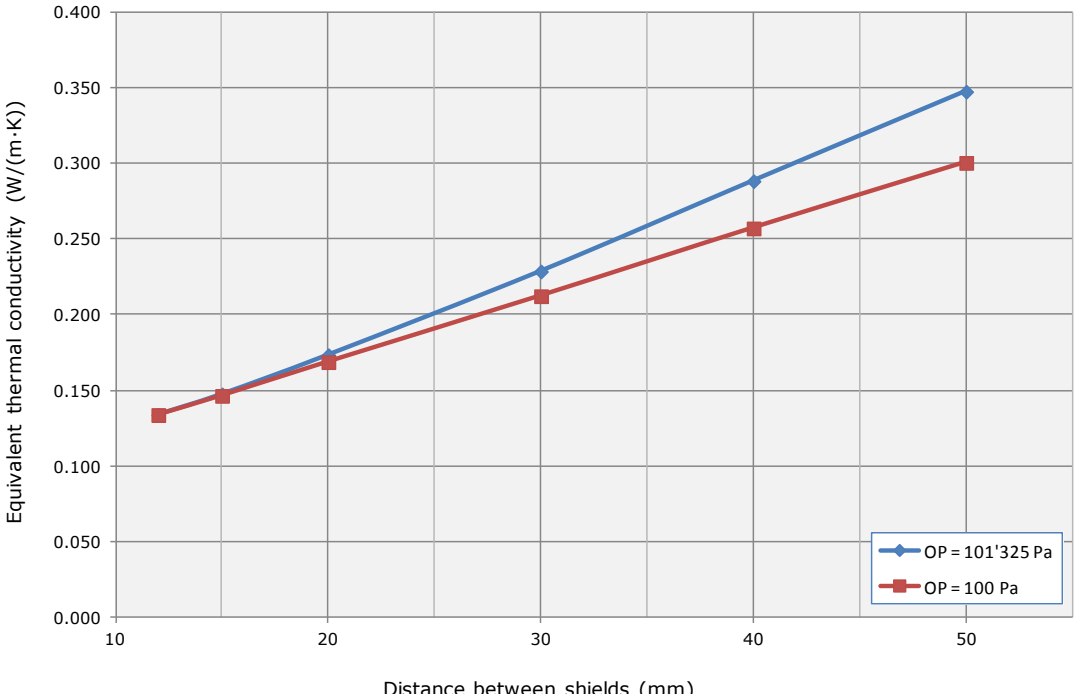

FIGURE 9: CASE 1 – EQUIVALENT THERMAL CONDUCTIVITY VERSUS DISTANCE BETWEEN SHIELDS GRAPH.

4.3.2. Case 2: Radiation shields quantity optimization

A second set of simulations was run to study the influence of the shields number. The external shield and the air duct dimensions were the same of Case 1 while the number of shields was varied from 8 to 12, 15 and 20.

As in Case 1 the simulations were run with two different operating pressure conditions, standard (101'325 Pa) and low (100 Pa). All the other dimensions were kept unchanged: spacer width is 20 mm and distance from the air duct and the first shield, at the closest point, is 3 mm.

Computational domain

The computational domain, reported in Figure 10, was defined applying the same assumption of Case 1.

Computational grid and modelling details

The model equation were the same of Case 1.

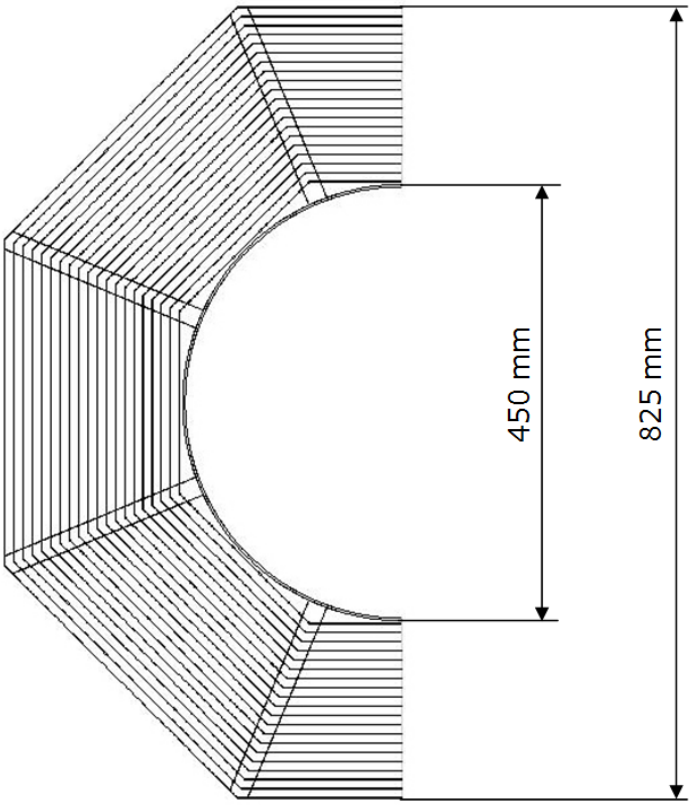

FIGURE 10: COMPUTATIONAL DOMAIN GEOMETRY AND MAIN DIMENSIONS – 20 SHIELDS.

CFD simulations results

Figure 11 shows temperature contours and Figure 12 shows velocity contours for the high pressure and low pressure cases of the 8 shields configuration. With this geometry a low pressure condition is required to prevent the convective currents development. The shape and the unfavourable effects of the convective cells are clearly observable in the high pressure case.

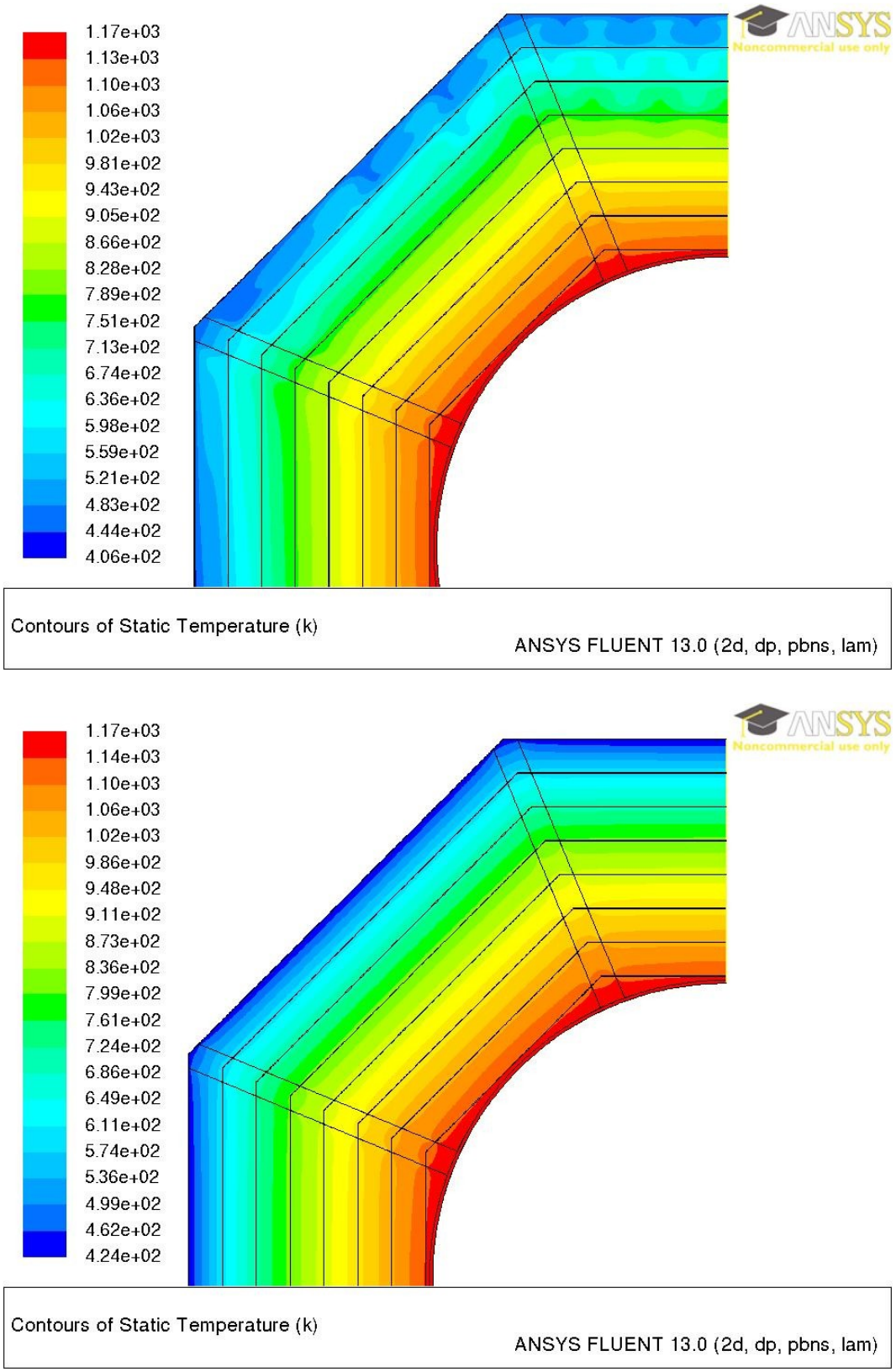

FIGURE 11: STATIC TEMPERATURE DISTRIBUTION FOR OPERATING PRESSURE OF 101'325 Pa (TOP) AND 100 Pa (BOTTOM) – NUMBER OF SHIELDS: 8.

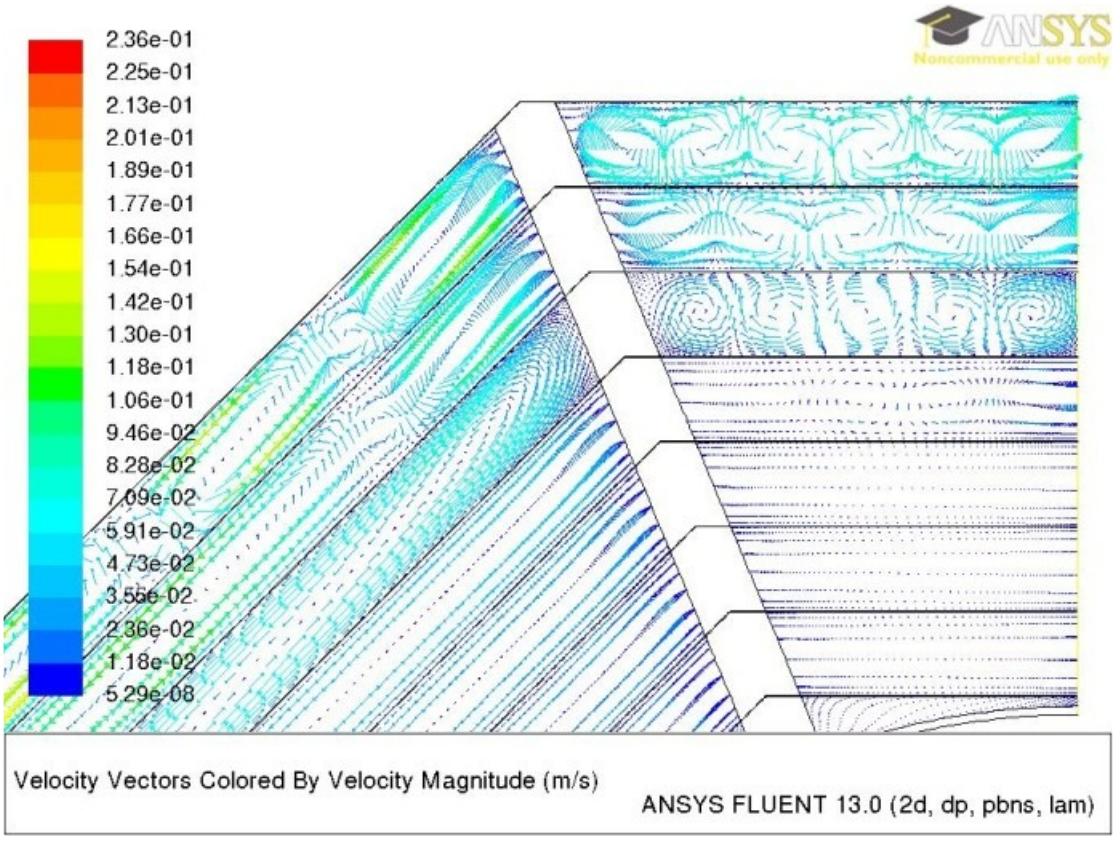

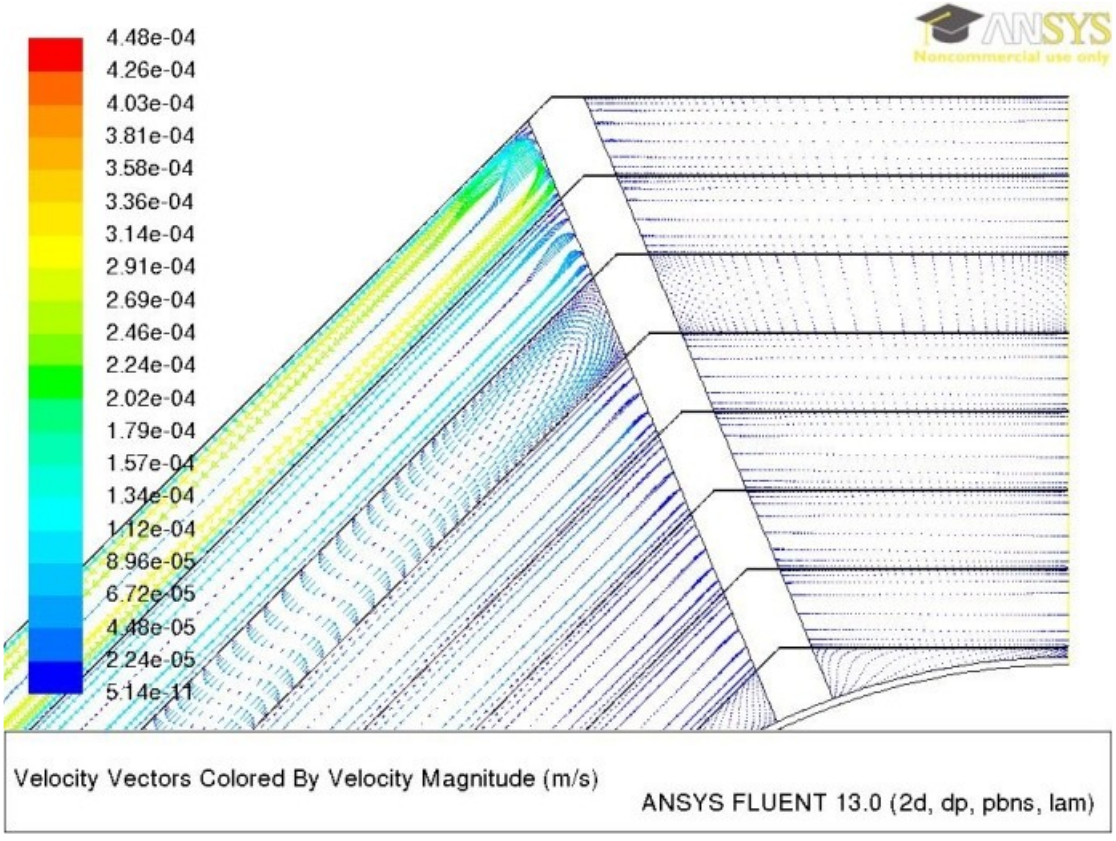

FIGURE 12: VELOCITY VECTORS COLORED BY VELOCITY MAGNITUDE FOR OPERATING PRESSURE OF 101'325 Pa (TOP) AND 100 Pa (BOTTOM). NUMBER OF SHIELDS: 8.

Figure 13 shows temperature contours for the 20 shields thermal insulation system. The low pressure condition in this case results to be not necessary. In fact, the temperature distributions are exactly the same for standard and low pressure condition.

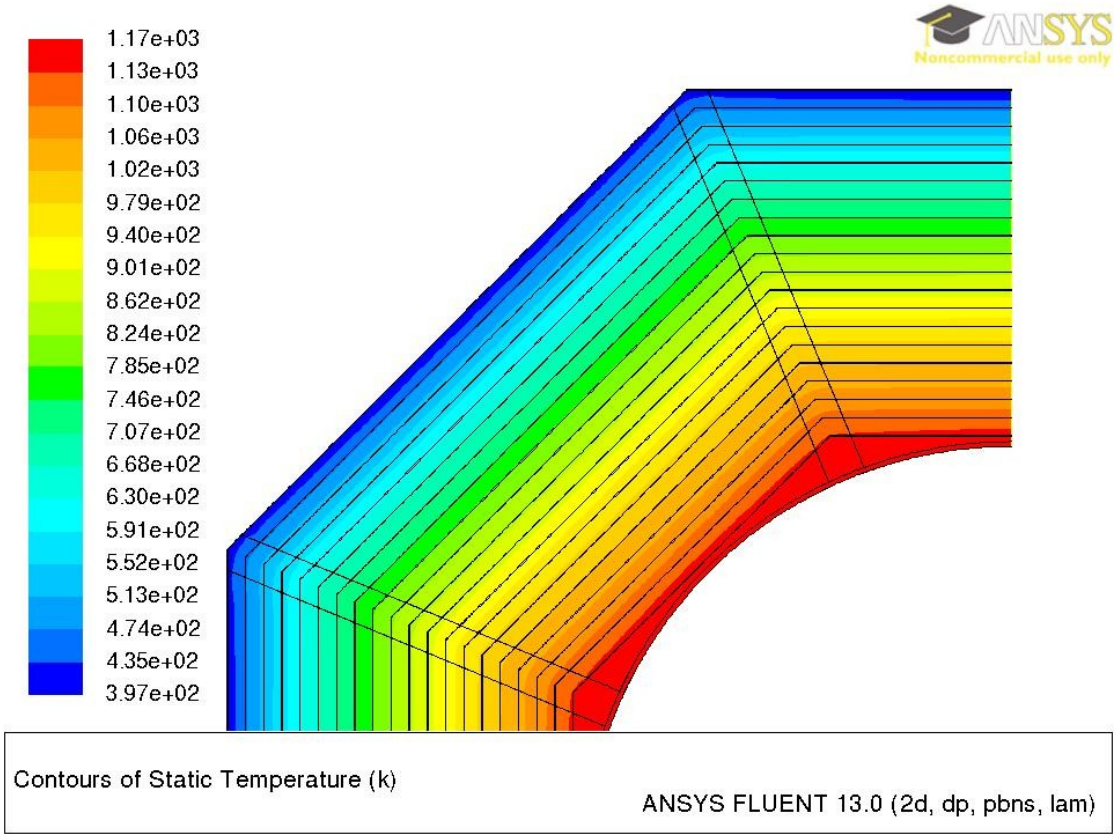

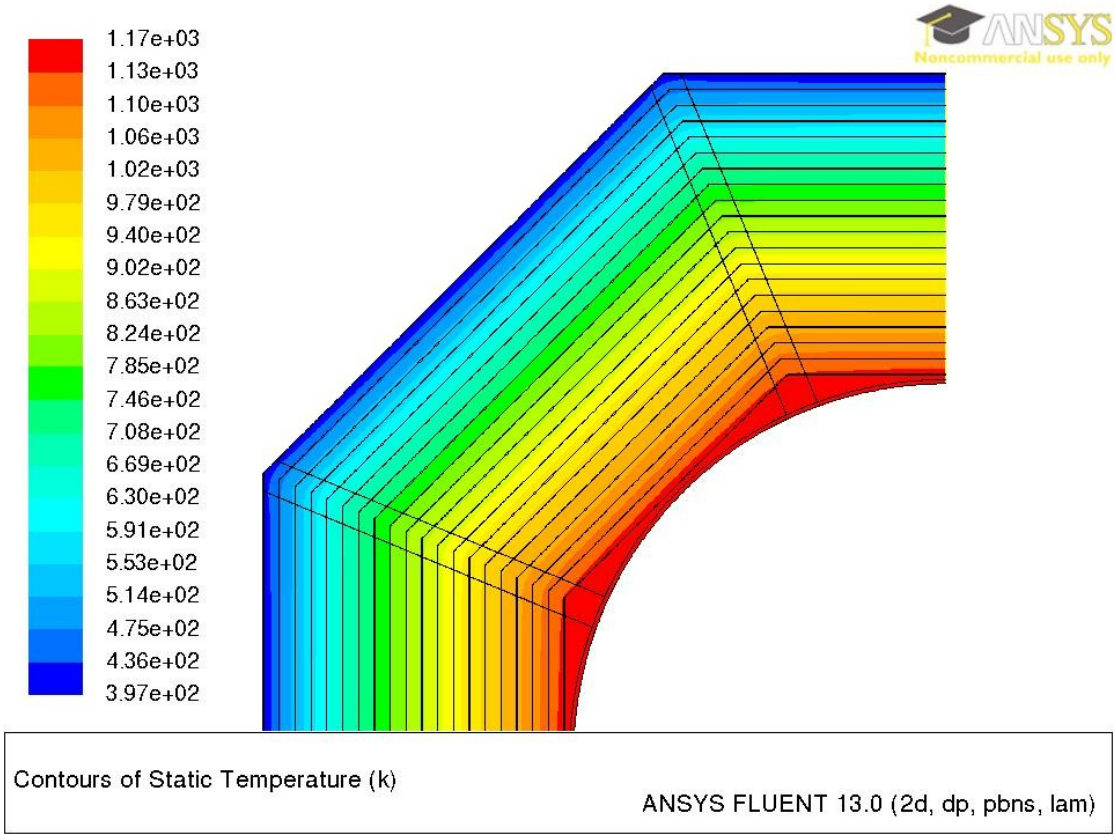

FIGURE 13: STATIC TEMPERATURE DISTRIBUTION FOR OPERATING PRESSURE OF 101'325 Pa (TOP) AND 100 Pa (BOTTOM) – NUMBER OF SHIELDS: 20.

Figure 14 and Figure 15 show that in Case 2 a reduction of the external shield outer wall temperature corresponds to a continuous reduction of the system heat losses. This is due to the fact that the receiver external diameter does not change.

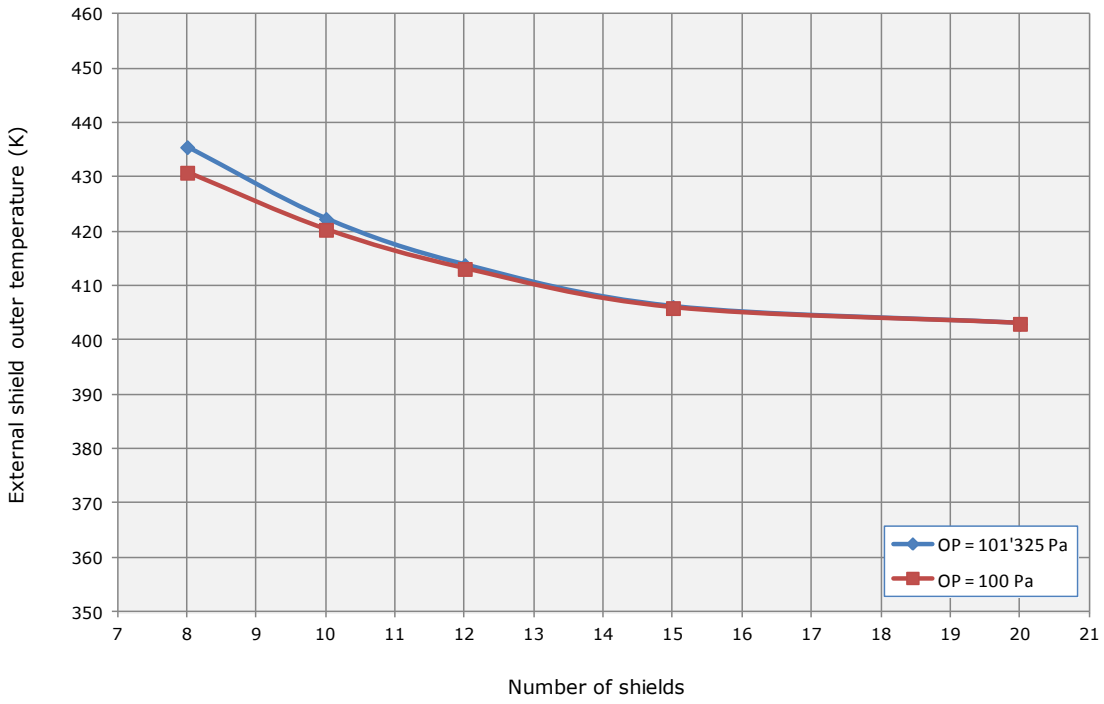

FIGURE 14: CASE 2 - OUTER WALL TEMPERATURE VERSUS NUMBER OF SHIELDS.

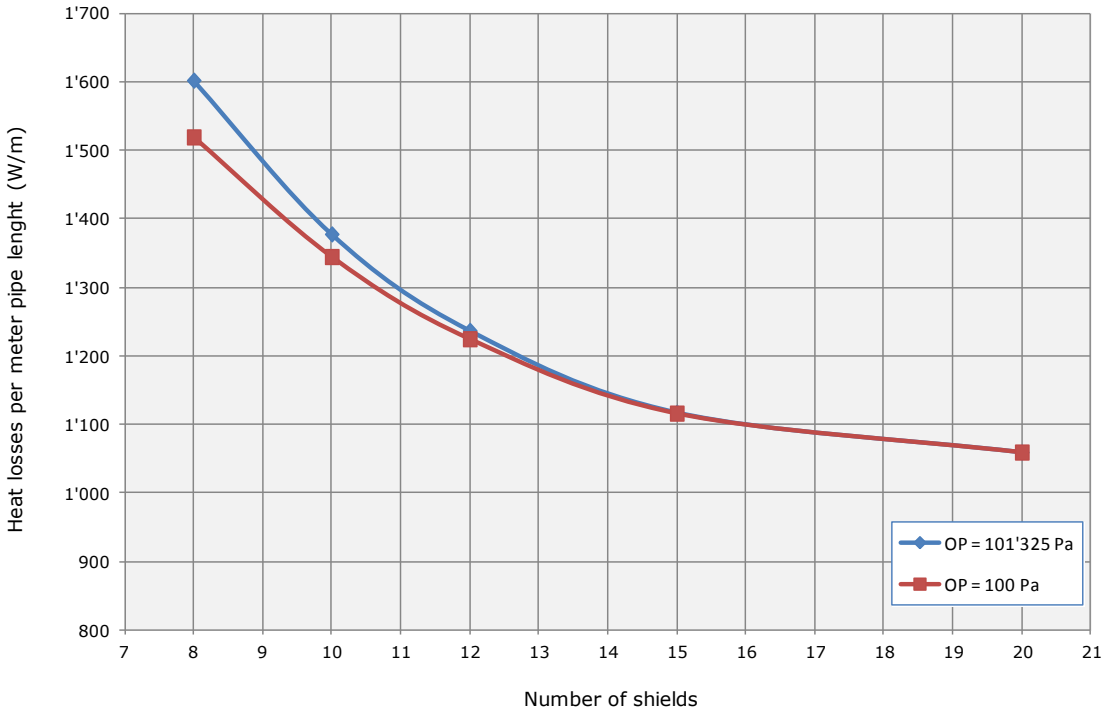

FIGURE 15: CASE 2 - HEAT LOSSES VERSUS NUMBER OF SHIELDS.

It is also possible to notice, looking at Figures 14-16, that the low pressure condition does not give any further advantage if the number of shields is greater than 12. This corresponds, as in Case 1, to a distance between shields lower than 15 millimetres.

Increasing the number of shields, the benefit in terms of heat losses tends to be asymptotic. Therefore, it will probably be not worth using more than 15-20 shields for the thermal insulation system.

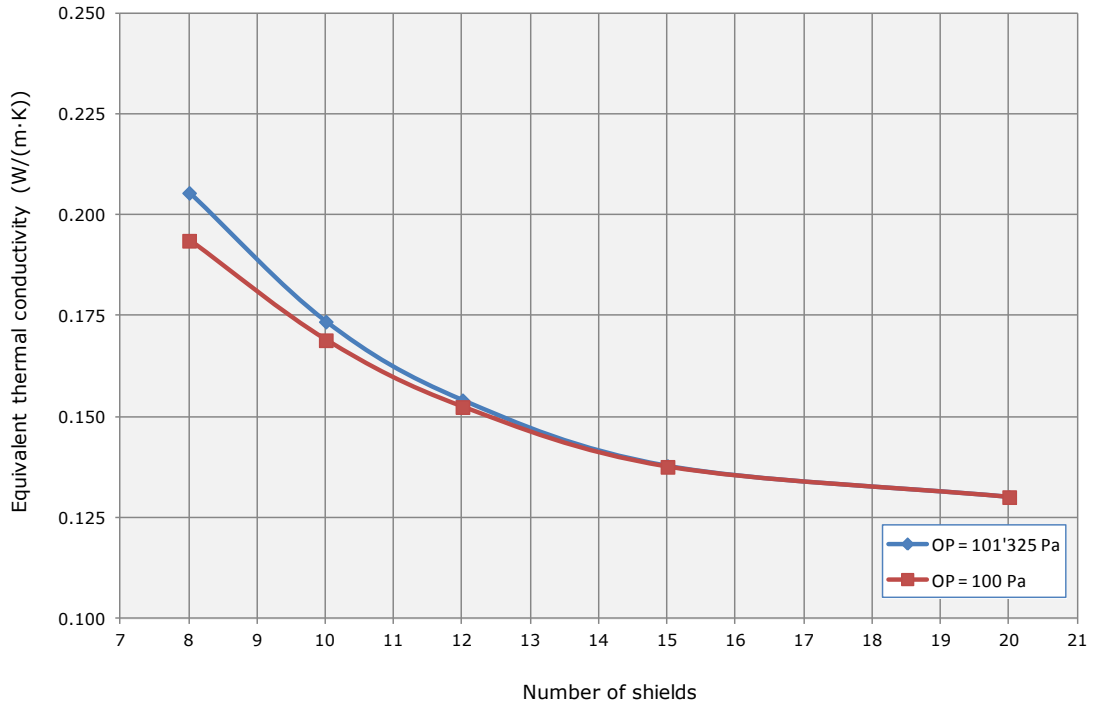

FIGURE 16: CASE 2 – EQUIVALENT THERMAL CONDUCTIVITY VERSUS NUMBER OF SHIELDS.

4.3.3. Case 3: External emissivity effect

Considering two hot cylinders located in the same surroundings, with the same external temperature but with a different outer emissivity, it is reasonable to expect that the component with the higher emissivity will lose by radiation a more important heat flux. Looking at the previous geometries if the external shield loses more energy, its temperature will decrease, but a lower temperature will essentially reduce, with the temperature to the fourth power, the radiation losses.

This fact makes more difficult to intuitively predict the overall behaviour of the system when changing its external emissivity.

In order to explore the external emissivity influence, the thermal insulation system made up with 10 shields placed at a distance of 12 mm was taken. The external emissivity was then increased from the value of 0.07 to 0.3 and 0.9.

Computational domain

The computational domain was the same used in Case 1 and Case 2.

Computational grid and modelling details

The meshes and the models were the same as in Case 1 and Case 2.

CFD simulations results

Figure 17 highlights that the higher the external emissivity the lower the receiver outer temperature. The larger temperature difference between the air duct internal wall and the external shield outer skin brings to a reduction of the theoretical equivalent thermal conductivity value of the insulating geometry. However, the analysis shows that, despite the outer wall temperature reduction, an enhancement of the external wall emissivity involves an augmentation of the receiver overall heat losses.

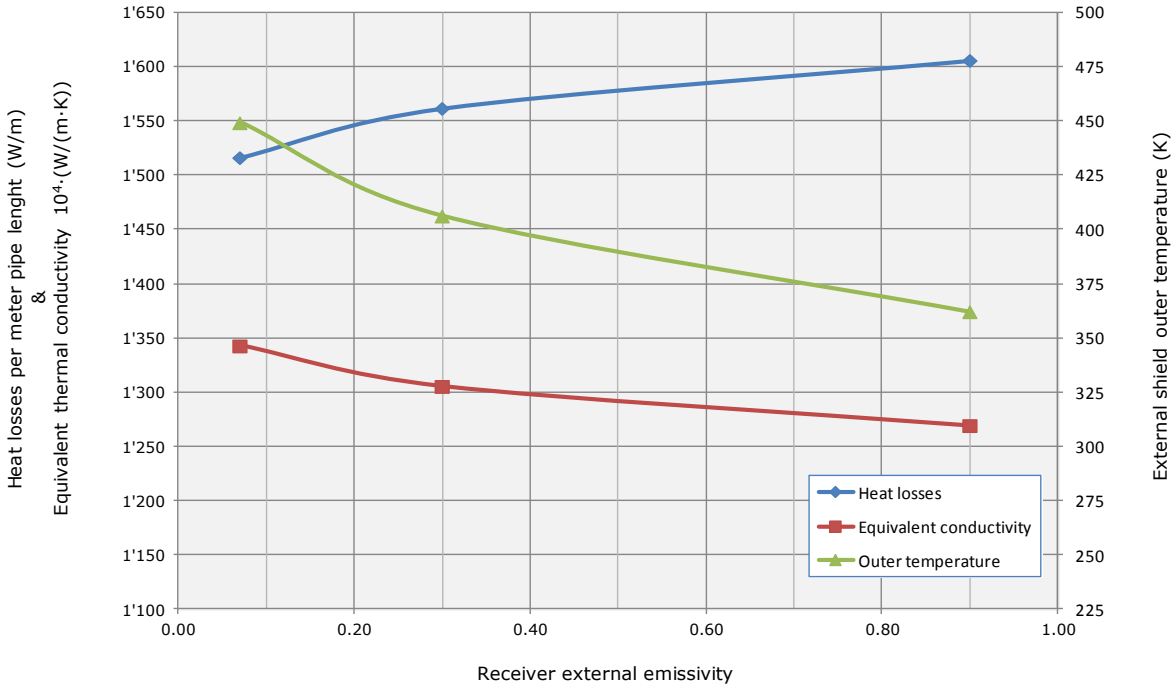

FIGURE 17: CASE 4 - EXTERNAL EMISSIVITY EFFECT HEAT LOSSES, EQUIVALENT CONDUCTIVITY AND OUTER TEMPERATURE.

4.3.4. Case 4: Spacer conductive influence

The heat losses by conduction along the spacers, is a phenomenon that cannot be avoided in the current design. In order to quantitatively evaluate this phenomenon, the spacer width was reduced from 20 to 5 mm and finally to 0 mm. For this study a design with 10 shields placed at a distance of 15 mm was taken as reference case.

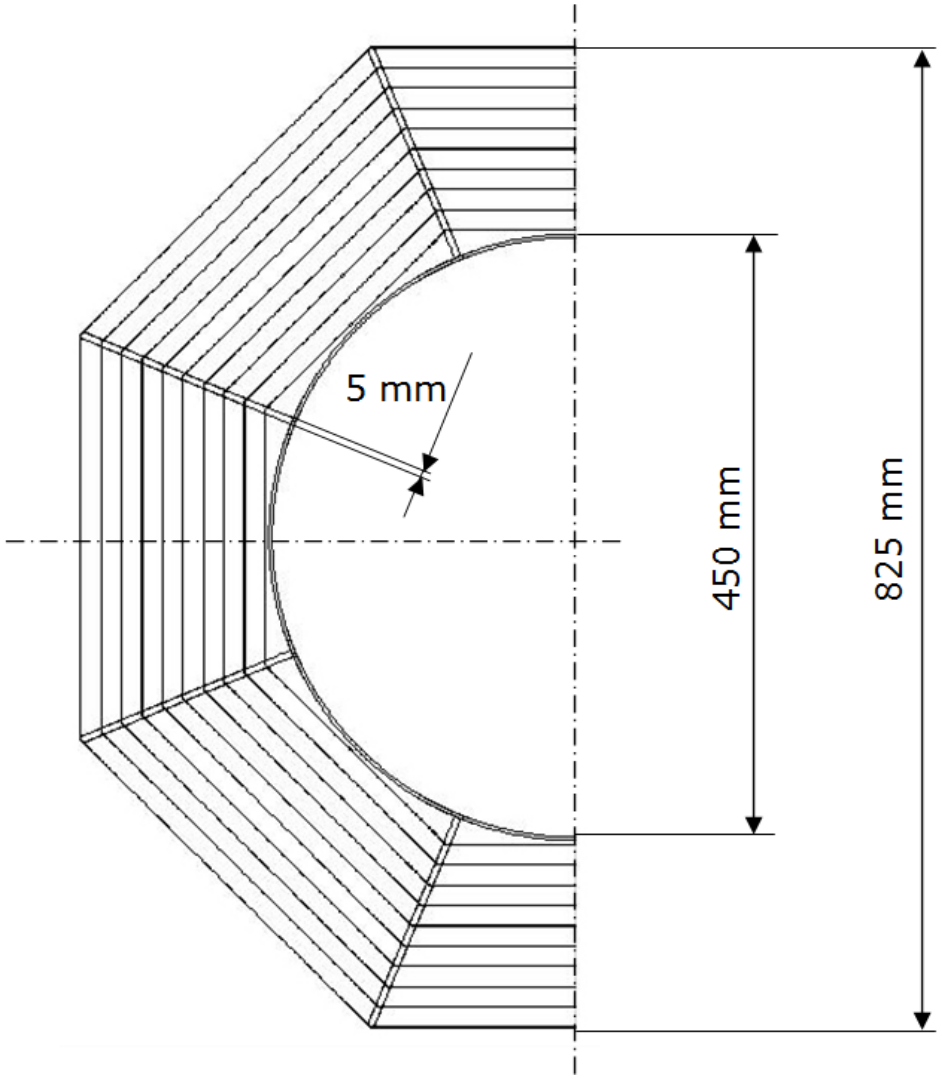

FIGURE 18: CASE 4 - SPACER CONDUCTIVE EFFECTS -THERMAL INSULATING SYSTEM MAIN DIMENSIONS.

Computational domain

The computational domain, apart from the spacer width, is the same used in *Case 1* and 2.

Meshes model and Boundary conditions

For the spacer conductive influence study, the meshes, the models and the boundary conditions, were the same of the ones used in Case 1 and Case 2. The only change, concerning the boundary condition, was introduced to simulate the 0 mm spacer width. Actually, in this case an adiabatic surface was set on the contact between the spacers and the shields. This change prevents thermal conduction phenomena between shields and spacers.

CFD simulations results

The analysis of the CFD simulations results obtained, in terms of heat losses, allowed to evaluate the conduction effects contribution. Actually, a reduction of the spacer width from 20 to 5 mm leads to a reduction in losses of 7% and an ideal spacer width of 0 mm would bring to a 19% reduction. Figure 19 shows the static temperature distribution in the case with conduction phenomena, whereas the case where conduction through spacers is inhibited is shown in Figure 20. In the latter figure a stepwise variation of temperature can be seen between adjacent spacers.

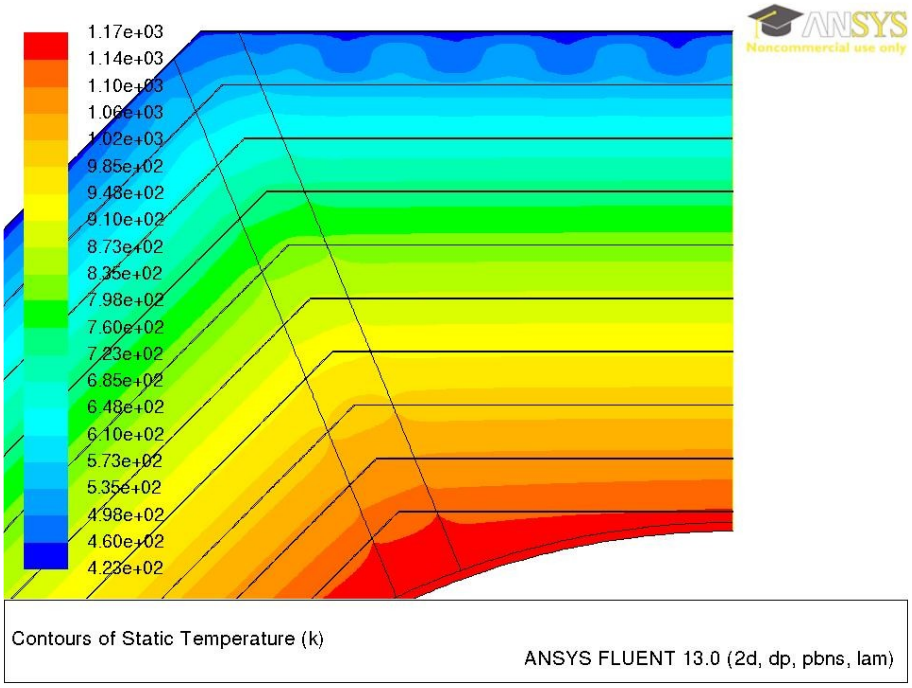

FIGURE 19: CASE 4 - STATIC TEMPERATURE DISTRIBUTION - SPACER WITH CONDUCTION PHENOMENA.

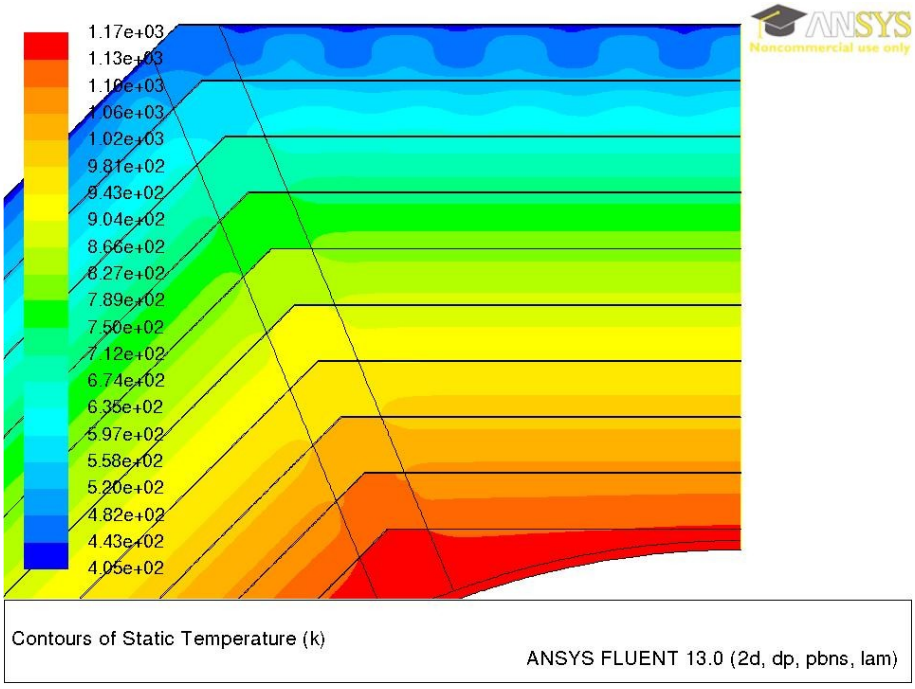

FIGURE 20: CASE 4 - STATIC TEMPERATURE DISTRIBUTION - SPACER WITHOUT CONDUCTION PHENOMENA.

4.4. Conclusions

In this chapter an analysis of a thermal insulation system based on radiation shields was performed.

The study was mainly focused on:

- shields separation distance evaluation;
- shields quantity optimization;
- conductive contribution of the spacers on the overall heat flux losses;
- external emissivity influence;
- low pressure condition effectiveness;
- spacer shape influence.

The assumption that the low pressure condition among shields could be unnecessary for some radiation shield geometries [1][4] was confirmed. The development of convective currents, which could increase the overall heat loss, can be avoided, for the geometries and temperatures analyzed in this work, considering distances between shields smaller than 15 mm.

In addition, the higher the shields number the best the thermal insulating efficacy. However, for the concerned temperature range a maximum number of 15 - 20 shields is suggested.

The receiver outer wall emissivity has to be kept as low as possible to minimize the overall heat losses.

The conductive heat transfer due to the shields spacers turn out to be relevant on the overall heat transfer. The result suggested to minimize the contact surface of the spacers as well as their quantity.

4.5. Publications

All the main results coming from the analysis of the multi-shields thermal insulation system were described into a scientific paper that was presented to the SolarPACES 2012 conference, in Marrakech, Morocco [5] and to the International CAE conference 2012, in Verona, Italy [6].

4.6. References

[1] SolAir 2 – Innovative solar collectors for efficient and cost-effective solar thermal power generation – 2 – SolAir-Pilot, BFE annual report 2011

[2] M. G. Carvalho, T. Farias, and P. Fontes. Predicting Radiative Heat Transfer in Absorbing, Emitting, and Scattering Media Using the Discrete Transfer Method. In W. A. Fiveland et al., editor, Fundamentals of Radiation Heat Transfer, volume 160, pages 17–26. ASME HTD, 1991.

[3] W. A. Fiveland and A. S. Jamaluddin. Three-Dimensional Spectral Radiative Heat Transfer Solutions by the Discrete Ordinates Method. HTD Vol. 106, Heat Transfer Phenomena in Radiation, Combustion and Fires, pp. 43–48, 1989.

[4] D. Montorfano, M. C. Barbato, “Receiver BRCPHC-7 - Thermal insulation analysis”, DTI-SUPSI, ICIMSI. Manno - CH : s.n., December 2011

[5] D. Montorfano, M. C. Barbato, A. Gaetano, A. Pedretti, F. Malnati, S. Pusterla. Thermal insulation based on radiation shields for CSP-HTF pipes: CFD modeling and experimental validation. SolarPACES 2012, Marrakech - Morocco .

[6] S. A. Zavattoni, D. Montorfano, A. Gaetano, G. M. Di Stefano, M. C. Barbato. CFD modeling suitable for concentrated solar power applications: thermal insulation based on radiation shields systems and thermal energy storage. International CAE conference 2012, Verona – Italia.

Chapter 5

Multi-shields insulation – Prototype testing

Contents

List of Figures

5.1. Introduction

To evaluate the thermal insulation behaviour of a prototype of multi-shields insulation system suitable for CSP piping, a test campaign was performed the 21st and 22nd December 2011 at the Airlight Energy Manufacturing SA site. This chapter illustrates the test set up, the test procedure and the results.

5.2. Test plan

5.2.1. Test list

A single test was foreseen because the system inspection after the test was destructive. The test aims at evaluating the capabilities of the new insulation system; moreover the test shall provide information about the capability of aluminium shields to withstand the high temperatures.

5.2.2. Temperatures stabilization criterion

For the test the temperatures selected and monitored shall reach the stabilization, this means that the time variation of the temperature values shall be less than 0.1°C/min.

5.3. Test model

The test aims at analyzing a system formed by a pipe, representing the internal tube of the CSP receiver, surrounded by the multi-shields insulation. The diameter of the internal tube is 200 mm and the length is 1 m. Figure 1 shows a sketch of the system while in Figure 2 the overall dimensions are given.

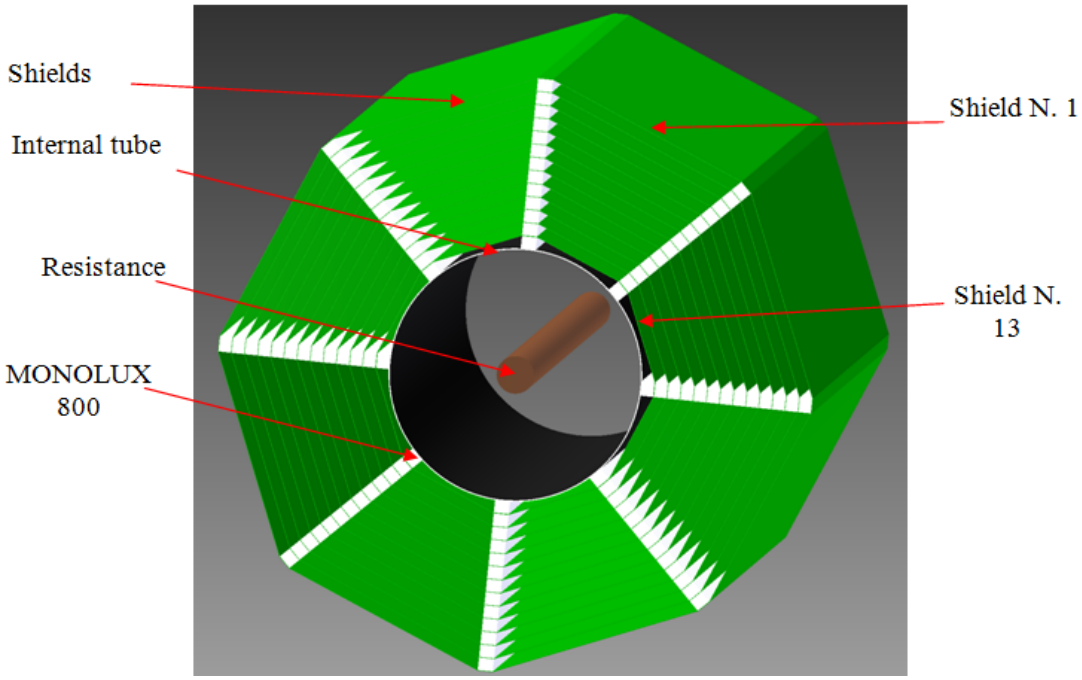

FIGURE 1: LAYOUT OF THE SYSTEM.

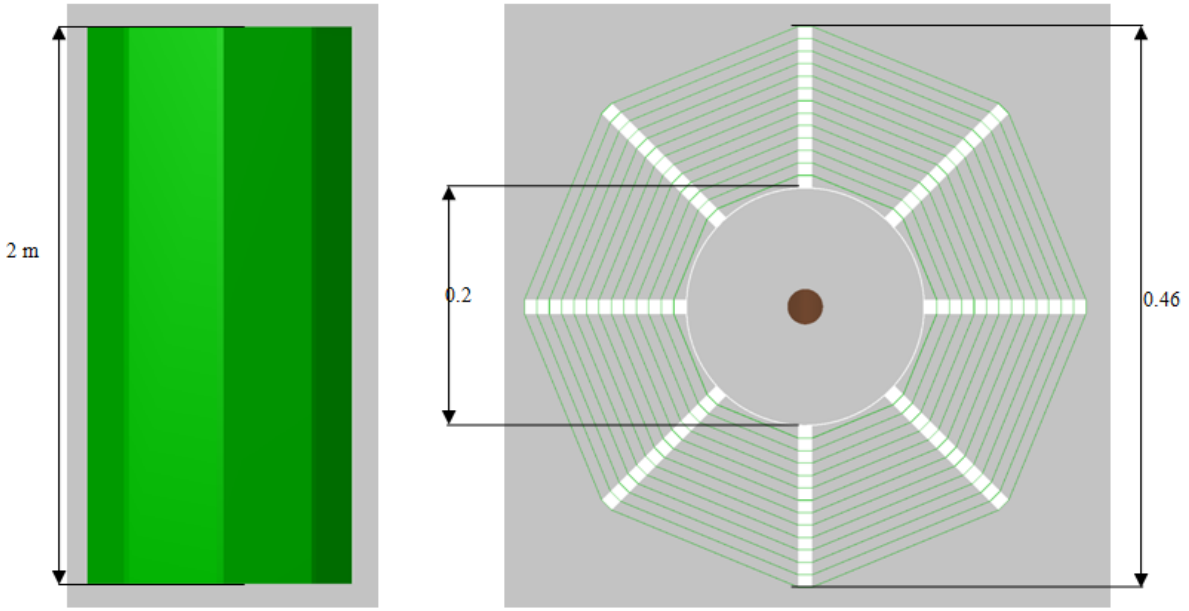

FIGURE 2: OVERALL DIMENSIONS OF THE SYSTEM.

The insulation is composed by 13 shields placed around the internal tube and separated by beams made of MONOLUX® 800. Figure 3 shows the system during the assembly phase at Airlight Energy laboratory. At the tips of tube two insulation panels are placed in order to maintain the hot air inside the tube and to avoid heat flux through them. During the test air is stagnating inside the tube, hence, no flow is allowed.

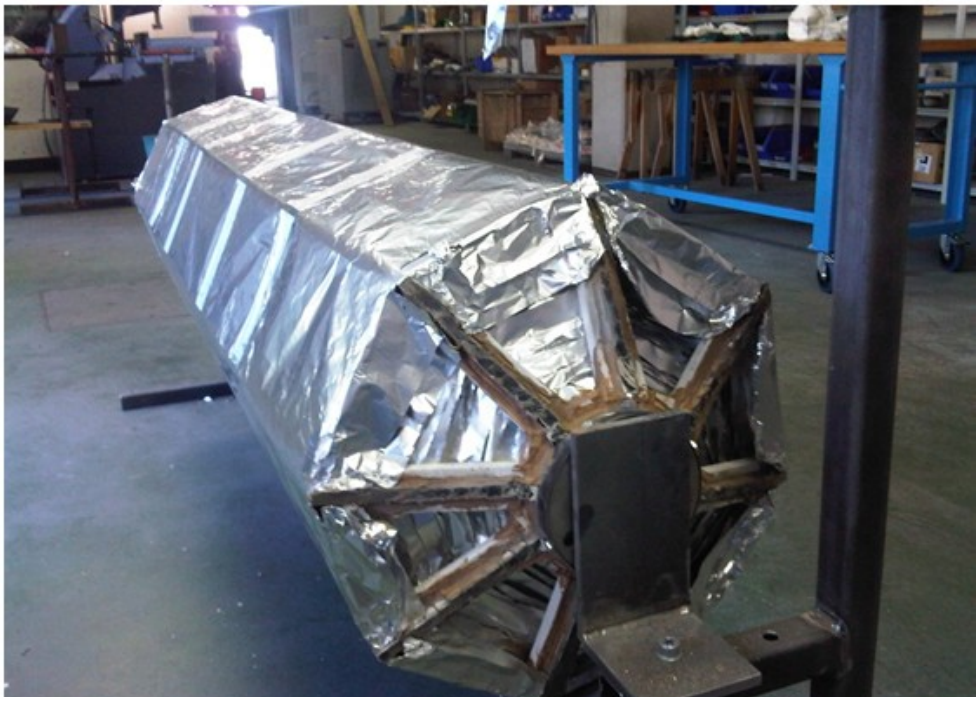

FIGURE 3: SYSTEM DURING ASSEMBLY PHASE AT AIRLIGHT LABORATORY.

5.4. Test sensors and acquisition systems

5.4.1. Thermal sensors

The thermal sensors are four thermocouples type K (Chromel – Alumel) with an operative range from –200°C to 1'200°C. The positions of the thermocouples on the system are described in Figure 4 and Figure 5.

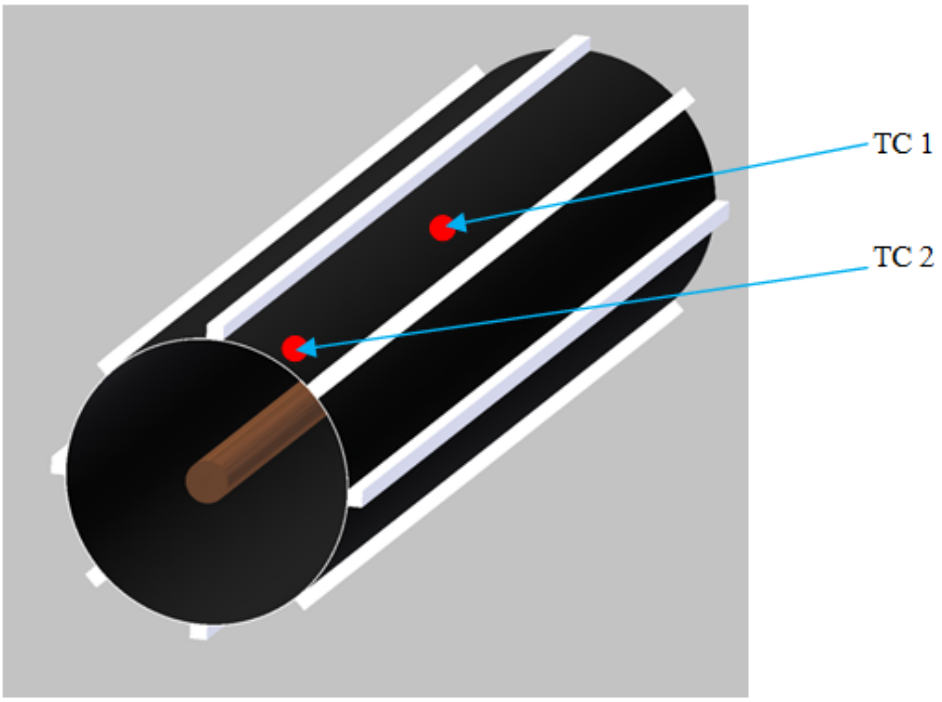

FIGURE 4: INTERNAL TUBE VIEW OF THE SYSTEM WITH THE POSITION OF THERMOCOUPLES.

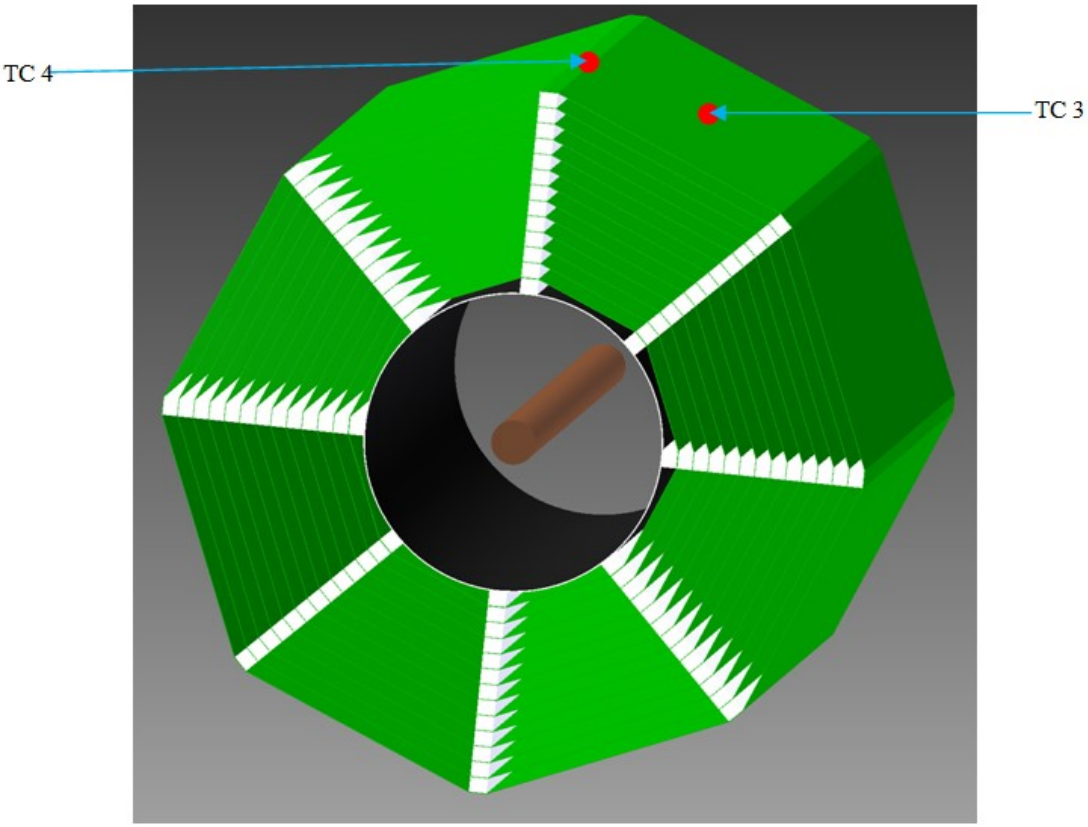

FIGURE 5: TEST ARTICLE VIEW WITH THE POSITION OF EXTERNAL THERMOCOUPLES.

5.4.2. Thermal data acquisition system

The thermal data acquisition system was able to show the temperatures with an accuracy of 1°C. Because the test aims at verifying the behaviour of the system in thermal equilibrium, the acquisition of temperatures could be done manually.

5.4.3. Power system

The power system was able to show the data about the electric power provided to the resistor. The electric power was provided by a relay which has a duty cycle of 2 seconds. As far as concerning the electrical feeding line, the voltage and current were monitored and the data were retrieved manually. The feeding line was an AC current line with frequency of 50 Hz.

5.5. Test description

After the initial setup, the test started with the supply of electric power to the resistor. The power was supplied gradually in order to avoid any damage to the system. The aim of test was to reach the temperature on TC 1 of 570°C and verify the stabilization criterion for, at least, 10 minutes. Figure 6 shows the temperatures of four thermocouples, the missing data are reconstructed. After the test, the shields were opened in order to perform a visual inspection. Figure 7 shows the shield N. 13, the closest to the internal tube. Even if the shield is made of aluminium, it could withstand the temperature reached with small mechanical degradation. The others shields didn't show any optical or mechanical degradation.

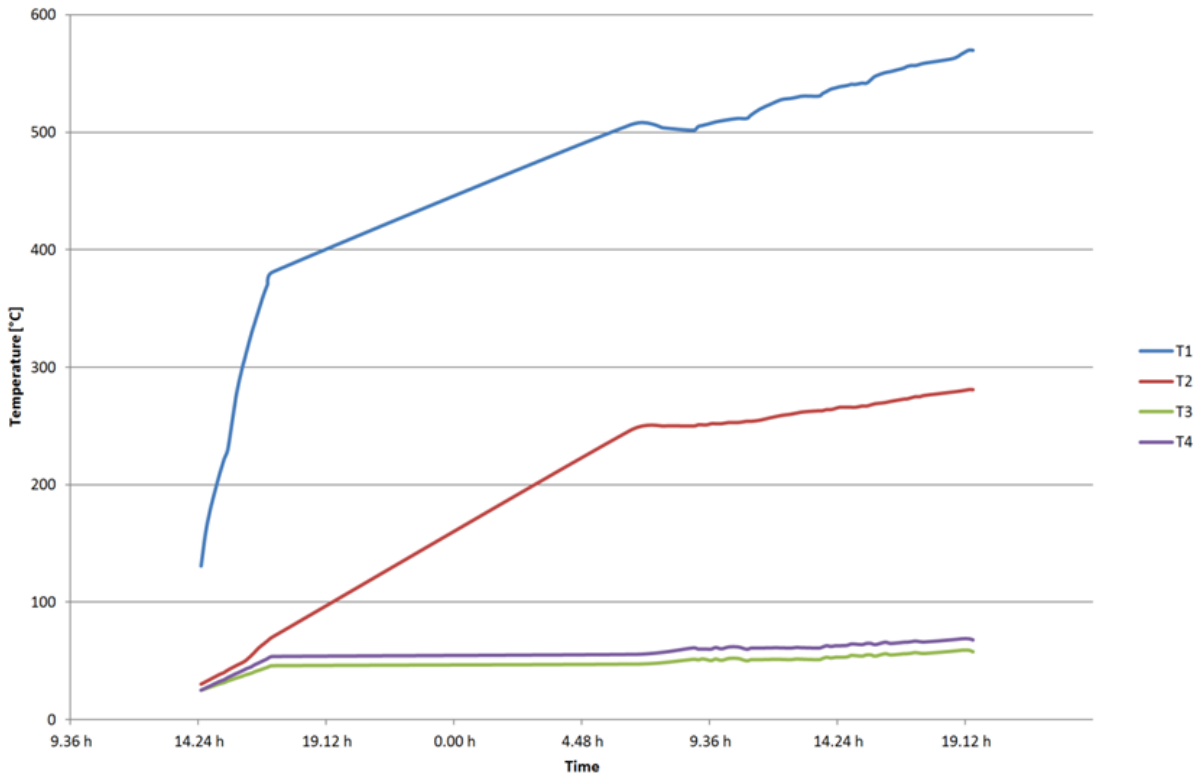

FIGURE 6: TEMPERATURE VALUES DURING THE TEST.

FIGURE 7: PICTURE ABOUT THE LAST SHIELD (N. 13) AFTER TEST.

5.6. Test data analysis

The test data were evaluated in order to verify the thermal conductivity along the radial direction. The value of the input power is 173.5 W obtained by the multiplication of current intensity by the voltage; the evaluation takes into account the duty cycle and the sinusoidal shape of the AC current. The formula to calculate the heat flux for a circular section is:

$$\dot{Q} = \frac{K \cdot 2 \cdot \pi \cdot L}{ln\left(\frac{R_2}{R_1}\right)} \cdot \Delta T$$

In the equation the parameters are: R_1 is the internal radius, R_2 is the radius, K is the effective thermal conductivity, L is the length of the tube and ΔT the difference of temperatures between the internal tube and the external shield. K can now be written as:

$$K = \frac{ln\left(\frac{R_2}{R_1}\right) \cdot \dot{Q}}{2 \cdot \pi \cdot L \cdot \Delta T}$$

5.7. Conclusions

Radiation shields experimental test main conclusions are:

- effective thermal conductivity value comparable to Microtherm®;
- heat capacity of the insulation lower than Microtherm® (conclusion obtained considering the energy absorbed by the system to reach steady state);
- faster transient at start up with respect to Microtherm®;

Because the temperature reached inside the tube (570°C) is less than the real receiver operative foreseen temperature (650°C) a problem should be expected if aluminium is used for the inner shields. In order to avoid the problem and to maintain a high level of reliability, a hybrid insulation system will be evaluated with a mix of multi-shields, in the external part of insulation and Microtherm® in the hottest inner part. Further tests and analysis are foreseen to estimate a good compromise between both systems and to harmonize the multi-shields system with the other components of the collector.

THIS PAGE INTENTIONALLY LEFT BLANK

Chapter 6

Receiver thermal insulation – CFD analysis

Contents

List of Figures

List of Tables

6.1. Introduction

This chapter gives an overview of the results achieved, by means of 2D steady-state CFD simulations performed at SUPSI, related to the thermal insulation of the new cavity receiver.

6.2. Receiver thermal insulation

Thermal insulation of the receiver is an important issue that has to be properly tackled in order to reduce as much as possible thermal losses towards the external environment. The use of air as HTF offers various advantages; however, air receivers need a larger heat transfer area and flow cross-section to overcome the poor thermal properties of air in comparison with the commonly used HTFs. For this reason, a larger volume of insulating material is required.

Thanks to both the experimental proof of concept, aforementioned in paragraph 5, and the foreseen advantages in terms of heat capacity, thermal shields were selected as main thermal insulation system. Figure 1 depicts a schematic representation of the receiver section with all the insulating materials involved.

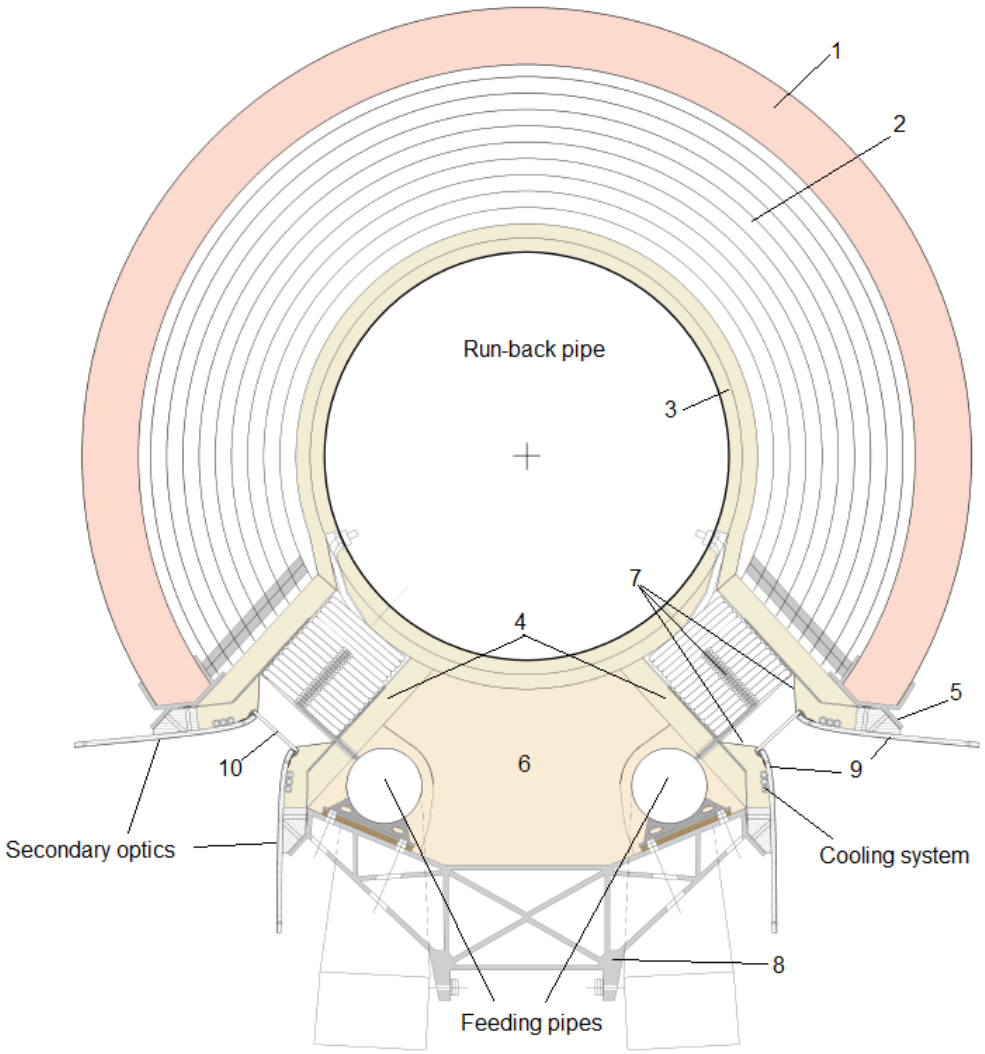

FIGURE 1: SCHEMATIC OF THE RECEIVER THERMAL INSULATION.

In this figure two distinct feeding pipes can be seen; “hot” air from all the cavities is then collected into a run-back pipe. Secondary optics is exploited to drive the incoming solar radiation into the chrysalis receiver. The external surfaces of this high-efficiency optics are coated with a thin aluminium film maximising the reflectivity behaviour. In order to maintain the favourable optics characteristics, the coating cannot withstand temperatures higher than 120°C; therefore, a water-based cooling system is provided to maintain the aluminium structure, of the secondary optics, into a safety temperature range. Two main heat fluxes have to be removed by the secondary optics cooling circuit: the heat flux from the cavities receivers and the fraction of incoming radiation absorbed by the material itself.

Table 1 provides a description of the materials, numbered into Figure 1, selected for the receiver. The data listed above are those implemented into the CFD simulations.

TABLE 1: LIST OF MATERIALS CONSTITUTING THE RECEIVER.

No.	Material	Density [kg/m^3]	Specific heat [J/(kg·K)]	Thermal conductivity [W/(m·K)]
1	Polyurethane foam	140	840	0.045
2	Aluminium thermal shields	2’719	871	202.4
3	Microtherm® OP	250	Piece-wise linear function [1]	Piece-wise linear function [1]
4	Microtherm® SG	320	Piece-wise linear function [1]	Piece-wise linear function [1]
5, 8	Aluminium	2’719	871	202.4
6	Rockwool	120	840	0.045
7	Stainless steel	8’030	502.5	16.27
9	Aluminium coating	2’719	871	202.4
10	Glass	2’200	Piece-wise linear function [2]	Piece-wise linear function [2]

6.3. CFD modelling and simulations

The thermal insulation effectiveness was studied by means of 2D steady-state CFD simulations supposing the larger heat transfer contribution occurring in the radial direction of the receiver cross-section and only a small fraction in the longitudinal.

The computation domain was built exploiting the symmetric characteristic of the receiver; hence, only half of the cross section was discretized with a grid of almost 310'000 quadrilateral cells. The internal heat transfer mechanisms, accounted for by the CFD simulation, are: conduction and radiation (the latter modeled via DO model). Due to the geometric limitations of this simplified model, convective heat transfer was not considered. This assumption is justified by the fact that convective heat transfer is negligible into both the internal part of the cavity and into the thermal shields because, as reported in [3], the distance between shields was kept small enough to prevent the onset of intense convective motions.

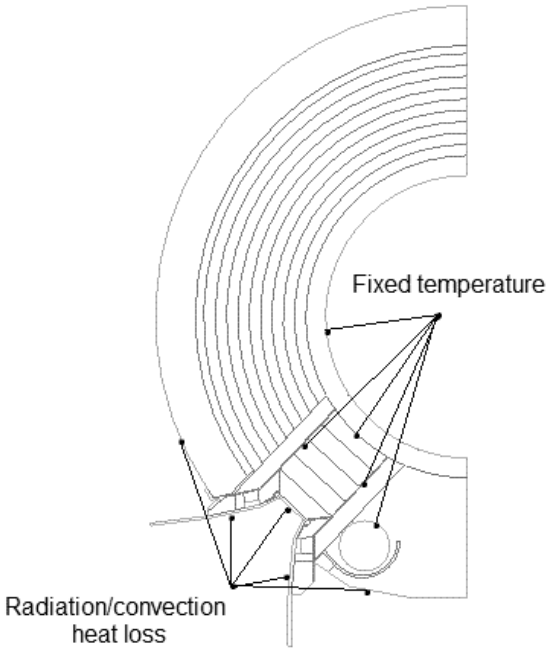

FIGURE 2: COMPUTATIONAL DOMAIN.

The boundary conditions applied to the model, as well as the modelling approximations assumed, are reported hereafter.

- A fixed temperature boundary condition was assigned to the external walls of the cavity. The latter were divided into four smaller segments describing in a more realistic way the effect of temperature variation into the cavity. The temperature value for the relative cavity segments was gathered from the results of the 3D CFD simulations previously reported in chapter 2.
- Constant fixed temperature conditions were assigned to the run-back and to the feeding pipes: 923.15 K and 393.15 K respectively.
- The cooling circuit was modeled as an equivalent convective heat-sink wherein the free-stream temperature and the convective heat transfer coefficient (HTC) were properly set.
- Due to the small thickness in comparison to the overall length, thermal shields were modeled as no-thickness foils.
- Heat losses towards the external environment, by means of both convection and radiation, were accounted for.

With the aforementioned assumptions, a first preliminary CFD simulation was performed. Figure 3 shows the results in terms of temperature distribution.

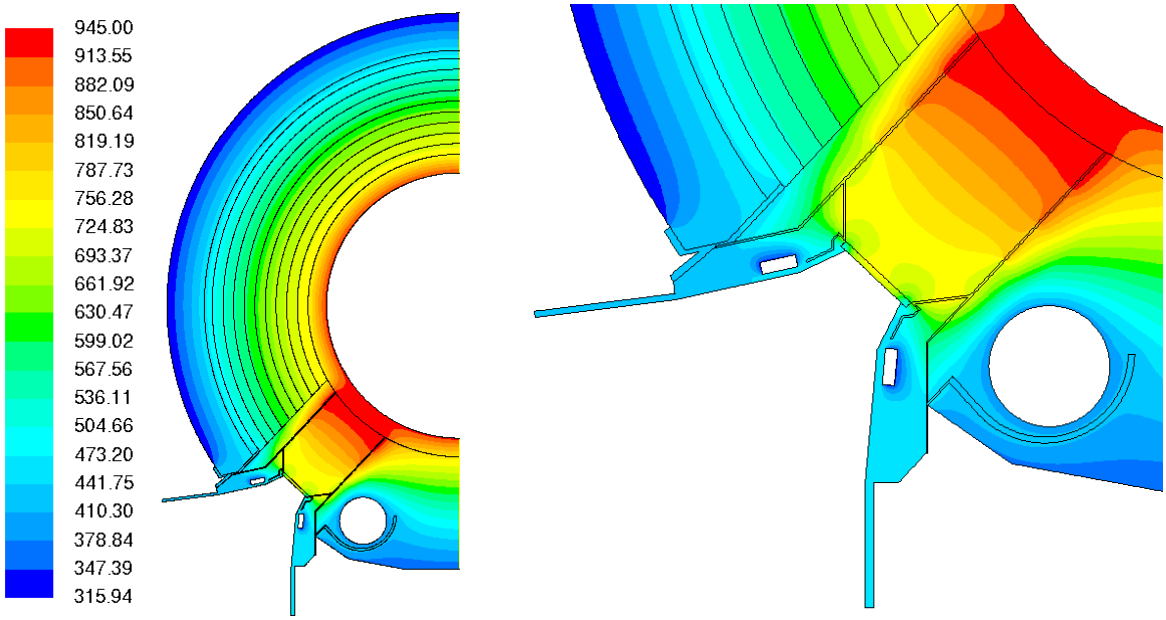

FIGURE 3: TEMPERATURE DISTRIBUTION OF THE RECEIVER CROSS SECTION. TEMPERATURE VALUES ARE IN K.

According to the CFD simulation results obtained, 53.8% of the overall heat losses is the power removed by the water cooling circuit; the remaining 46.2% is given by the heat losses towards external environment. However, it is worth to note that, beyond the power removed by the cooling circuit, the other major fraction of heat losses is due to the radiative/convective heat transfer from the external glass surface of the cavities.

As far as concerning the thermal shields, all of them are below the threshold temperature value, given by the limit of the material, of 820 K. The highest temperature, of about 730.2 K, is observable in correspondence of the first, and most internal, shield.

Secondary optics shows an average temperature of about 480 K, well above the fixed limit. The reasons are manifold: (1) thermal contact between glass external surface and secondary optics structure; (2) the presence of thin steel plates which, due to the relatively high steel thermal conductivity, establish a favourable way for heat transfer from the hottest internal regions towards the colder external surfaces; (3) the presence of other thin steel plates in direct thermal contact with the secondary optics and the internal region of the cavity.

The same geometry was analyzed afterwards considering the contribution of a 1'000 W/m^2 direct solar radiation onto the upper receiver surface faces directly the sun. The solar contribution was implemented into the solver by means of a purpose-built user defined function. Temperature distribution result is reported in Figure 4. The only appreciable difference with respect to the previous case is a temperature increment, of about 30 K, of the external surface directly irradiated by the sun. Despite the higher surface temperature, the net heat flux out of the surface is lower than the previous case due to the incoming solar power contribution. The heat flux from all the remaining surfaces is almost unchanged.

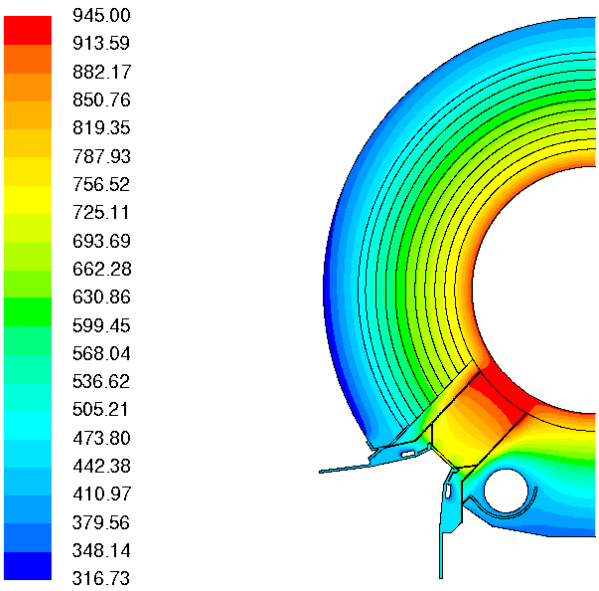

FIGURE 4: TEMPERATURE DISTRIBUTION OF THE RECEIVER CROSS SECTION WITH SOLAR CONTRIBUTION. TEMPERATURE VALUES ARE IN K.

Further simulations allowed to confirm the possibility of reducing both the overall heat losses and the secondary optics temperature acting mainly upon:

- the separation of the thermal contact between secondary optics and external glass surface;
- the removal of the steel plates which directly link the secondary optics and the internal region of the cavity.

The combination of these modifications allowed to reduce the overall heat losses with respect to the previous case (87.7% heat losses towards external environment and 12.3% power removed by the cooling cycle). The average temperature of the secondary optics was also reduced down to 357 K.

Figure 5 shows the temperature distribution for this last case. It has therefore to be intended as ideal case because the thermal contact between glass external surface and secondary optics was replaced with an adiabatic condition and the steel plates, linking internal cavity with secondary optics, were replaced with the same neighbour insulating material.

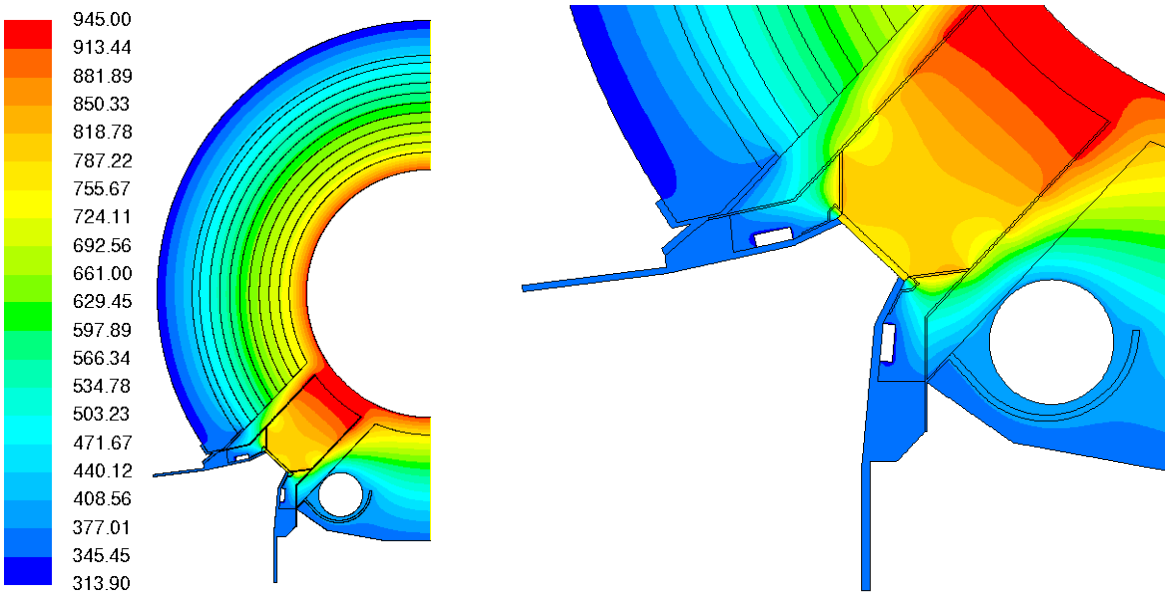

FIGURE 5: TEMPERATURE DISTRIBUTION OF THE RECEIVER CROSS SECTION. TEMPERATURE VALUES ARE IN K.

6.4. Receiver thermal insulation – Second version

Based upon the information derived by the first set of CFD simulations performed, a new version of the receiver thermal insulation was proposed. The main improvements were:

- increased number of radiation shields and reduced pitch in between;
- reduced number, as well as cross-section area, of the steel plates surrounding the cavities receivers;
- separation of the secondary optics from the external glass surface;
- increased cross-section area of the secondary optics cooling system;
- different arrangement of insulating materials;
- employment of a cheaper and stiffer aluminum-extruded framework for the secondary optics.

Figure 6 shows a schematic of the improved receiver thermal insulation.

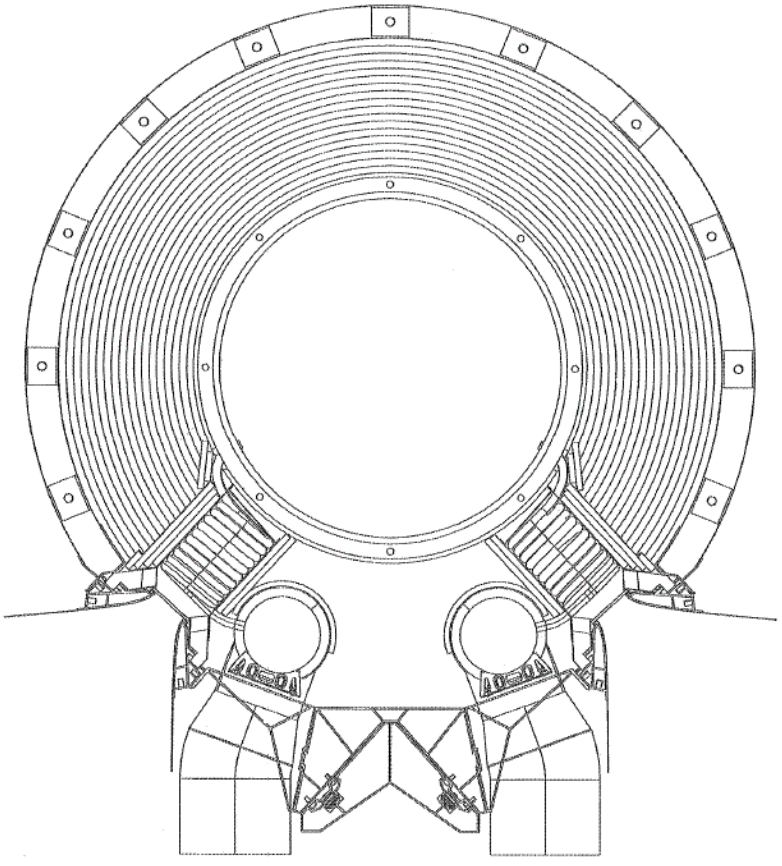

FIGURE 6: SCHEMATIC OF THE IMPROVED RECEIVER THERMAL INSULATION.

Most of the changes are focused in the cavities and secondary optics region. Figure 7 shows a magnification of the latter region wherein more details are visible. Some steel plates are still present because they are used either as support to keep in place the insulating materials and to enclose the cavities preventing the leakage of incoming radiation. In this improved design, due to constructive reasons, a new material was selected to build the insulating structure above the secondary optics. Microtherm® (“A” in Figure 7), withstanding higher temperatures, is still used to insulate the internal part of the cavity. It is enclosed by a different calcium silicate material, “B” in Figure 7, which can be easily cut in any desired shape.

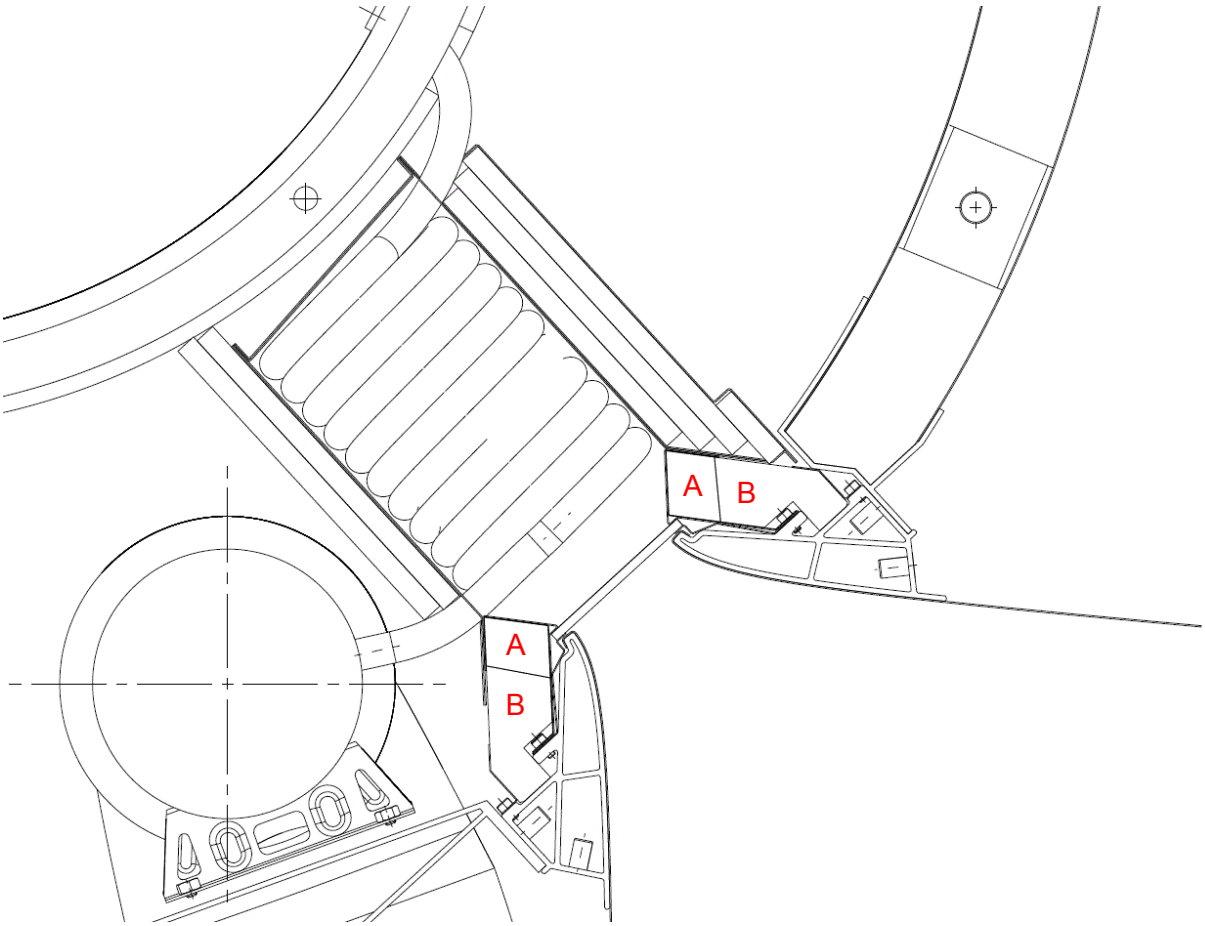

FIGURE 7: IMPROVED THERMAL INSULATION – DETAIL MAGNIFICATION.

6.5. CFD modelling and simulations

For this second geometry, as depicted in Figure 8, only a quarter of the whole receiver cross-section was considered as computational domain; the grid size was about 476’000 elements. Buoyancy-driven effects were not accounted for. The computational domain was therefore limited to the most critical region of the receiver cross section.

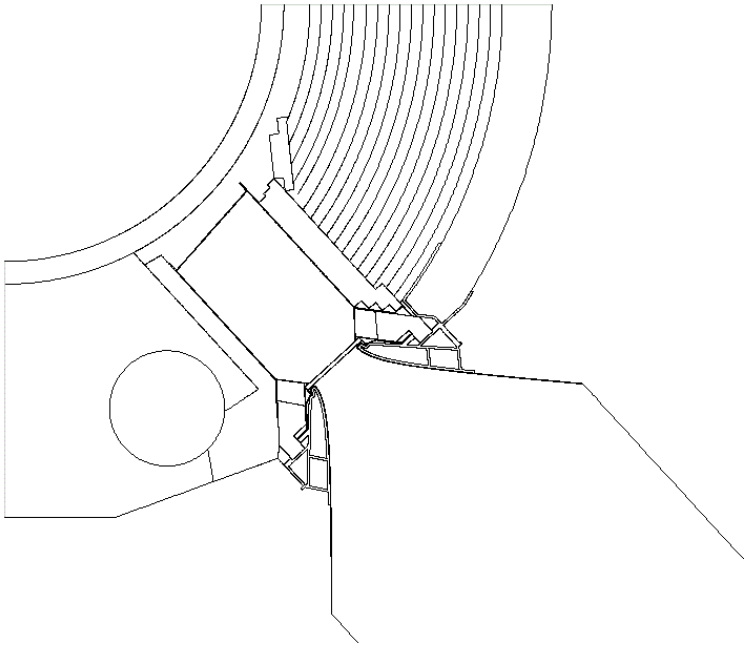

FIGURE 8: COMPUTATIONAL DOMAIN OF THE SECOND RECEIVER THERMAL INSULATION DESIGN.

A symmetry boundary condition was used either for the zone in between the two feeding pipes and for the thermal shields. For the latter, the strong assumption can be justified by the fact that, as observed from the previous simulations, far enough from the cavity the heat flux in the shields region is purely radial.

The computational domain was improved including the air region in front of the secondary optics allowing to consider the effect of the mutual interaction of the reflecting surfaces for radiative heat transfer.

Heat losses by means of convection and radiation were accounted for. The sky temperature was assumed equal to the temperature of the ambient into the balloon due to the optical behavior of the ETFE layer which is opaque in the IR spectrum region [4]. Considering the external surface as a blackbody at the given temperature, by means of Wien's displacement law [5], it was verified that the radiation peak occurs in the far IR region.

Figure 9 shows the result, in terms of temperature distribution, of the first CFD simulation performed. The computational domain enhancement allowed to observe the heat transfer between external surface of the glass and the secondary optics. In this case, the average temperature of the latter is about 350 K with a peak of 364 K in the region close to the external glass surface.

For this new design an average temperature of 900 K, well beyond the limit of the material, was observed for the most internal shields.

An optimization, that can be immediately proposed looking at these results, is the isolation of the fluid region above the cavity in order to avoid convective motions which would substantially increase the Microtherm® and shields temperature and therefore, the overall loss.

Another important information obtainable analyzing the temperature distribution is that, despite the reduction of the number and dimensions of structural steel plates, those remaining still offer an important favourable way for heat transfer. Therefore, it would be better to remove them completely or, at least, trying to limit their presence in the internal part avoiding them passing through the insulating materials.

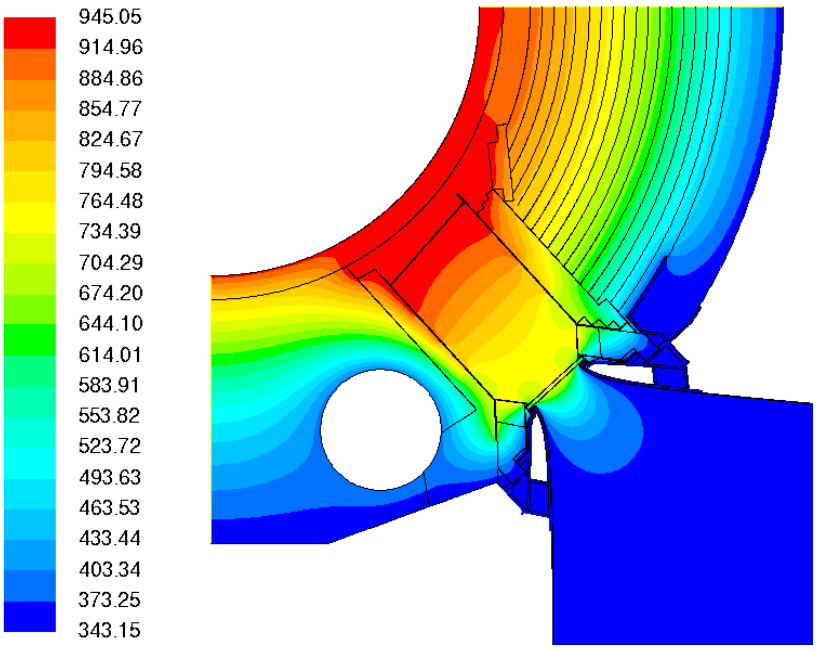

FIGURE 9: TEMPERATURE DISTRIBUTION OF THE RECEIVER CROSS SECTION. TEMPERATURE VALUES ARE IN K.

The power removed by the cooling circuit is comparable with that of the previous test case. This indicates that other improvements, such as wider separation between external glass surface and secondary optics and better insulation towards the internal components, are still required. A CFD test, in which the secondary optics surfaces were considered adiabatic in all the regions in contact with steel plates and internal structure, was performed to evaluate the possible reduction of power removed by the cooling circuit. An ideal 55% reduction was envisaged showing the relevance of the heat flux coming from the structure itself.

6.6. Receiver thermal insulation – Third version

A further improvement, in the design of the receiver thermal insulation, was proposed. The main variations with respect to the previous solutions are:

- complete removal of steel plates connected to the external part of the receiver;
- larger separation of the secondary optics from the external glass surface;
- reduced surface of the secondary optics face to face with the external glass surface;
- improved geometry of the secondary optics cooling circuit;
- different arrangement of insulating materials between cavity and secondary optics;
- isolation of the fluid region abode the cavity.

Figure 10 shows a schematic of the third version of the receiver thermal insulation. An important modification in this third version is related to the design of the region between cavity and secondary optics. The Microtherm® in zones “A” and “B” was substituted with an external ceramic material (zones “A” in Figure 10) and a calcium silicate material (zones “B” in Figure 10).

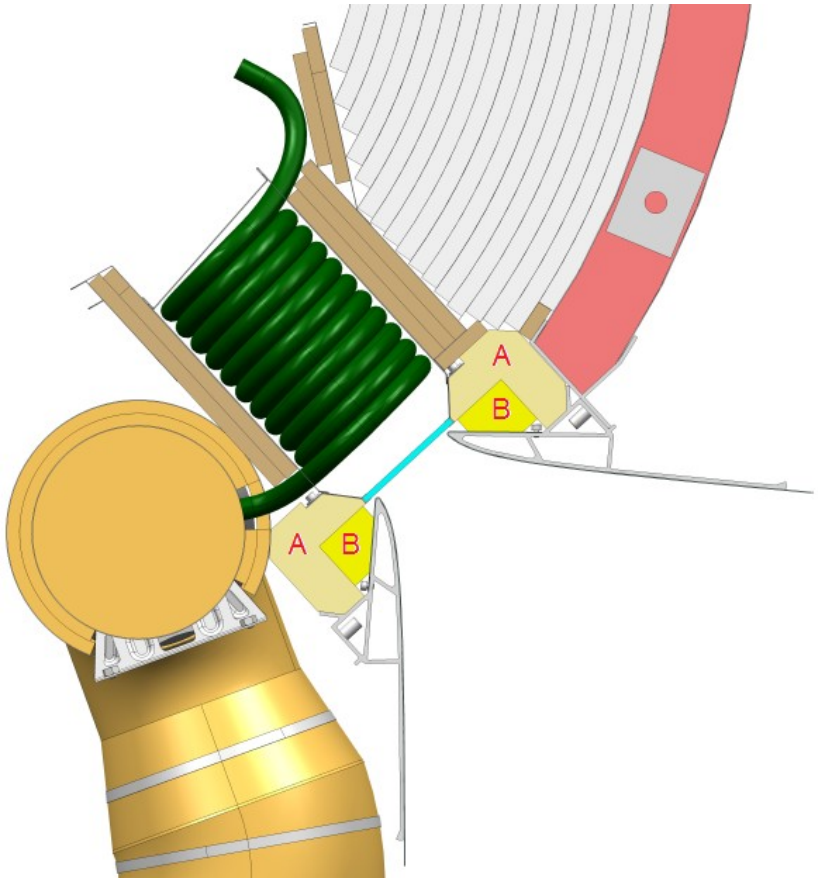

FIGURE 10: SCHEMATIC OF THE THIRD VERSION OF THERMAL INSULATION.

6.7. CFD modelling and simulations

The third geometry was analyzed exploiting the symmetry of the receiver cross section: as shown on the l.h.s. of Figure 11, only half of the cross section was considered as computational domain. The domain was discretized with a mapped grid of almost 490'000 quadrilateral cells.

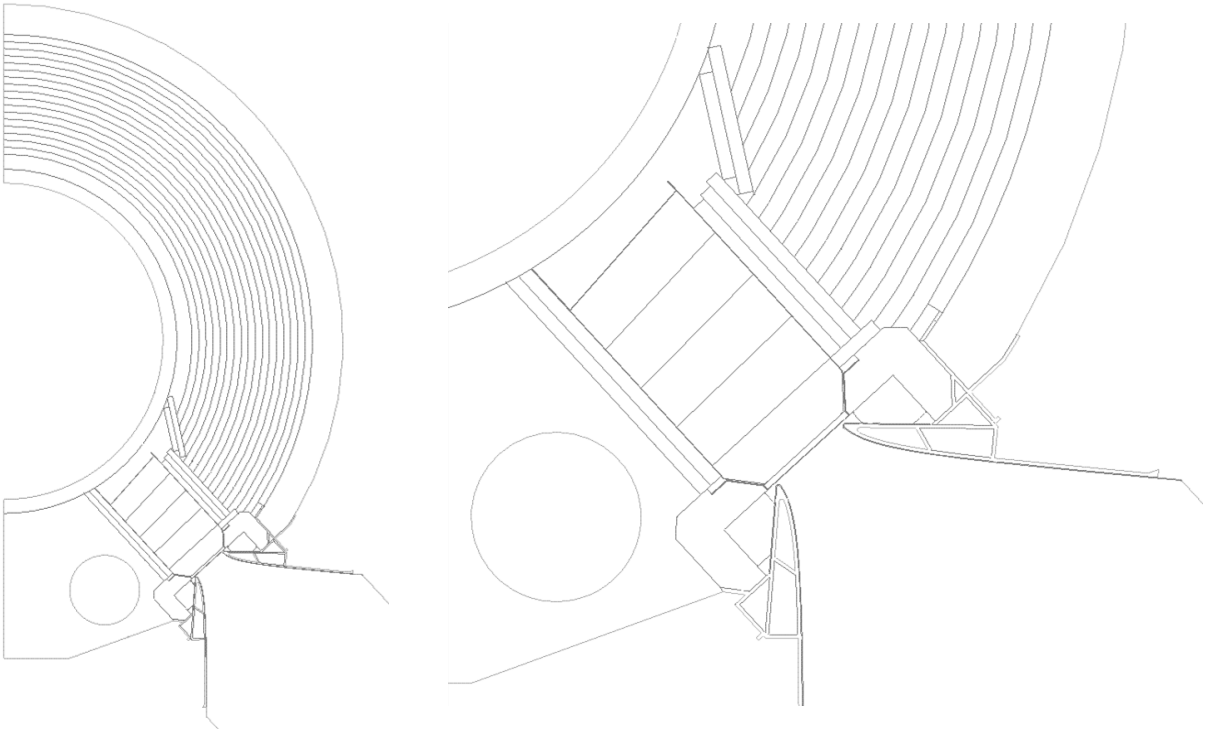

FIGURE 11: COMPUTATIONAL DOMAIN OF THE THIRD THERMAL INSULATION DESIGN; GLOBAL VIEW (L.H.S.) AND DETAIL MAGNIFICATION (R.H.S.).

The knowledge acquired from all the previous CFD simulations was used to set the parameters for all the computations performed with new geometry; therefore, all aforementioned modelling approximations and boundary conditions are still valid.

Figure 12 shows the temperature distribution of the thermal insulation for the half receiver cross-section with a magnification of the cavity-secondary optics region.

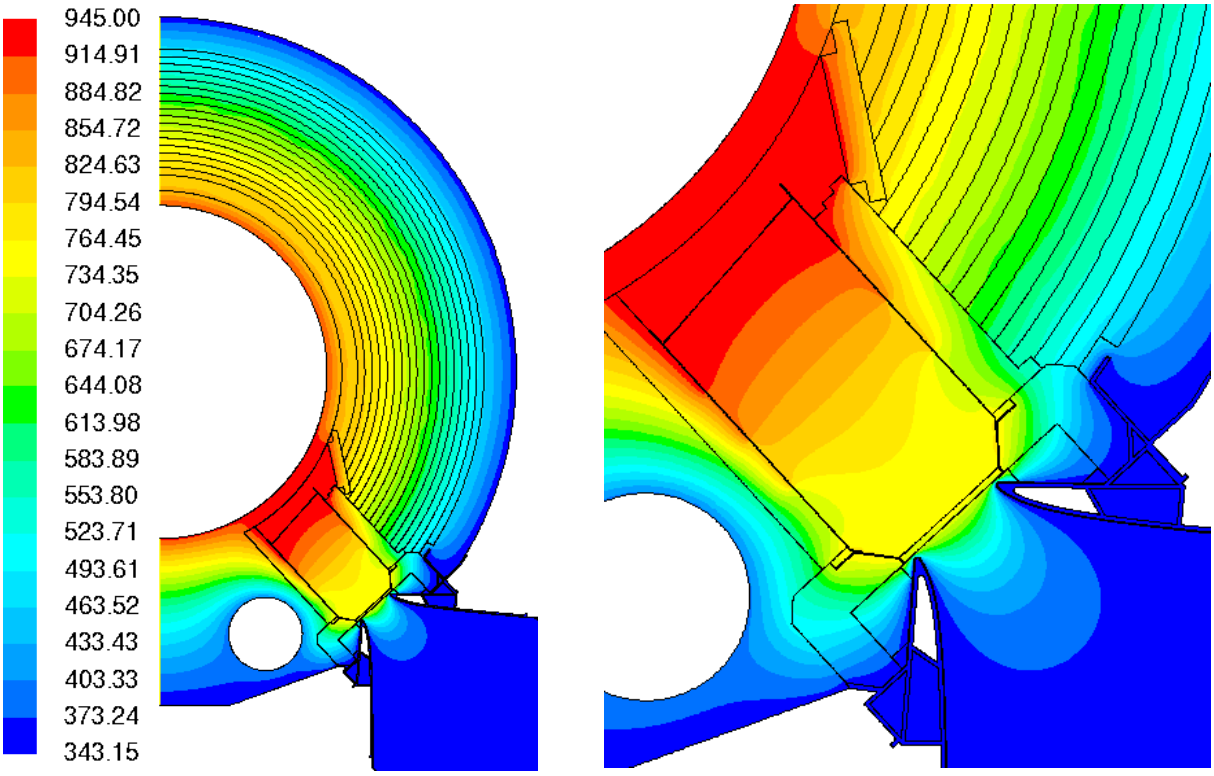

FIGURE 12: TEMPERATURE DISTRIBUTION OF THE THIRD THERMAL INSULATION DESIGN. TEMPERATURE VALUES ARE IN K.

It is worth to note that, the removal of the steel plates connected to both the internal and external regions avoided to prevent favourable ways for heat fluxes; moreover, the isolation of the fluid zones above the cavity led to a noticeable temperature reduction, to a maximum of 820 K, of the most internal shield. The improvements in the receiver thermal insulation design allowed to reduce, in this case, the overall heat losses of about 8.5% with respect to the original design.

A further simplification in the design of the region between cavity and secondary optics (“A” and “B” elements in Figure 10) was proposed. Instead of having the block made by the two different ceramic and calcium silicate materials, it was decided to use just one block of ceramic material. Despite its unfavourable thermal properties with respect to calcium silicate, the ceramic block can be easily machined. Hence, a new CFD simulation was performed to evaluate the effect of this modification on the receiver thermal insulation behaviour.

Simulations results showed that, as expected, substituting the calcium silicate with ceramic material led to an increment, of about 100 W/m, of the overall heat flux. The power removed by the cooling circuit showed the largest increment: the ceramic material has a higher thermal conductivity with respect to calcium silicate leading to a larger heat flux.

In order to reduce the undesirable effect abovementioned, it was proposed to decrease the contact area, between ceramic material and the secondary optics aluminium framework. The resulting empty space was filled with air; the small dimensions of the region allow to prevent the onset of convective motion. Figure 13 shows the reduced contact area between ceramic material and secondary optics.

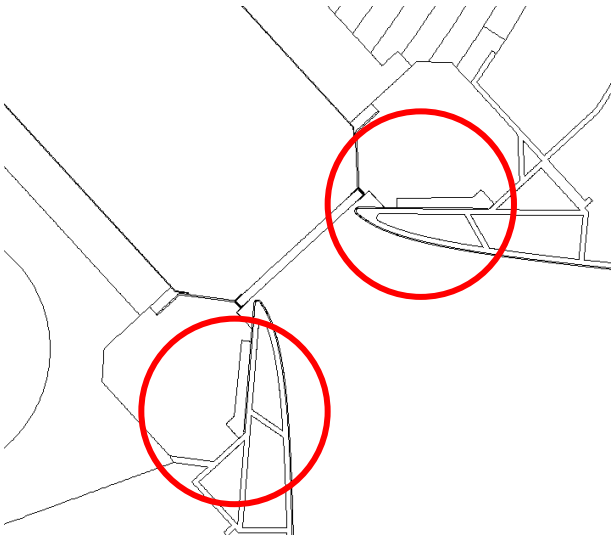

FIGURE 13: REDUCED CONTACT BETWEEN CERAMIC AND SECONDARY OPTICS FRAMEWORK.

Figure 14 shows the result of the CFD simulation, in terms of temperature distribution, of the new receiver thermal insulation.

Simulations results allowed to observe the beneficial effect of the modification proposed: the reduction of the contact area between ceramic and secondary optics leads to reduce the overall heat losses of almost 120 W/m.

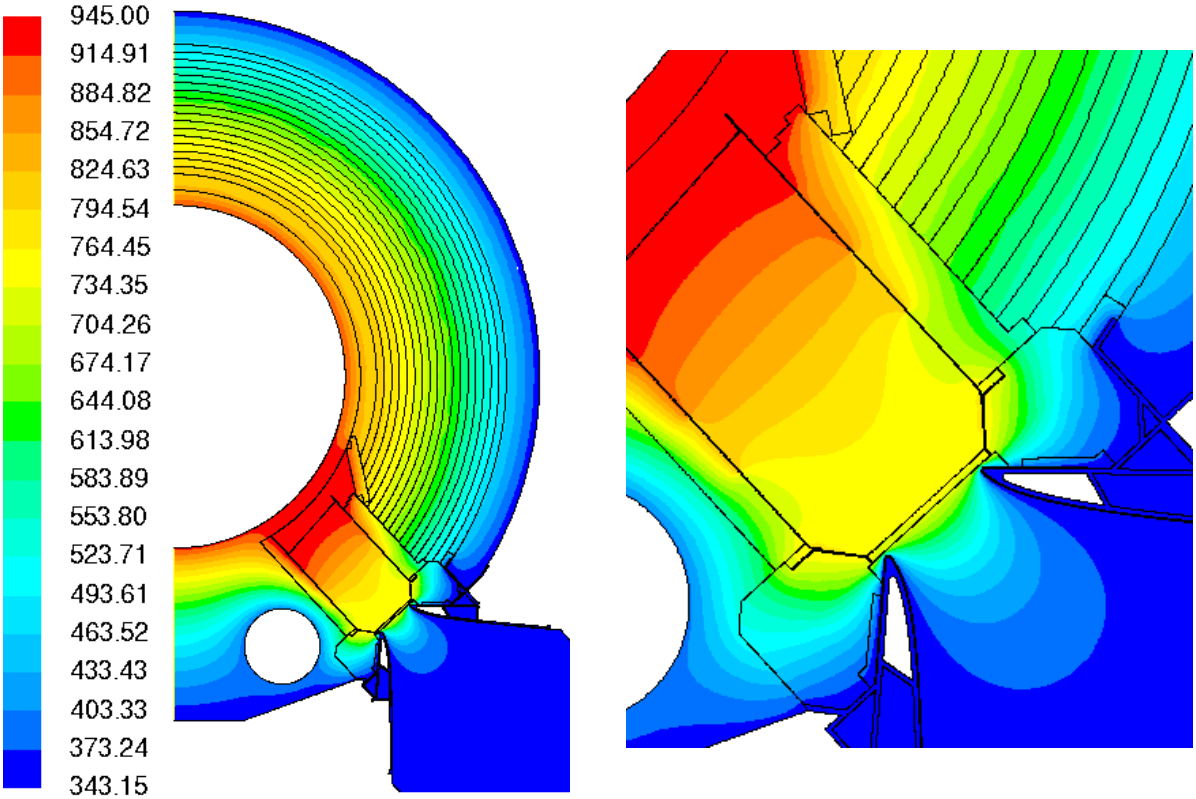

FIGURE 14: TEMPERATURE DISTRIBUTION OF THE THIRD THERMAL INSULATION DESIGN. TEMPERATURE VALUES ARE IN K.

6.8. Conclusions

The receiver thermal insulation behaviour has been analyzed by means of 2D steady-state CFD simulations. The analysis of the results obtained drove the various modifications in the thermal insulation design aimed at reducing as much as possible the receiver heat losses. A total of three different design versions have been studied achieving, at the end, a reduction of the overall heat losses of 9%, or about 233 W/m, with respect to the first thermal insulation design. The main modifications proposed, according to the CFD results obtained, are:

- the removal, or at least reduction, of the steel plates which provides a favorable way for heat flux from the internal to the external region of the receiver;

- the separation between secondary optics and external glass surface to reduce the amount of heat transfer, by means of conduction and radiation, between the two and, hence, the maximum secondary optics temperature;

- the isolation of the fluid region above the cavities from that between Microtherm® and internal shield to prevent the onset of convective motions.

6.9. References

[1] “www.microthermgroup.com,” [Online].

[2] “www.schott.com/borofloat/english/?highlighted_text=borofloat,” [Online].

[3] “SolAir 2 - Innovative solar collectors for efficient and cost-effective solar thermal power generation - 2,” BFE annual report, 2011.

[4] H. Poirazis, M. Kragh and C. Hogg, “Energy modelling of ETFE membranes in building applications,” Glasgow, Arup, 2009.

[5] J. Howell, R. Siegel and M. Menguc, “Thermal radiation heat transfer, 5th edition,” CRC Press, 2010.

THIS PAGE INTENTIONALLY LEFT BLANK

Chapter 7

Receiver performance analysis

Contents

List of Figures

7.1. Introduction: objectives and problem description

This section presents a mathematical model, based on the electrical analogy, developed to evaluate the performance of the new receiver design in terms of both available power and receiver efficiency.

The geometry has been optimized to guarantee a uniform distribution of the mass flow rate for each cavity.

Three different skew angles have been considered to assess the receiver performance at various reference working conditions.

7.2. Receiver structure

The receiver is composed by 36 modules (5.88 m long each) for a total length of 212 m. A schematic of the receiver is shown in Figure 1; whereas, its cross section can be seen on the l.h.s of Figure 2. Each module is composed by:

- 1 primary feed pipe;
- 2 secondary feed pipes;
- 128 cavities (64 for each of the two sides);
- 1 runback pipe;
- insulation, support, etc.

Air, flowing through the primary feed pipe, is distributed to each module through linking pipes. The feed pipes of each module provide the air flow to the cavities. In the cavities air heats up due to the concentrated solar radiation, and is then collected in the runback pipe.

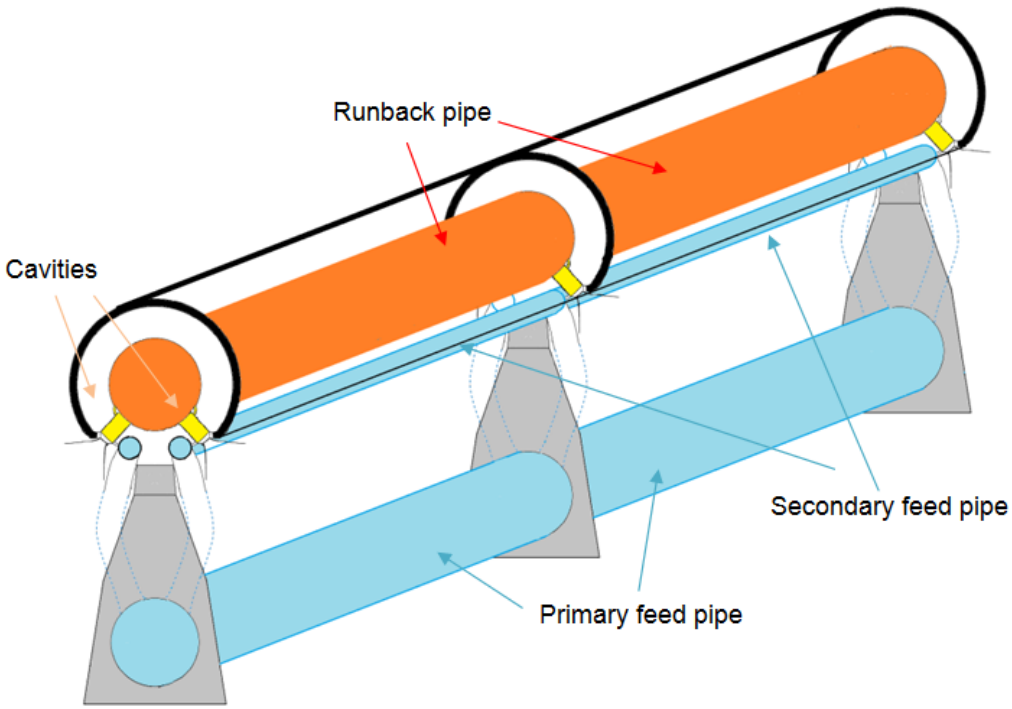

FIGURE 1: SCHEMATIC OF THE RECEIVER.

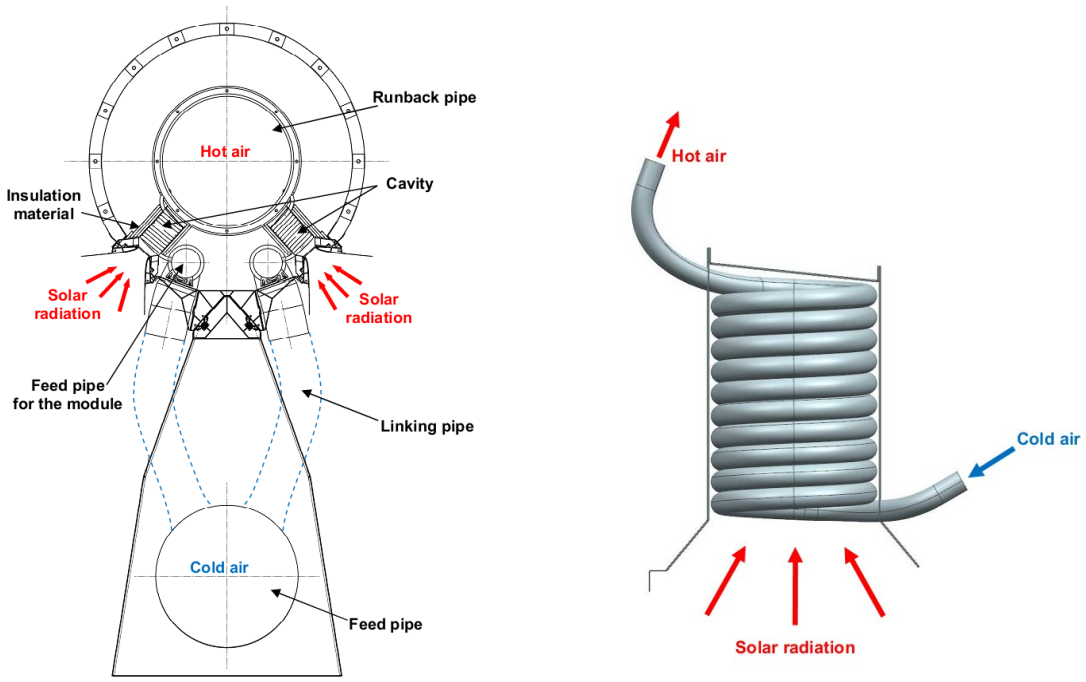

FIGURE 2: RECEIVER CROSS SECTION (L.H.S) – VIEW OF A SINGLE CAVITY (R.H.S).

Runback pipe

Runback pipe is thermally insulated by means of multiple concentric layers of:

- Microtherm®;
- radiation shields made of aluminium;
- support tube;
- polyurethane foam;
- external support tube.

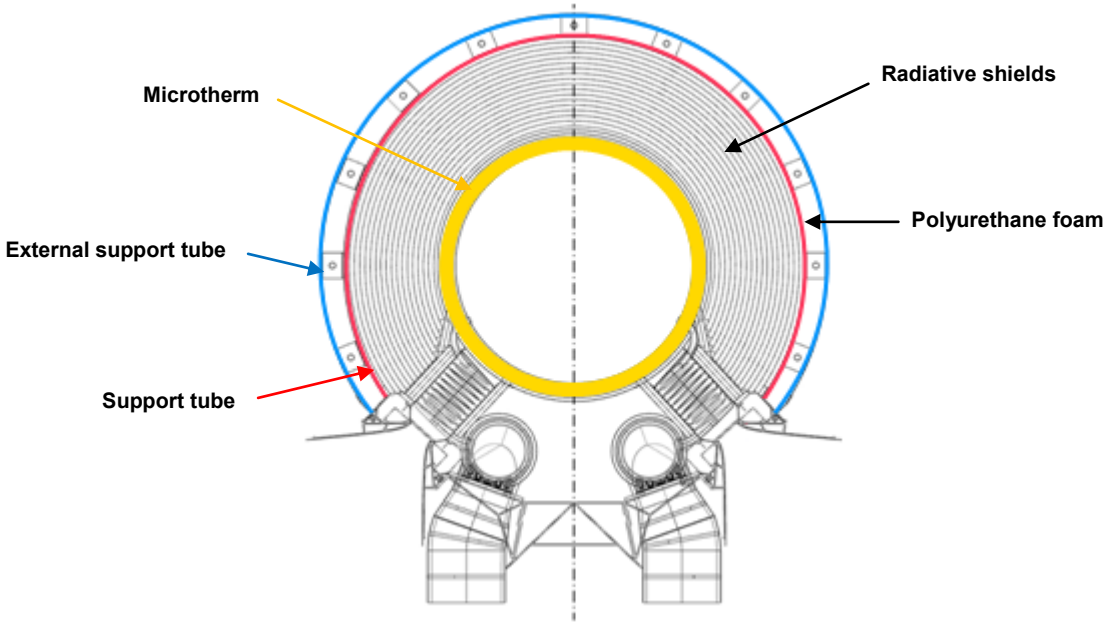

FIGURE 3: RUNBACK PIPE CROSS SECTION – DETAILS OF THE INSULATION.

7.3. Numerical modelling

7.3.1. Introduction

Evaluating the thermal losses of the entire receiver is a quite demanding task. The system is complex, composed by many parts and has very large physical dimensions. The fact that hot and cold air move counter-flow makes impossible to apply the “CFD-piecewise” modelling approach used for previous receivers [1]. Therefore an approach based on the electrical analogy was chosen.

7.3.2. Electrical analogy

The electrical analogy, already applied in Chapter 1 of this report, was used to model the whole receiver. The electrical circuit, representing the receiver, is shown in Figure 4. The model outputs are mass flow rate and air temperature for each cavity, pressure drop and air outlet temperature for the entire receiver.

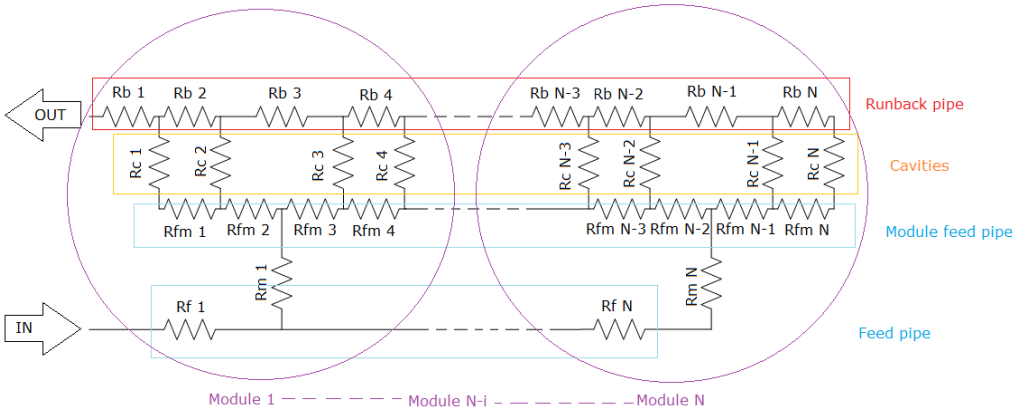

FIGURE 4: ELECTRICAL REPRESENTATION OF THE RECEIVER.

7.3.3. Cavity

The electrical analogy was also used to model the thermodynamic behaviour of the cavities. The model, already presented in this report, is schematically illustrated by Figure 5. The cavity model takes into account heat losses through the glass window and it is able to assess air outlet temperature and the pressure drop for a single cavity. The model results were validated comparing them with the CFD simulations, described in Chapter 2. A good agreement, in terms of air outlet temperature, was observed with a maximum difference of 5%. As far as concerning the heat losses, due to the modelling approximations assumed for the view-factors computation and for the internal cavity temperature, a lack of accuracy up to 30% was detected.

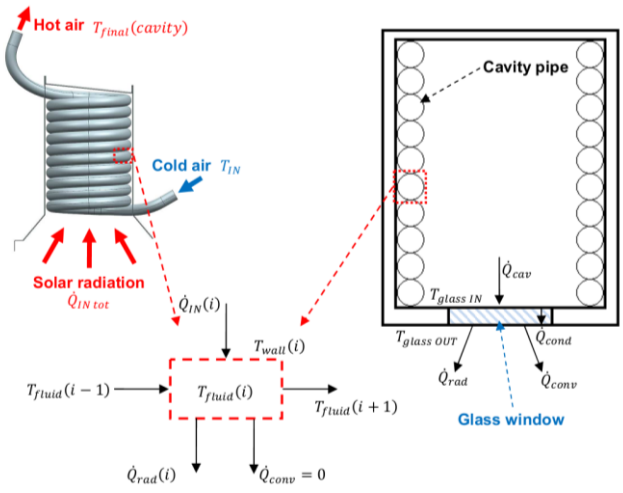

FIGURE 5: CAVITY NUMERICAL MODEL.

7.4. Results

Receiver simulations were carried out for three different skew angles of the concentrated incident radiation. The reference skew angles were 0°, 18° and 40° respectively.

7.4.1. Mass flow rate and flow baffles

A uniform distribution of the mass flow rate in the cavities has a twofold importance:

- a too low air mass flow rate in an irradiated cavity can bring the material temperature to overcome its upper limits;
- a too high mass flow rate can result in a too low air temperature at the cavity outlet.

Figure 6 shows that, for feed, linking, and runback pipes with constant diameters, and for cavities with equal dimensions, the air mass flow rate of the first and the last cavity of the receiver can be very different. For identical cavities, the higher is this difference, the higher will be the difference between cavities air outlet temperature.

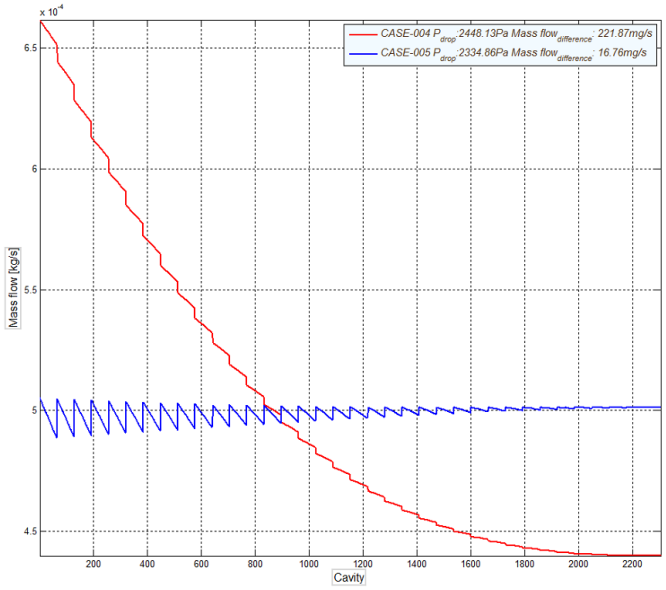

FIGURE 6: MASS FLOW RATE WITH DIAPHRAGM (BLUE LINE) / WITHOUT DIAPHRAGM (RED LINE).

To overcome this problem a proposed solution consists in adding a set of valves, one for each receiver module, to control the mass flow rate distribution. The idea is to install the valves on the pipes connecting the feed tube and the module (the so called “linking pipes”). For the purpose of this analysis valves where schematically represented as baffles to reduce the pipes cross section (see Figure 7). The dimension of the latter can be different for each module. The diameters of the reduced cross sections were designed targeting a given total mass flow rate for the receiver.

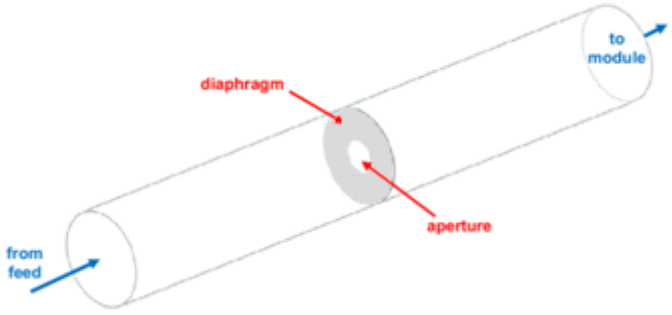

FIGURE 7: FLOW RESTRICTORS.

7.4.2. Performance at different skew angles

To evaluate the influence of the incoming solar radiation skew angle on the receiver performance, three different tests were performed at 0°, 18° and 40° skew angles. The receiver mass flow rate and inlet air temperature were kept constant. The total available power can be calculated from the DNI as:

$$P_{tot} = DNI \cdot L_{receiver} \cdot W_{mirror} \cdot cos(\theta_{skew})$$

The power entering each cavity is calculated as the total collected power multiplied by the optical efficiency (which takes into account the mirror and the secondary concentrator efficiencies as well as the incoming beam reflections onto the glass surface) and divided by the total number of cavities.

$$P_{cavity} = \frac{P_{tot} \cdot \eta_{optics}}{N_{cavities}}$$

The power gathered by the fluid is given by:

$$P_{fluid} = m_{flow-tot} \cdot C_P\,(T_{ave}) \cdot (T_{out} - T_{in})$$

The ratio between the power harvested by the HTF and the total radiation energy entering the cavities represents the solar-to-thermal receiver efficiency:

$$\eta_{receiver} = \frac{P_{fluid}}{P_{cavity} \cdot N_{cavities}}$$

Multiplying the amount of power, gathered by the HTF, by the power-block efficiency (assumed equal to 0.3) the electrical power available can be computed as:

$$P_{electrical-available} = P_{fluid} \cdot \eta_{power\ block}$$

Since the HTF must be pumped in the circuit to keep the system running, the pumping power can be evaluated using the pressure losses computed with the electrical analogy.

$$P_{pumping} = \frac{m_{flow\ tot} \cdot \Delta p}{\rho(T_{in})}$$

Pumping power must be subtracted from electrical power available to obtain the useful power:

$$P_{useful} = P_{electrical-available} - P_{pumping}$$

It is now possible to calculate the solar-to-electric system efficiency:

$$\eta_{system} = \frac{P_{useful}}{P_{tot}}$$

The results obtained show that a system efficiency up to 20% seems to be achievable for skew 0° and skew 18° working conditions. For wider skew angles, the system efficiency slightly decreases. The receiver efficiency, instead, seems to be insensitive to the skew angle variation. This is due to the aforementioned modelling approximations (paragraph 7.3.3) for the heat losses computation wherein an average internal cavity temperature, and a simplified view-factor correlation, were used to calculate the radiative heat transfer. These assumptions lead to reduce the heat losses, in the case of large skew angles working conditions, mitigating the effect of the presence of a hot region close to the glass surface.

7.5. Conclusions

A zero-dimensional mathematical model developed, based upon the electrical analogy, has been used to analyze the behavior of the entire receiver, i.e. the whole system including all cavities, the feeding and runback pipes. With this model, the receiver performance was evaluated for three working conditions corresponding to three different skew angles. Receiver data examined were:

- power harvested by the HTF flowing through the cavities;
- temperature of the HTF at the outlet sections of both the cavities and the run-back pipe;
- pressure drop through the receiver;
- mass flow rate distribution within the cavities.

The predicted receiver performance shows that, depending upon the skew angle working conditions, a system efficiency (solar-to-electric) up to 20% seems to be achievable. The temperature of the HTF at the outlet section of the run-back pipe was found to be equal to 655.5°C, 626.4°C and 502.5°C for the skew 0°, 18° and 40° working conditions respectively.

The simulations performed showed that, to achieve a proper and uniform working condition of all cavities along the receiver, a set of valves, or diaphragms, has to be implemented onto the linking pipes, i.e. the ducts connecting the feeding pipe with the cavities. In fact, these devices are necessary to balance the distribution of the air mass flow rate into the cavities and make them perform uniformly in terms of outlet air temperature.

7.6. References

[1] “SolAir 2 – Innovative solar collectors for efficient and cost-effective solar thermal power generation-2”, BFE annual report, 2010.

Chapter 8

Thermal energy storage system prototype

Contents

List of Figures

8.1. Experimental void fraction measurement under cyclic load condition

In order to assess the effect of cyclic load conditions on the porosity distribution of the packed bed, a new experimental test has been performed. The cylindrical iron tank, already employed in [1], with 2 m inner diameter and 1.5 m height was used for the test. In this case also, the void fraction was measured by filling the packed bed with a known volume of water and measuring the water level in the packed bed. For this purpose, a steel tube with 40 mm outer diameter and 1.5 m height was welded coaxially to the bottom of the tank. The steel tube was drilled at the bottom in order to ensure equal water level as in the packed bed. As depicted in Figure1, six external vibrators with a working moment of 7.96 kgcm each and 3'000 rpm were assembled on the outside of the tank with 60° angular intervals.

FIGURE1: PHOTOGRAPH OF THE TEST TANK USED FOR THE MEASUREMENTS.

The tank was then filled with non-homogeneous river pebbles with equivalent diameters of about 30 mm. The pebbles were used in a previous experimental campaign in a packed bed thermal energy storage prototype. The filling was carried out by a hydraulic shovel in order to reproduce the same random packing conditions as in the storage prototype.

The vibrators were used to shake the packing for approximately 20 minutes simulating the upwards/downwards movement of the packed bed subjected to several charging/discharging cycles.

After the aging process, the packed bed settled for an average of a couple of centimetres to more than 5 cm in the vibrators region (Figure 2). At that time, the void fraction of the packed bed was measured filling it with water in seven steps, of 200 litters each, and measuring the water level in the tube at the end of every step with a Bosch DLR130K Digital distance measurer (accuracy of 1.5 mm). This led to observe that the average bulk void fraction decreased from 0.342, of the randomly packed bed condition, to 0.332 of the vibrated bed.

FIGURE 2: TOP SURFACE OF THE PACKED BED AFTER THE VIBRATION PROCESS.

The final comparison between the experimental results of the two tests performed shows that the monotonic decrease, obtained during the first experimental test under randomly packed condition (Figure 3), was replaced by an oscillatory behaviour of the void fraction (Figure 4).

The vibration eliminates the effect of the gravitational force and allows the pebbles to re-arrange in the tank. However, the void fraction distribution is also strongly dependent on vibration dimension, amplitude and frequency as well as the duration of the vibration.

The results from the axial void fraction variation are important for increasing the understanding of the phenomenon and are useful for designing storage systems, since the storage capacity of the packed bed is directly related to its packing density and the pressure drop, experienced by the air passing through the rocks, is inversely proportional to their void fraction [2].

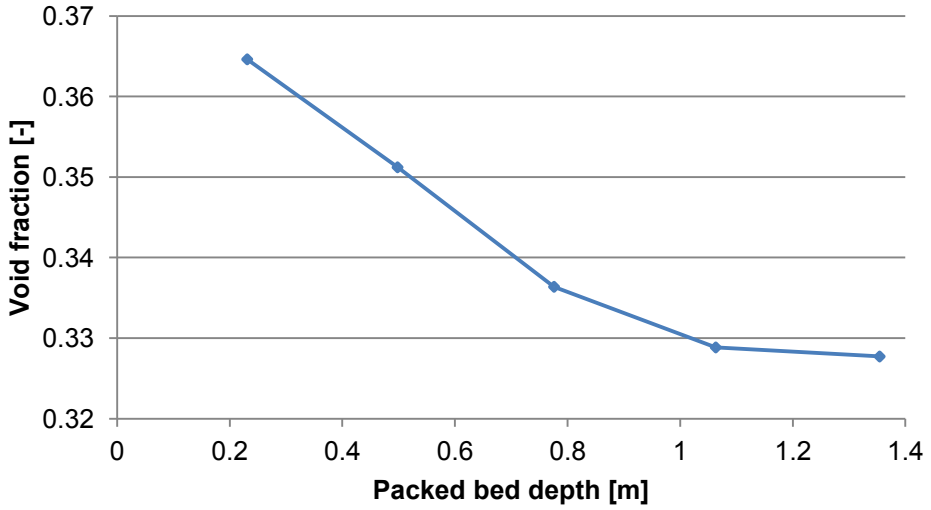

FIGURE 3: AXIAL VOID FRACTION DISTRIBUTION IN THE PACKED BED BEFORE VIBRATION.

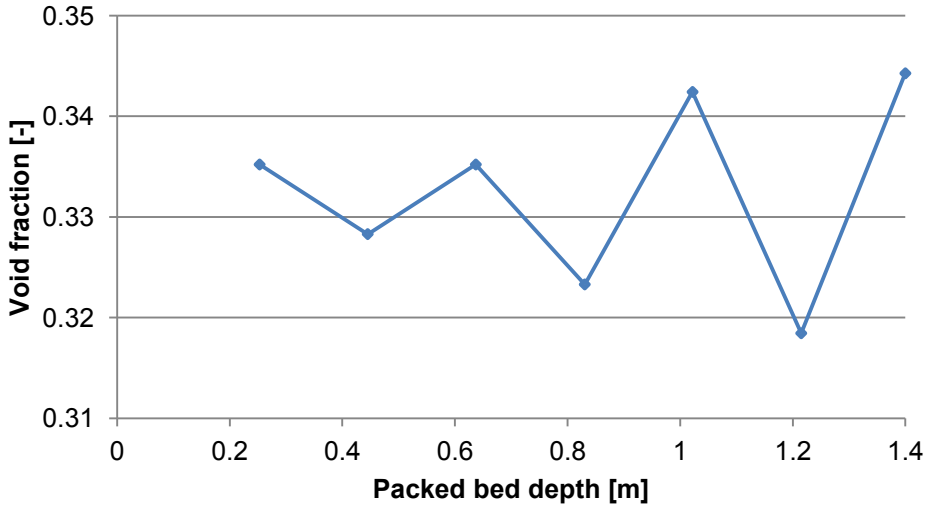

FIGURE 4: AXIAL VOID FRACTION DISTRIBUTION IN THE PACKED BED AFTER VIBRATION.

8.2. New storage prototype: tests campaign proposal

In order to assess the performance of the new storage prototype, the previous test procedure, already mentioned in [1], has been enriched with other tests. The final test campaign was divided into two different groups containing basically the same tests with the difference that they are expected to be performed under different operating pressures.

After a first preliminary phase of fibers evaporation, which will lead to the complete evaporation of the fibers contained within the concrete walls resulting in a stable thermal behaviour and a lower thermal conductivity of the concrete vessel, all the other tests may be summarized as follows:

- **Cyclic load**: the aim of this test is to study the behaviour of the storage subjected to a continuative cyclic load composed by 5 complete cycles. The inlet temperature and the mass flow rate should be kept constant for the whole test. Each cycle consists of a charging and a discharging phase as described below:
    - **Charging phase**: During the charging phase air with constant mass flow rate and high temperature is fed to the storage from top for a specific amount of time. At the beginning of the first charging phase the storage should be at its dead state (thermally depleted). The charging time will be defined once both the available mass flow rate and the inlet temperature are known. The temperature evolution will be monitored and recorded.
    - **Discharging phase**: During the discharging phase, air with the same mass flow rate as in the charging phase and ambient temperature is pumped into the storage from bottom for the same amount of time as the charging phase. In this case also, the temperature evolution will be monitored along the whole test.

- **Idle time**: this test is aimed to analyze the behaviour of the full-charged storage during an arbitrary idle time. It allows to assess the degradation of the thermo-cline zone and the thermal losses towards the environment.

- **Fast discharging phase**: this test is aimed to evaluate the performance of the storage in the case of fast discharging phase, performed with a high mass flow rate. The information obtained can be useful to assess the capability of the storage to deliver the most of the stored power, as quickly as possible, simulating its sudden use (for instance during a peak energy demand).

- **Fast discharging phase with different mass flow rates**: conceptually this test is the same as the previous; the difference here is that the storage will be suddenly discharged with different mass flow rates to investigate the limits of good heat transfer between solid and fluid.

During the tests execution, information about temperature distribution, pressure drop and mass flow rates, will be monitored and recorded by means of measuring instruments such as: thermocouples, flow meters and pressure gauges.

8.3. Construction progress of the new storage prototype in Biasca

Due to some unforeseen events, the construction of the new TES system prototype in Biasca has been delayed. At the moment, the works proceed regularly and the construction progress is represented in the following pictures.

FIGURE 5: EXTERNAL VIEW OF THE NEW STORAGE PROTOTYPE.

Figure 6 depicts the internal part of the storage system equipped with the insulating materials:

– Dark grey bricks: FoamGlas®;

– Light grey bricks at the bottom: Microtherm®.

Other low density concrete blocks will be positioned afterwards to protect the insulating materials from direct contact with pebbles.

FIGURE 6: INTERNAL PART OF THE NEW STORAGE PROTOTYPE.

8.4. Storage Design for Plant in Morocco

A purpose-built quasi-one-dimensional model [3], experimentally validated, was used to design and predict the performance of the storage unit of the plant in Morocco. The solar plant is connected to an organic Rankine cycle and has the goal of upgrading the process heat of a cement factory, entering the plant at 280°C. Therefore, the inlet temperature of the solar plant is 280°C. The cyclic parameters, obtained by doing 30 consecutive cycles are presented in Figure 5. The total losses per cycle are below 4% of the incoming energy and the overall efficiency increases to 91% as the storage approaches its steady behaviour. The final outflow temperature represents the temperature of the air leaving the storage at the end of the discharging phase, hence the lowest outlet temperature of each cycle. The internal temperature profile in the packed bed at the end of the charging and end of the discharging phase for the cycles #1, #10, #20 and #30 are shown in Figure 6. Figure 7 depicts two technical drawings of the final storage design.

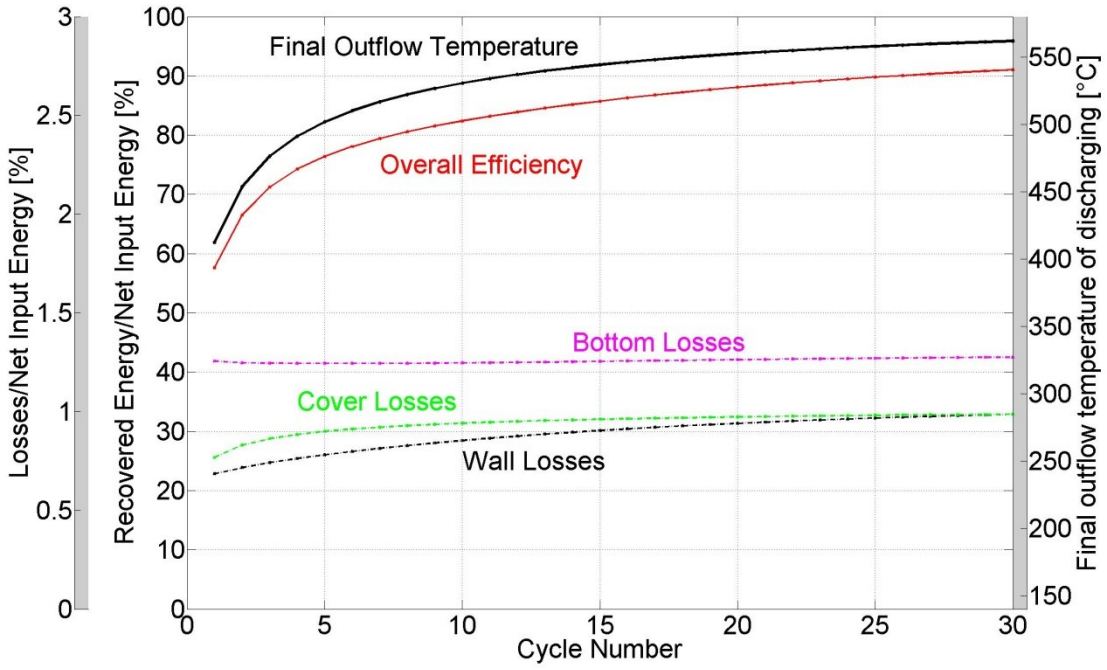

FIGURE 7: CYCLIC PARAMETERS OF THE STORAGE UNIT IN MOROCCO.

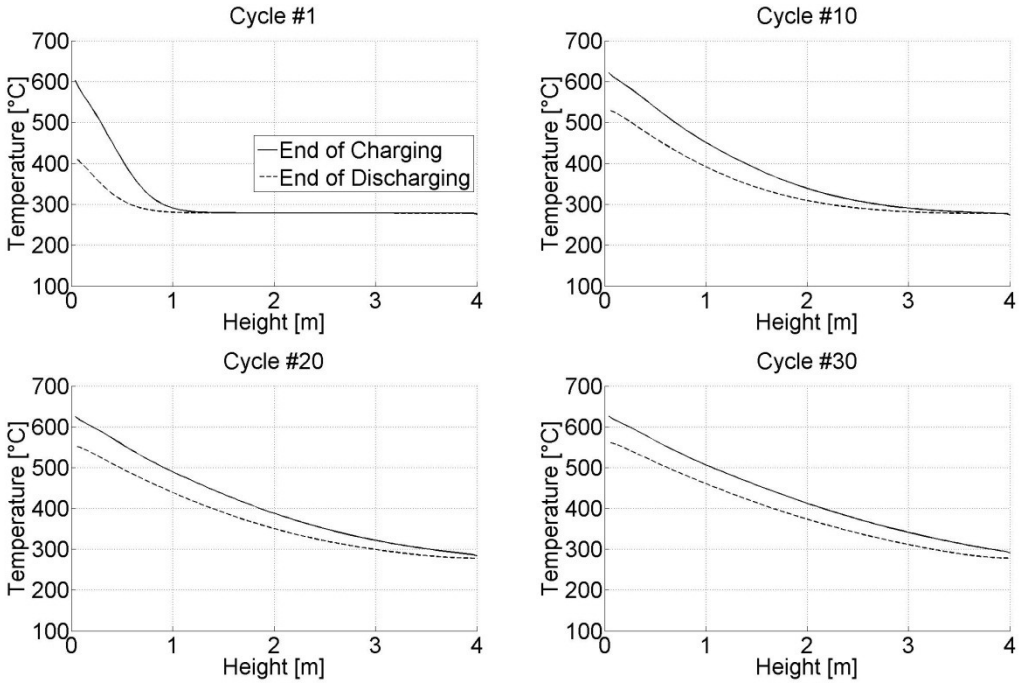

FIGURE 8: INTERNAL TEMPERATURE PROFILE IN THE PACKED BED AT THE END OF THE CHARGING AND END OF THE DISCHARGING.

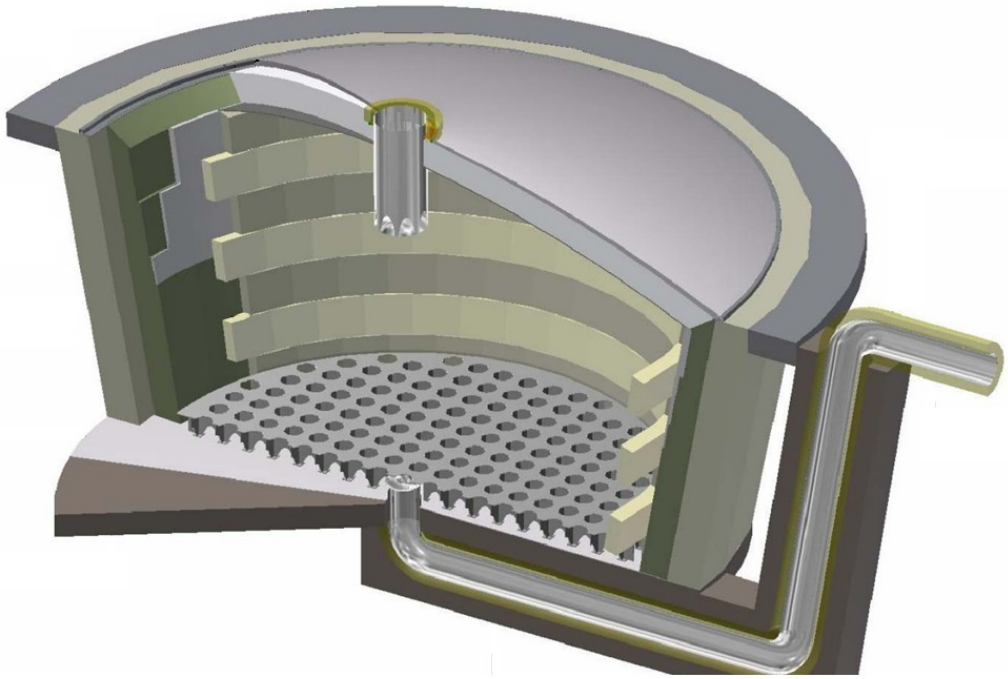

FIGURE 9: SCHEMATIC OF THE STORAGE UNIT IN MOROCCO.

8.5. Publications

The detailed study of the behaviour of the real packed bed prototype, in terms of void fraction distribution [4] and effective thermal conductivity [5], allowed to achieve a high accuracy level in its CFD modelling.

Since the integration of a TES system into a CSP plant is a key factor to compete with PV to produce electric energy at low price, it is very important to have the right tools to model its performance in the most precise and affordable way. For this reason, a paper, containing all the main results related to the thermal behaviour of the real prototype, was presented to the SolarPACES 2012 conference, in Marrakech, Morocco and to the International CAE conference 2012, in Verona, Italy.

The details of the papers presented are:

Simone A. Zavattoni, Maurizio C. Barbato, Andrea Pedretti, Giw Zanganeh. Aldo Steinfeld, "Effective thermal conductivity and axial porosity distribution of a rock-bed TES system: CFD modeling and experimental validation". SolarPACES 2012 Conference, Marrakech, Morocco. Paper ID: 23336

Simone A. Zavattoni, Davide Montorfano, Antonio Gaetano, Gian Maria Di Stefano, Maurizio C. Barbato, "CFD Modeling Suitable for Concentrated Solar Power Applications: Thermal Insulation Based on Radiation Shields and Thermal Energy Storage Systems.". International CAE conference, Verona, Italy.

Besides the detailed 3D flow and temperature distribution in the packed bed, a dynamic model has been developed to be used for scale-up design, optimization, and system integration. The details of the modelling, validation and scale up are found at [3]:

*Zanganeh G., Pedretti A., Zavattoni S., Barbato M., Steinfeld A., "*Packed-bed thermal storage for concentrated solar power – pilot-scale demonstration and industrial-scale design*", Solar Energy, Vol. 86, pp. 3084-3098, 2012.*

The model described in the paper is a quasi-one-dimensional heat transfer model with separate solid and fluid phases and considers thermal losses from the lateral walls, the lid and the bottom and axial dispersion in the packed bed. The fluid and solid thermo-physical properties (which have been experimentally measured) are implemented temperature-dependent in the model and the axial void fraction distribution is set according to the experimental results previously presented.

8.6. References

[1] “SolAir 2 - Innovative solar collectors for efficient and cost-effective solar thermal power generation - 2,” BFE annual report, 2011.

[2] S. Ergun, “Fluid flow through packed columns,” in *Chemical Engineering Progress 48*, 1952, pp. 89-94.

[3] Zanganeh G., Pedretti A., Zavattoni S., Barbato M., Steinfeld A., “Packed-bed thermal storage for concentrated solar power – pilot-scale demonstration and industrial-scale design”, Solar Energy, Vol. 86, pp. 3084-3098, 2012.

[4] Simone A. Zavattoni, Maurizio C. Barbato, Andrea Pedretti, Giw Zanganeh. “CFD simulations of a pebble bed thermal energy storage system accounting for porosity variations effects”. SolarPACES 2011 Conference, Granada, Spain. Paper: 24636.

[5] S. Zavattoni and M. Barbato, “Effective thermal conductivity in packed beds of natural rocks,” SUPSI Internal report, 2011.

THIS PAGE INTENTIONALLY LEFT BLANK